

SANDIA REPORT

SAND2016-12167

Unlimited Release

Printed November 2016

NSRD-11: Computational Capability to Substantiate DOE-HDBK-3010 Data

David L.Y. Louie, Alexander L. Brown, Fred Gelbard, John Bignell, Flint Pierce, Tyler Voskuilen, Salvador B. Rodriguez, Remi Dingreville, Ethan T. Zepper, Pierre-Alexandre Juan, San Le, and Lindsay N. Gilkey

Prepared by
Sandia National Laboratories
Albuquerque, New Mexico 87185 and Livermore, California 94550

Sandia National Laboratories is a multi-mission laboratory managed and operated by Sandia Corporation, a wholly owned subsidiary of Lockheed Martin Corporation, for the U.S. Department of Energy's National Nuclear Security Administration under contract DE-AC04-94AL85000.

Approved for public release; further dissemination unlimited.



Sandia National Laboratories

Issued by Sandia National Laboratories, operated for the United States Department of Energy by Sandia Corporation.

NOTICE: This report was prepared as an account of work sponsored by an agency of the United States Government. Neither the United States Government, nor any agency thereof, nor any of their employees, nor any of their contractors, subcontractors, or their employees, make any warranty, express or implied, or assume any legal liability or responsibility for the accuracy, completeness, or usefulness of any information, apparatus, product, or process disclosed, or represent that its use would not infringe privately owned rights. Reference herein to any specific commercial product, process, or service by trade name, trademark, manufacturer, or otherwise, does not necessarily constitute or imply its endorsement, recommendation, or favoring by the United States Government, any agency thereof, or any of their contractors or subcontractors. The views and opinions expressed herein do not necessarily state or reflect those of the United States Government, any agency thereof, or any of their contractors.

Printed in the United States of America. This report has been reproduced directly from the best available copy.

Available to DOE and DOE contractors from

U.S. Department of Energy
Office of Scientific and Technical Information
P.O. Box 62
Oak Ridge, TN 37831

Telephone: (865) 576-8401
Facsimile: (865) 576-5728
E-Mail: reports@osti.gov
Online ordering: <http://www.osti.gov/scitech>

Available to the public from

U.S. Department of Commerce
National Technical Information Service
5301 Shawnee Rd
Alexandria, VA 22312

Telephone: (800) 553-6847
Facsimile: (703) 605-6900
E-Mail: orders@ntis.gov
Online order: <http://www.ntis.gov/search>



SAND2016-12167
Unlimited Release
Printed November 2016

NSRD-11: Computational Capability to Substantiate DOE-HDBK-3010 Data

David L. Y. Louie
Severe Accident Analysis

Alexander L. Brown and Ethan T. Zepper
Fire Science and Technology

Fred Gelbard
Advanced Nuclear Fuel Cycle Technology

John Bignell, Remi Dingreville, Lindsay N. Gilkey, Pierre-Alexandre Juan, and San Le
Structural and Thermal Analysis

Flint Pierce and Tyler Voskuilen
Computational Thermal and Fluid Mechanics

Salvador B. Rodriguez
Advanced Nuclear Concepts

Sandia National Laboratories
P.O. Box 5800
Albuquerque, New Mexico 87185-0748

Abstract

Safety basis analysts throughout the U.S. Department of Energy (DOE) complex rely heavily on the information provided in the DOE Handbook, DOE-HDBK-3010, Airborne Release Fractions/Rates and Respirable Fractions for Nonreactor Nuclear Facilities, to determine radionuclide source terms. In calculating source terms, analysts tend to use the DOE Handbook's bounding values on airborne release fractions (ARFs) and respirable fractions (RFs) for various categories of insults (representing potential accident release categories). This is typically due to both time constraints and the avoidance of regulatory critique. Unfortunately, these bounding ARFs/RFs represent extremely conservative values. Moreover, they were derived from very limited small-scale bench/laboratory experiments and/or from engineered judgment. Thus, the basis for the data may not be representative of the actual unique accident conditions and configurations being evaluated.

The goal of this research is to develop a more accurate and defensible method to determine bounding values for the DOE Handbook using state-of-art multi-physics-based computer codes. This enables us to better understand the fundamental physics and phenomena associated with the types of accidents in the handbook. In this year,

this research included improvements of the high fidelity codes to model particle resuspension and multi-component evaporation for fire scenarios. We also began to model ceramic fragmentation experiments, and to reanalyze the liquid fire and powder release experiments that were done last year. The results show that the added physics better describe the fragmentation phenomena. Thus this work provides a low-cost method to establish physics-justified safety bounds by taking into account specific geometries and conditions that may not have been previously measured and/or are too costly to perform.

ACKNOWLEDGMENTS

Dr. Louis F. Restrepo of Atkins NS has provided guidance and review for this project. He is one of the original contributors and reviewers to DOE-HDBK-3010, and both his expertise with DOE-HDBK-3010 and his extensive experience in the U.S. Department of Energy (DOE) facility nuclear safety have helped this project significantly. We also thank the summer interns, Cole C. Mueller and Bobbi Merryman for providing support in the Fuego simulations of the 50 psig powder release experiment and the Fish experiment, Michael Wagner for developing the mesh model for the powder release simulations, Victor Figueroa for performing the difficult STORM SR-11 simulations early in the project and many of the SIERRA's solid mechanics team for their support, especially Dr. Nathan K. Crane, Dr. Mark T. Merewether, and Dr. Michael R. Tupek. Finally, the authors would like to express their appreciation to Dr. Alan Levin and Patrick Frias of DOE-HSS (AU-30) for overseeing this research. This work is supported by the DOE Health, Safety and Security Nuclear Safety Research and Development Program under WAS Project No. 2015-AU30-SNL-DOE H 3010.

This Page Intentionally Left Blank

CONTENTS

Acknowledgments.....	5
Contents	7
Figures.....	8
Tables	11
Nomenclature	12
1 Introduction.....	17
1.1 Accomplishment in FY2015 (Year 1).....	19
1.1.1 Liquid Fire experiments	19
1.1.2 Exploratory Simulations	20
1.2 Tasks in FY2016 (Year 2).....	23
2 Fuego Model Development.....	25
2.1 Resuspension Model Development.....	25
2.1.1 Model Overview	25
2.1.2 Model Testing	30
2.2 Multi-Component Evaporation Model Development	36
2.2.1 Model Overview	36
2.2.2 Model Testing	42
2.3 Summary and Conclusion	48
3 Resuspension Model testing and application.....	49
3.1 Fish Experiment Description	50
3.1.1 Fuego Aerosol Model	51
3.1.2 Fuego Results and Discussions.....	52
3.2 Summary and Conclusion	54
4 Reanalyzing Fire Experiments.....	55
4.1 Beaker Fire Simulations.....	55
4.1.1 Introduction.....	55
4.1.2 Methods and Simulation Details.....	56
4.1.3 Results and Discussions	58
4.1.4 General Discussions.....	66
4.2 Gasoline Fire Simulation	66
4.2.1 Introduction.....	66
4.2.2 Theory	67
4.2.3 Methods.....	69
4.2.3.3.1 Computational mesh	70
4.2.4 RESULTS AND DISCUSSION.....	74
4.2.4.2 Resuspension Entrainment.....	78
4.2.5. GENERAL DISCUSSION	78
4.3 Summary and Conclusion	79
5 ReAnalyzing Powder Release Experiments.....	81
5.1 Gravitational (Free Fall) Spill Experiments.....	81

5.1.1	Experimental Data	82
5.1.2	Fuego Simulation	83
5.1.3	Summary and Conclusion	89
5.2	Pressurized Release Experiments	90
5.2.1	50 psig (0.34 MPa) Test	91
5.2.2	250 psig (1.72 MPa) Test	98
5.3	Summaries and Conclusions	116
6	Fragmentation Analysis	119
6.1	Introduction	119
6.2	Two-Scale Model Approach	119
6.2.1	Macro-scale	120
6.2.2	Micro-scale model	122
6.3	Demonstration Problem	125
6.3.1	Macro-scale model	126
6.4	Results and Analysis	128
6.4.1	Macro-scale model	128
6.4.2	Micro-scale model	130
6.4.3	Combined two-scale model	131
6.5	Conclusions	132
7	Summary and Conclusion	133
7.1	Fuego Model Improvement	133
7.2	Resuspension Model Testing	133
7.3	Reanalyzing Fire Experiments	134
7.4	Powder Release Experiments	135
7.5	Fragmentation Analysis	137
8	Recommendations for Future Work	139
9	References	143
	Appendix A	149

FIGURES

Figure 2-1	Particle-wall interaction flow chart	26
Figure 2-2	Particle rebalance force balance	27
Figure 2-3	Simulation domain for wall impact test	30
Figure 2-4	Different diameter particle paths near the wall stagnation point	31
Figure 2-5	Different diameter particle paths in the inflow channel	32
Figure 2-6	Particle deflection at different diameters for particles that hit the wall	32
Figure 2-7	Resuspension test domain (cut in half), showing spray location	33
Figure 2-8	Size distribution of particles stuck on base surface at 1.5 seconds (blue) and 4.0 seconds with both the mean (green) and variable (red) shear stress models	34
Figure 2-9	Particle deposition pattern on base surface	34
Figure 2-10	Evaporation test domain	42

Figure 2-11 Time dependent evaporation of 2 component particles of various sizes (0.3mm – 2.7mm) at 3 different times (t = 1, 3.5, 6.5 sec).	44
Figure 2-12 Geometry for Evaporation Example 2.	45
Figure 2-13 Time dependent evaporation of particles of different sizes.	47
Figure 3-1 Schematic of the Human Activity Experiment [Fish et al. 1967].	51
Figure 3-2 ZnS Particle Spatial Distribution at 40 seconds.	52
Figure 3-3 ZnS Particle Spatial Distribution at 115 seconds.	53
Figure 3-4 Comparison of computed and measured resuspension factor.	53
Figure 4-1 Borkowski’s number vs. droplet size pdf. [Borkowski 1986]	56
Figure 4-2 Illustration of the predicted liquid droplet entrainment from one of the MS tests (Base 1) at 0.1 seconds, before ignition at 0.2 seconds.	59
Figure 4-3 An illustration of the predicted liquid droplet entrainment from one of the MS test scenarios (Base 1) at 0.3 s, following ignition at 0.2 s.	60
Figure 4-4 An illustration of the predicted liquid entrainment from one of the MS test scenarios (Late Base 1) late in the simulation.	60
Figure 4-5 Predicted mass of contaminant (UO ₂) deposited on pool surface, beaker side walls, and escape surface for the early period of the beaker-fire burn (Base 1).	61
Figure 4-6 Predicted mass of contaminant (UO ₂) deposited on pool surface, beaker side walls, and escape surface for the late period of the beaker-fire run (Late Base 1).	62
Figure 4-7 A flare-up event seen in one of the MS scenarios at late times in the simulation (Late Base 1).	62
Figure 4-8 ARF for all Scenarios starting at 20 mm (Base 1-5, Turbmod7 A-D, TurbMod8 A-D) or 40mm (Early Base 1-6) pool height without inclusion of the contaminant mass from the initial ignition pulse.	64
Figure 4-9 ARF for all Scenarios starting at 20 mm (Base 1-5, Turbmod7 A-D, TurbMod8 A-D) or 40mm (Early Base 1-6) pool height with inclusion of the contaminant mass from the initial ignition pulse.	65
Figure 4-10 Boiling scenario: Contaminant entrainment prediction, parcels enlarged for visualization.	70
Figure 4-11 Wind tunnel mesh: Geometry and surfaces.	71
Figure 4-12 Boiling: Predicted contaminant mass deposition vs time (1B).	74
Figure 4-13 Boiling: Predicted number deposition vs time (1B).	75
Figure 4-14 Predicted mass fate for heptane; boiling case 1 (1B).	75
Figure 4-15 Predicted mass fate for the contaminant; boiling case 1 (1B).	76
Figure 4-16 Predicted contaminant boiling atomization entrainment scenario: UO ₂ mass deposition.	76
Figure 4-17 Predicted and Reported Airborne Release Fraction.	77
Figure 4-18 Resuspension mechanism: (a) all particles have adhered to surfaces or exited the domain, and (b) resuspended particles have re-entered the flow. Particle size is exaggerated for visibility.	78
Figure 5-1 Free-fall Spill Experiments in RART [Sutter 1981].	82
Figure 5-2 Mesh used for Gravitational Spill Simulation, Containing ~10 Million Elements.	84
Figure 5-3 Two-Dimensional Mesh Near the Beaker (384 element mesh) at the Ceiling of RART.	85
Figure 5-4 Locations of the Filters and Impactors Relative to RART Dimension.	86
Figure 5-5 Particle Velocity Predictions from 3-m Spill Simulation at ~50 seconds.	87

Figure 5-6 Particle Velocity Predictions from 3-m Spill Simulation at ~200 seconds.....	88
Figure 5-7 Fluid Velocity Distributions from 3-m Spill Simulation at ~200 seconds.....	88
Figure 5-8 Fuego Simulation on the Particle Depositions at Various Locations (Ring location on the floor).....	89
Figure 5-9 Schematic of RART for Pressurized Release Experiment [Sutter 1983].....	90
Figure 5-10 Layout of PARE [Sutter 1983].....	91
Figure 5-11 Fuego Results on Particle Velocity for 50 psig (0.34 MPa) Pressurized Release of TiO ₂ at 5 seconds.....	94
Figure 5-12 Fuego Results on Fluid Velocity for 50 psig (0.34 MPa) Pressurized Release at 5 Seconds.	94
Figure 5-13 Fuego Results on Particle Velocity for 50 psig (0.34 MPa) Pressurized Release at 35 Seconds.	95
Figure 5-14 Fuego Results on Sampling Flow Effect for 50 psig (0.34 MPa) Pressurized Release at 35 Seconds.	95
Figure 5-15 Percentage of Particles Airborne Versus Deposited for 50 psig (0.34 MPa) Case..	96
Figure 5-16 Particles Deposition for the Ceiling Surface Treatment for 50 psig (0.34 MPa) Test – Central, Middle and Outer Cases.....	97
Figure 5-17 Comparison of Sampling Surfaces Treatment for 50 psig (0.34 MPa) Test – No Open and Filer Cases.	97
Figure 5-18 Mesh and Calculation Results for Initial Run.....	101
Figure 5-19 Mesh and Calculation Results for 2 nd Run.....	101
Figure 5-20 Finite Element Mesh for Final Run.....	102
Figure 5-21 Final State of Particles at end of Presto Calculation.....	103
Figure 5-22 Kinetic Energy of All Particles vs. Time.....	104
Figure 5-23 Case 1 Fuego Simulation.....	107
Figure 5-24 Case 2 particle velocities during initial burst into Fuego simulation, before momentum exchange and drag forces slow the particles.....	108
Figure 5-25 Case 2 stuck particles (PIS=0 is suspended, PIS=1 is stuck) and velocities at 1.0s.....	108
Figure 5-26 Case 3 particles showing the different sizes of particles at different times after injections.....	110
Figure 5-27 Case 3 particle and fluid velocities at impact with the ceiling of canister.....	110
Figure 5-28 Case 3 particle and fluids velocities after impact with the ceiling.....	111
Figure 5-29 Case 3 stuck particles (PIS=0 is suspended, PIS=1 is stuck) and velocities at time 200s.....	112
Figure 5-30 Case 4 particle and fluid velocities at impact with the ceiling of canister.....	113
Figure 5-31 Case 4 particle and fluids velocities after impact with the ceiling.....	114
Figure 5-32 Case 4 Percent Particles Suspended, Time 0-0.2s.....	115
Figure 5-33 Case 4 stuck particles (PIS=0 is suspended, PIS=1 is stuck) and velocities at time 200s.....	115
Figure 6-1 Graphical representation of the two irreversible linear decaying cohesive laws developed by Zhou and Molinari and Camacho and Ortiz [Zhou 2005].....	123
Figure 6-2 Examples of predicted average fragment sizes plotted with respect to strain rates in the case of an initially defect-free homogeneous bar [Zhou 2005].	124
Figure 6-3 Particle sized distribution resulting from UO ₂ pellet impact test (taken from [Jardine 1982]).....	126

Figure 6-4 Macro-scale finite element model mesh.	127
Figure 6-5 Fragmentation predicted by macro-scale finite element model.	128
Figure 6-6 Particle size distribution resulting from the macro-scale finite element model compared to the test data [Jardine 1982].	129
Figure 6-7 Failed element strain rate frequency plot.	129
Figure 6-8 Fragment size distributions and cumulative mass ratios resulting from micro-scale model simulations.	130
Figure 6-9 Particle size distribution resulting from the micro-scale model simulations compared to the test data [Jardine 1982].	131
Figure 6-10 Particle size distribution resulting from the combination of the macro- and micro-scale model simulations compared to the test data [Jardine 1982].	132

TABLES

Table 1-1 SIERRA Codes at SNL*	17
Table 1-2 Fuego Improvement Proposed for FY2016.....	22
Table 1-3 Recommendation for Modeling Mechanical Insult Accident Using SIERRA SM Code	22
Table 1-4 Recommendations on Modeling Pressurized Powder Release Simulations for FY2016	22
Table 2-1. List of particle-wall model components	26
Table 4-1 The simulation matrix showing all parameters varied in the simulations, including duration, particle data file used, turbulence parameters at the pool surface, and pool height.	58
Table 4-2 Entrainment mechanisms believed to be potentially active in this scenario.	67
Table 4-3 Turbulent boundary conditions for surfaces and scenarios.	71
Table 4-4 Vapor velocity for pool model at various times (baseline)	72
Table 4-5 Entrainment Scenarios.....	73
Table 4-6 Entrainment Simulation Variations	73
Table 5-1 Experimental Data for 100 g TiO ₂ , 3-m Free-fall Spill Test [Sutter 1981].....	82
Table 5-2 Source TiO ₂ * Powder Distribution in Measured Cumulative Mass Percent [Sutter 1981]	83
Table 5-3 Assumed Sampling Flow Rates.....	86
Table 5-4 Additional Simulation Assumptions.....	86
Table 5-5 Turbulence Parameters Used in the Spill Test	86
Table 5-6 50 psig (0.34 MPa) Test Simulation Assumptions.....	92
Table 5-7 50 psig (0.34 MPa) Test Simulation of Rupture Disk of PARE	92
Table 5-8 Turbulence Parameters Used in 50 psig (0.34 MPa) Test	92
Table 5-9 50 psig (0.34 MPa) Additional Simulation Cases	96
Table 5-10 Comparison of Particle Sizes and Number of Elements for All Runs	102
Table 5-11 250 psig Experiment Turbulence Parameters.....	106
Table 5-12 Particle Block Parameters for Fuego.....	109
Table 8-1 Fuego Particle Model Improvement Needs.....	139

NOMENCLATURE

1-D	One-dimensional
3-D	Three-dimensional
AED	Aerodynamic equivalent diameter
ARF	Airborne release fraction
ASC	Advanced Simulation and Computing
BC	Boundary condition
CFD	Computational Fluid Dynamics
DOE	Department of Energy
DR	Damage ratio
DSA	Document Safety Analysis
EDC	Eddy dissipation concept
EOS	Equation of state
FD	Fluid dynamics
FY	Fiscal year
GDE	Gradient damage explicit
HEPA	High efficiency particulate air
hr	Hour
IC	Integrated Code
ITAR	International Traffic in Arms Regulations
LES	Large-eddy simulation
LPF	Leak path factor
M	Mach number
MAR	Material-at-risk
mph	Miles per hour
MS	Mishima and Schwendiman
NRC	Nuclear Regulatory Commission
NSRD	Nuclear Safety Research and Development
ODE	Ordinary differential equations
PARE	Pressurized airborne release equipment
PDF	Probability Density Function
RART	Radioactive airborne release tank
PNL	Pacific Northwest Laboratory
RANS	Reynolds averaging of the Navier Stokes equations
RF	Respirable fraction
SD	Structural dynamics
SM	Solid mechanics
SNL	Sandia National Laboratories
SPH	Smoothed particle hydrodynamics
ST	Source term
TBP	Tributyl phosphine

Symbol – Applicable only for Section 2.1

A_p	Area of particle
C_μ	Turbulence wall model constant

D	Diameter described in Figure 2-6
E	Turbulence wall model constant
F_{adh}	Adhesion force
F_{lift}	Lift force
P	Probability function
a	Slope in Figure 2-6
k	Turbulent kinetic energy
m	Exponent in Figure 2-6
r_p	Radius of particle
u	Velocity
u_τ	Wall friction velocity
$u_{ }$	Fluid velocity component parallel to the wall
u'	Velocity variation
\dot{v}	Particle acceleration
t	Time
y^+	Dimensionless wall distance
α	Lift coefficient
ε	Surface roughness
ρ_f	Density of fluid
ρ_p	Density of particle
τ_w	Wall stress, $\overline{\tau_w}$, a time averaged value, τ_w' , a stress variation
μ_f	Viscosity of fluid
σ_u	Velocity variation standard deviation

Symbol – Applicable only for Section 2.2

B_{F-O}	Mass transfer number
B_{T-O}	Heat transfer number
C	Drag coefficient
C_p	Particle specific heat
H_s	Sensible enthalpy given in Eq. (2-34)
$H_{T\infty}$	Enthalpy of gas phase at gas temperature
H_{T_p}	Enthalpy of gas phase at particle temperature
LSODE	Solver
M	Mass, subscript F for evaporating (fuel)
M_p	Mass of particle
MW	Molecular weight, subscript NF for non-fuel, G for fluid, F for fuel, f for evaporating species
Nu	Nusselt number, subscript p for particle
P	Pressure, subscript vap for vapor, and ref for reference condition
P_{Ff}	Partial pressure of evaporating material (species)
Pr	Prandtl number, subscript p for particle
Q_{rad}	Thermal radiation heat
R	Ideal gas constant

$R_{\text{mdot,BTO}}$	Ratio of time derivative of species mass to heat transfer, Eq. (2-35)
Re	Reynolds number, subscript p for particle
Sc	Schmidt number, subscript p for particle
Sh	Sherwood number, subscript p for particle
T	Temperature, subscript p for particle, vap for vapor, and ref for reference condition
T_{crit}	Critical point temperature
T_{flame}	Flame temperature
$T_{\text{p,i}}$	Initial particle temperature
T_{∞}	Temperature at far field or fluid
X_{Ff}	Mole fraction for the evaporating species
Y_{Ff}	Mass fraction of evaporating species at film surface
$Y_{\text{F},\infty}$	Mass fraction of evaporating species in the fluid
$Y_{\text{F,p}}$	Mass fraction of the species in the particle and at the film
f_{BTO}	A parameter is given in Eq. (2-28)
f_{Buoy}	Buoyancy force
f_{D}	Drag coefficient
f_{Drag}	Drag force
g	Gravity
h_{vap}	Heat of evaporation, subscript ref for reference condition
r_{p}	Radius of particle
tol	Tolerance
v_{F}	Fluid velocity
$v_{\text{F,f}}$	Fluctuating fluid velocity
v_{rel}	Particle relative velocity
$v_{\text{p,c}}$	Current particle velocity
x,y,z	Cartesian coordinate
u,v,w	Velocity component corresponding to the Cartesian coordinate (x,y,z) respectively
$\frac{dM_{\text{F}}}{dt}$	Time derivative of current species mass
$\frac{dT_{\text{p}}}{dt}$	Time derivative of temperature associated with the particle species
$\frac{dx_{\text{p}}}{dt}$	Time rate change of position vector
ΔM	Particle/fluid mass difference
ρ_{p}	Density of particle
μ_{F}	Viscosity of fluid

Symbol – Applicable only for Chapter 4

$\rho_{\text{f/g}}$	fluid/gas/density
ρ	average density
ρ_{X}	density of species X

j_g	superficial gas velocity
j_{fe}	superficial liquid drop velocity
α	particle lift coefficient
A_p	particle cross-sectional area
τ_w	wall shear stress
r	particle or pool radius
V	volume
ε	surface roughness
E_{fg}	entrainment factor (droplet/gas)
Y_X	mass fraction of X in gas phase

Symbol – Applicable only for Chapter 6

σ	Cauchy stress tensor
σ_1	Maximum principal stress
σ_1^u	Maximum principal stress for the undamaged material
$A(d)$	Stiffness function
D or d	Damage number included between 0 and 1
I	Identity tensor
λ, μ	Lame constants
ν	Poisson's ratio
ϵ	Green-Lagrange strain tensor
ϵ^+, ϵ^-	Positive and negative components of the strain tensor
$\dot{\epsilon}$	Strain rate tensor
P	Matrix built from the eigenvectors of the Green-Lagrange strain tensor
Λ	Diagonal matrix of principal strains
Λ^+	Diagonal matrix whose values consist of the max between the principal strain and zero
ξ_i	Principal strain with $i=\{1,2,3\}$
p	Parameter influencing the shape of the stress decay following the initiation of damage
m	Parameter expressed from the modulus of elasticity, the fracture energy, the fracture stress and the phase regularization length
E	Material's modulus of elasticity
L	Phase regularization length
L_e	Characteristic element length
G_c	Critical fracture energy
σ_c	Critical fracture stress
η	Phase viscosity
$\hat{\Psi}$	Driving energy
ψ^+	Driving energy for the undamaged material
c, k	Constants depending on both the fracture energy and the phase regularization length
R	Random number drawn from a uniform distribution between 0 and 1
b	Weibull shape parameter
$\bar{\mu}$	Weibull median
w	Element's total mass
L_{bar}	Length of the bar used in the micro-scale model
σ_0	Uniform axial stress

ϵ_0	Uniform uniaxial strain
$\dot{\epsilon}_0$	Uniform uniaxial strain rate
σ_{coh}	Cohesive uniaxial stress
δ_{coh}	Current crack opening distance
δ_c	Critical crack opening distance
δ_{max}	Maximum crack opening distance

1 INTRODUCTION

Safety analysts throughout the U.S. Department of Energy (DOE) complex rely heavily on the data provided in the DOE Handbook (referred to herein as the Handbook), DOE-HDBK-3010 [DOE 1994], to determine radionuclide source terms (STs) in support of safety and risk analyses in documented safety analysis (DSA) or risk analysis documents. In calculating source terms, analysts tend to use the Handbook’s bounding values on airborne release fractions (ARF) and respirable fractions (RF) for various categories of insults (representing potential accident release categories). This is typically due to both time constraints and the avoidance of regulatory critique. Unfortunately, these bounding ARF/RFs may represent extremely conservative values. Moreover, they were derived from very limited small-scale and bench/laboratory experiments, as well as from engineering judgment which may not have been substantiated. Furthermore, these previous estimates may not be representative of the actual accident conditions and configurations under consideration. In response, we have proposed including high-fidelity modeling to provide a more accurate and defensible method to identify not only bounding values, but also more representative values that can be used by analysts tasked with risk assessments.

Advances in computing capability at national laboratories have enabled us to use computer simulations to better model hydrodynamic, structural dynamic, and thermal/fluid dynamic phenomena. This provides a better understanding of the insights on the fundamental physics related to potential accident scenarios that could occur or could be postulated. Today, the availability of the high-fidelity computer resources (both hardware and software) that incorporate state-of-the-art models at national laboratories allows safety and risk analysts to utilize these methods for non-weapon-related safety activities. An example of the use of these state-of-the-art models in supporting source term calculations and in particular ARFs for postulated scenarios is the SIERRA high fidelity codes developed at Sandia National Laboratories (SNL). The SIERRA codes are designed to solve multi-physics engineered problems, particularly for weapon applications (see Table 1-1). The recent study performed on spent fuel processing source terms for the Nuclear Regulatory Commission (NRC) indicates that SIERRA codes can be used to provide ARF/RF for a red oil explosion accident [Gelbard 2013].

Table 1-1 SIERRA Codes at SNL*

Module/Code Name	Description	Potential Application
Solid mechanics (SM) [SIERRA 2016a]	<p>A three-dimensional solid mechanics code with a number of features: versatile element library, nonlinear material models, large deformation capabilities, and contact.</p> <ul style="list-style-type: none"> • Adagio –The standard SM code that currently provides the full suite of both explicit and implicit capabilities. In the past, the SM code for solving problems in explicit and implicit capabilities was separated into Presto and Adagio, respectively. Thus, Presto executable became obsolete. • Presto_itar – This SM code version provides capabilities to material models with an energy-dependent pressure response, such as for very large deformations and strain rates and for blast modeling [SIERRA 2016b]. The use of this code version falls under the U.S. Department of State’s International Traffic in Arms Regulations (ITAR) export-control 	May be used to model impacts, large deformation of solids, powders, and liquid dispersals using a smoothed particle hydrodynamics (SPH) model.

	<p>rules. Many of the material models in this version are similar to those models in CTH code.****</p> <ul style="list-style-type: none"> • Peridynamics – an extension of the SM code for modeling classical solid mechanics problems, such as the modeling of bodies in which discontinuities occur spontaneously. 	
Structural dynamics (SD)	<p>Used to perform most traditional structural dynamics simulations in time and frequency domains, including stress and fatigue calculations. These calculations could include energy dissipation at discrete joints. Since this SD module has a massively parallel capability, it can efficiently perform simulations to millions of degrees of freedom. Its variety of equations solvers enables solving problems with a large number of constraints. This module also includes a structural-acoustics capability for simulating noise-induced structural vibration or response due to a given noise source [SIERRA 2016c].</p>	<p>May be used to determine the failure of the structural-related components in the problem. No apparent applications for this research at this time.</p>
Thermal Analysis**	<p>Aria, Calore, and Chaparral modules comprise the state-of-the-art thermal analysis tools using massive parallel capability:</p> <ul style="list-style-type: none"> • Aria is a Galerkin finite element-based program for targeting applications that involve incompressible flow and primarily focus on energy transport; species transport with reactions; electrostatics; and the general transport of scalar, vector, and tensor quantities in two and three dimensions for both transient and direct-to-steady state. • Calore approximates linear and nonlinear continuum models of heat transfer. • Chaparral is a library package to address three-dimensional enclosure radiation heat transfer problems. 	<p>May be used to determine situations requiring detailed thermal analysis. No apparent applications for this research at this time.</p>
Fluid dynamics (FD) with low Mach**	<p>Fuego*** is an FD module for the SIERRA code suite. Fuego is designed to predict low-Mach number ($Ma < 0.3$) reacting flows, and has a capability to model particle and drop transport using a dilute spray approximation Lagrangian/Eulerian coupling. The liquid phase can be modeled as individual Lagrangian drops that interact through momentum source terms with the Eulerian gas phase. It couples with Syrinx, a media radiation heat transfer module, to simulate a more complete heat transfer and FD problems, such as fires. Fuego models particles in terms of user input or code generated as in soot from a fire. With the particle capability, it can model particle dispersal; however, Fuego does not currently model particle interaction, which is important for the particulate release out of a pathway.</p>	<p>Useful to model fire with particulates and droplet/powder release due to an elevated pressure effect.</p>
Fluid dynamics (FD) with high Mach**	<p>Aero module that can model flow problems at Mach numbers in excess of Mach 8. It can model gas flow in two and three-dimensional problems, which can approximate the compressible Navier-Stokes equations on unstructured meshes.</p>	<p>Useful to model deflagration types of accidents, particularly their flow conditions. Aero currently does not have a particle model, and thus has no apparent applications for this research at this time.</p>

*see [SIERRA 2016] for more details on the specific module description and usage. This suite is compliant to DOE Order 414.1D [Minana 2012].

**These codes and modules make up the SIERRA Thermal Fluid (TF).

***[SIERRA 2016d]

****<http://www.sandia.gov/CTH>

This report will summarize our research on the application and use of these types of codes in determining ARFs in our first two years of funding. If our research determines that the data are

too conservative, the DSA source term may over-specify the implementation of design and operating controls, which may lead to substantial design, construction, and/or implementation costs to DOE. On the other hand, if our research determines the data that are non-conservative, this means that the DSA underestimates the source term, which could translate to a potentially significant safety concern to the workers and to the public. In either case, the results of our investigation could enhance how safety analysts across the DOE complex approach the selection of adequate bounding ARFs/RFs. This should improve both the defensibility of the safety analyses and the confidence level of these data.

This research was funded by DOE Nuclear Safety Research and Development (NSRD) Program starting in FY2015. At the end Year 1, we documented our research in a SAND report [Louie 2015]. In this report, we will discuss our accomplishments in this fiscal year (FY). In the next two sections, we will summarize what was accomplished in Year 1 of the project. Then we will discuss our tasks in FY2016. Finally, we present our accomplishments in FY2016.

1.1 Accomplishments in FY2015 (Year 1)

At the end of Year 1, we published a final report to document our accomplishments [Louie 2015]. In this report, we summarize Year 1 accomplishments based on the tasks assigned:

- Simulate the liquid fire experiments in the Handbook.
- Conduct exploratory simulations, such as an object hitting a can filled with powders, and pressurized release experiments from the Handbook.

1.1.1 Liquid Fire experiments

For the beaker fire, there were 25 ml of kerosene with 30% Tributyl phosphine (TBP) and contaminants in a beaker and a chimney apparatus to ensure no cross-flow [Mishima 1973]. A Fuego model (see Table 1-1) was developed for droplet entrainment during the boiling for the release of the contaminants. An initial droplet size distribution was employed to model droplet breakup during rising bubbles. The simulations included a number of parameter variations, such as the initial liquid height and turbulence induced at the boiling surface. The sensitivity to the initial fuel height was significant, since results indicated that this parameter is closely related to the airborne release. The aerosol release for a 20 mm initial liquid height showed reasonable agreement with the data. Beaker wall deposition was also observed in the simulations. Since Fuego does not currently have a liquid level depletion model, no resuspension is used. The beaker simulation study identified these major findings:

- Liquid height might influence the release of contaminant, a parameter not considered in the experiments.
- The effect of flow turbulence was not particularly significant.
- Much of the airborne release was predicted to occur at the beginning of the simulations during the ignition.

In addition to the beaker fire, a gasoline pool fire with ~20 g of UO₂ powder was simulated using Fuego [Mishima 1973a]. For this experiment, a steel pan was located inside a wind tunnel, in

which gasoline contaminated with UO_2 was allowed to entrain. In this simulation series, a number of entrainment phenomena were considered in the model such as evaporation induced entrainment (EIE) and agitation by boiling (similar to that in the beaker fire). Although wind can be important for resuspension, this aspect of these tests was not simulated because Fuego currently does not model resuspension. In subsequent work (FY2016), we planned to implement and test a resuspension model. As demonstrated in the gasoline pool fire simulation, the deposited mass on the walls of the wind tunnel is small compared to the outflow of the airborne materials. The magnitude of the EIE is very small in comparison to the boiling. All cases were found to have higher ARF values than that of the experiments, but this was driven by the assumed boiling time. Better assessments of the boiling time are needed.

The major conclusions for the pool fire simulation series are listed below.

- The entrainment mechanism of surface agitation by boiling significantly dominated the entrainment during flaming.
- Turbulence boundary conditions were not reported, and a practical range of assumptions results in significant uncertainty in the ARF for the above entrainment mechanisms.
- The boiling mechanism was found to be the significant contributor to the amount of entrained mass. Modeling of particle entrainment from pool boiling will improve the modeling accuracy.

1.1.2 Exploratory Simulations

In addition to these fire simulations, exploratory simulations were also conducted to identify if SIERRA codes can be used to model solid particle entrainment.

For a projectile impacting a can filled with UO_2 powder, the simulations for the powders included the use of the Mie-Gruneisen Equation of State (EOS) Model [SIERRA 2016b] and the Soil-Crushable Foam material model [SIERRA 2016a].

Two simulation impact speeds of 20 m/s and 175 m/s were conducted. Two mesh models (coarse and fine) were also used for the simulation. A total of five cases were simulated. In general, a 20 m/s impact velocity of the projectile would puncture a hole in the can, which leads to powder escaping. At this velocity, the can remains stationary while the projectile rebounds. On the other hand, when the impact speed increases to 175 m/s, the projectile penetrates the can and becomes lodged inside while the can flies upward. During can lofting, particles escape through the opening. Eventually, the can falls back and hits the floor again. During this time, additional release near the bottom of the can was observed in the simulation. This release may not be realistic. Therefore, additional 20 m/s impact velocity cases were simulated to observe this secondary release. Only cases with the Mie-Gruneisen EOS material model were observed to have this behavior. The use of the Soil-Crushable Foam material model did not exhibit the secondary release. Perhaps the Mie-Gruneisen EOS material model may not be appropriate for low impact speed scenarios; it may instead be appropriate for explosion simulations or high-impact velocity simulations where shocks are developed. Further analysis of this behavior for the Mie-Gruneisen EOS model may be needed. On the other hand, the Soil-Crushable Foam material model is useful for modeling the impact from an accident.

The major conclusions for this projectile impact case are listed below.

- SIERRA SM code can be used to simulate solid entrainment by the use of a SPH model.
- The use of Mie-Gruneisen EOS material model should be limited for shock related impact type of accidents.
- The use of a Soil-Crushable Foam material model is useful for modeling impact accidents.
- The use of coarse and fine mesh models for the same simulation model suggests that the model may behave well.
- Problems with a longer duration are needed to observe unrealistic model results.

The other powder simulations involved the pressurized release from a container to a containment type volume [Sutter 1983]. Here, because of known limitations of Fuego's model for particle interactions, the MELCOR code was also used. Although MELCOR is a system-level code, it contains an aerosol physics model [Humphries 2015]. Because the MELCOR aerosol physics model is based on concentrations of the airborne aerosol, multiple volumes were required. A single volume model and a two-volume model have been developed. Two pressure cases were simulated (50 psig and 250 psig). A better modeling method is needed to include this exchange.

A preliminary Fuego model was developed to simulate the 50 psig case of the experiment. Although the surfaces for the model are assumed to re-bounce rather than stick in a 60-second run showed the impingement of the particles on the ceiling. This result is consistent with the experimental results.

The major conclusions for the pressurized powder release simulations are listed below.

- Although MELCOR is a system-level code with a concentration based on aerosol physics model, it can be used to simulate this type of experiment.
- Fuego, on the other hand, has been used to model fires as described in Section 1.1.1. This FD code can be extended to model pressurized powder release.
- Fuego may not be appropriate for modeling high pressure conditions since it is designed for low-Mach flow.
- Although Fuego currently does not have a particle interaction model, it can be used to identify the particle impingement to walls and ceilings.

Note that these exploratory simulations were intended to demonstrate the code's capability in FY15. At this stage, the simulations are not intended to be compared to experimental results. Further analyses of scenarios using MELCOR and Fuego for pressured powder release are to be continued in subsequent work (in FY16).

In the recommendation from Year 1, the following three tables summarized the further work needed. Table 1-2 lists the Fuego improvement proposed for this year. Table 1-3 provides the

recommendations for modeling mechanical insults using the SM code. Finally, Table 1-4 lists the recommendations for simulating powder release experiments conducted. Many of the code improvement and recommendations were accomplished in FY2016 (see Section 1.2). However, no further study was made for the recommendations described in Table 1-3.

Table 1-2 Fuego Improvement Proposed for FY2016

SIERRA FD code (Fuego) Recommendation	Potential Benefit
Multicomponent particle capability	This capability is particularly useful when fuel and solids (contaminants) are mixed, allowing fuel to evaporate while solids remain during the fire
Resuspension of particle capability	This capability is important for resuspension of deposited materials from the walls or burn residues resuspended under wind conditions

Table 1-3 Recommendation for Modeling Mechanical Insult Accident Using SIERRA SM Code

Model and Simulation Improvement	Potential Benefit
Mie-Gruneisen EOS Material Model	This model should be used with caution, particularly with the SPH capability for modeling particle dispersal. It should only be applied to explosion simulations and high-velocity impact cases where shocks can be developed. In addition, this model is only available in Presto (ITAR version) of the SIERRA SM code. Discussions of the model and results are limited.
Soil-Crushable Foam Material Model	This material model should be suitable for modeling low-velocity impact cases as described in Section 1.1.2. It tends to be stable in comparison to the Mie-Gruneisen EOS model above for the same simulation model. Unlike the Mie-Grunesien EOS model, this material model can be obtained from Adagio, which may not be restricted in terms of export controls.

Table 1-4 Recommendations on Modeling Pressurized Powder Release Simulations for FY2016

Model Improvement	Potential Benefit
Multi-volume MELCOR model	This multi-volume MELCOR model may improve results with the experiment since the aerosol physics model depends on concentration.
Flow of Air exchange during experiment needed to be included in MELCOR model	During the aerosol measurement, air inside the containment volume was exchanged 80 times. This exchange may improve MELCOR model results with experimental data.

Refined Fuego model	Proper modeling of the experiments is needed, including those described in the MELCOR model improvement above. This would improve the particle deposition results on the walls and ceiling of containment.
Fuego/MELCOR Coupling	Since Fuego currently does not model particle interactions, the Fuego results, particularly for the wall and ceiling deposition, can be used in conjunction with MELCOR results to compare with the experimental data. This coupling would improve the calculation results to experiments.
Adagio/Fuego/MELCOR Coupling	As described in this research, Fuego can only model pressurized powder release with a 50 psig pressure. To model higher pressure cases, the use of the SPH particle model in Adagio may be required. The results of Adagio are then used by Fuego to predict impingement. Finally, the results are used in MELCOR to determine the final results to compare with the experiments.

1.2 Tasks in FY2016 (Year 2)

In this year, as reported here, we proposed to do the following:

- To improve Fuego code by implementing a particle resuspension model, and multi-component evaporation model as recommended in year one. Note that the implementation of the resuspension model was proposed to be a user subroutine. However, through the discussion with the code developers, it was best to implement the model through a user function with all physics associated with the model implemented by the code developer.
- To test these new models, we have added experiments and are re-analyzing the previous simulations from Year 1.
 - To model a resuspension experiment documented in the Handbook
 - To re-analyze the beaker and gasoline pool fire experiments as conducted in Year 1.
- To improve the Fuego models to simulate the previously analyzed, Year 1, pressurized release experiments.
 - We also added a simulation on the release of powder from a gravitational spill using the same containment as in the pressurized release experiments.
 - Note that there will be no MELCOR simulation discussions in this report, since MELCOR simulations are covered in a separate NSRD project report [Louie 2016].
- To examine and develop an approach to address solid fragmentation through the simulation of an impact of a falling weight onto a brittle ceramic as an exemplar problem. The exemplar problem is representative of the impact experiment described in ANL-82-39 [Jardine 1982] that is referenced in Section 4.3.3 of the Handbook.
 - The model exercised is a two-scale model simulating the drop of a weight onto a cylindrical ceramic specimen.

- At the macroscale, the model uses a continuum elastic fracture material model formulation with element strength degradation (found in Sandia’s explicit transient dynamics SIERRA/SM) to simulate the dynamic fracture of the cylinder. Results from the macroscopic calculations are passed to a one-dimensional lower length scale model that incorporates the relevant fine scale effects to determine the micro-scale fragmentation.
- This one-dimensional (1-D) micro-scale fragmentation model simulates the internal crack nucleation and opening processes to predict the average fragment size and the fragment size distribution as a function of the material properties, loading conditions, and microscopic characteristics length scale of the material.

This report is divided into seven chapters. Fuego code improvement is discussed in Chapter 2, which documents both the development of the particle resuspension and multi-component evaporation models. Chapter 3 provides the testing of the particle resuspension model. Chapter 4 describes and discusses the re-analysis of two previous liquid fire experiments documented in Year 1. Chapter 5 re-analyzes the powder release experiments with better modeling improvement compared to work done in the previous year. Chapter 6 provides a description of the two-scale modeling approach applied to the simulation of the brittle fracture experiments. Chapter 7 describes the summaries, conclusions and recommendations. Chapter 8 provides the recommendation for future efforts, including a description of the tasks to be investigated in FY2017. Appendix A provides a summary table of Handbook data. Note: the summary table is an “in-progress” table, which means that it would be updated as more substantiating studies in this project are done with the data in the Handbook.

2 FUEGO MODEL DEVELOPMENT

As a part of the code improvement task in Year 2, the FUEGO code [SIERRA 2016d] has been improved by adding two particle related models. The first model relates to the particle resuspension capability, which allows the particles deposited on the surface to be suspended back into the atmosphere. The second model relates to the evaporation of the liquid drop that consists of a number of components, such as liquid fuel and contaminants. Both models were identified by Year 1 activity described in the introduction section of this report.

This section describes the two model developments. The first subsection describes the resuspension model development and second subsection describes the multi-component evaporation model development.

2.1 Resuspension Model Development

Of particular interest to this work is the scenario where airborne particles settle on a surface and then the settled particles are disturbed by airflow or mechanical agitation. In such a scenario, the resulting airborne particle distribution can depend strongly on the physical configuration and agitation method.

The primary focus of this work is for solid particles. Resuspension considerations for liquid particles would require different adhesion models based on surface tension and wetting angle to be appropriate. Such models can be implemented in the given framework, but are not the focus here. In this section we describe the implementation and demonstration of the new particle resuspension models in the SNL code SIERRA/FD (Fuego), which is a low-Mach number fluid mechanics Computational Fluid Dynamics (CFD) code targeting fire simulations and particle transport [SIERRA 2016d].

2.1.1 Model Overview

The motion of inertial particles in SIERRA/Fuego is modeled using a spherical drag model to form a set of ordinary differential equations governing the motion of Lagrangian particles. There is two-way coupling between the particle motion and the fluid motion on the background mesh. The fluid velocities at each time step are interpolated to the particle position along with relevant fluid properties. If applicable, the velocities are perturbed based on the turbulent kinetic energy to provide a stochastic representation of the effect of sub-grid eddies on particle motion. The particle movement then produces an accumulated momentum source which is applied back to the fluid to be solved. For more complex particles (e.g. non-isothermal or multi-component), a similar two-way coupling is also used for the energy and species equations.

The sphere drag force model defines the particle's motion in the fluid domain, but when a particle impacts a domain boundary there are several options available to treat that interaction which depend on the properties of both the particle and the boundary. Each domain boundary can have both a reflection model and an adhesion model applied to it. When a particle actually hits a boundary, the logic outlined in Figure 2-1 is used to determine the appropriate response based on which reflection and adhesion models are used on that boundary.

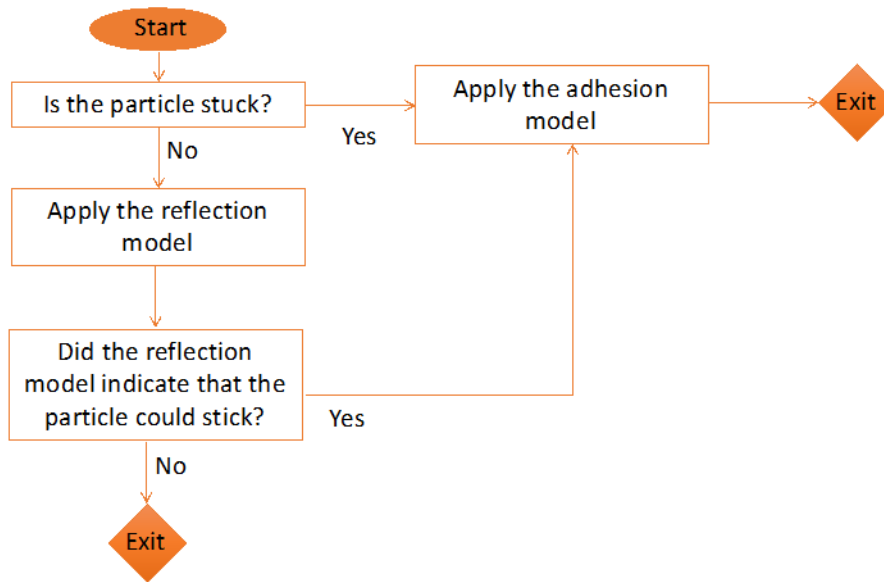


Figure 2-1 Particle-wall interaction flow chart.

The available reflection and adhesion models are listed in Table 2-1. Since the reflection model is evaluated first (per the flow chart above) it determines whether the particle can adhere to the boundary or not. For example, the “Rebound” model will always result in the particle rebounding off the boundary, while the “Rebound Yoon” and “Shatter Brown” models (see Section 2.1.1.4) use the Weber number and other local criterion to determine whether the particles rebound, shatter, or potentially stick to the boundary. The models developed for this work are the two resuspension models listed in the “Adhesion Models” column.

Table 2-1 List of particle-wall model components

Reflection Models	Adhesion Models
None	None
Rebound	Stick
Rebound Yoon	Resuspend Wichner
Shatter Brown	Resuspend Generic

2.1.1.1 Basic Resuspension Model

The determination of whether a particle will re-suspend or remain stuck to the wall is done using a force balance on the particle (Figure 2-2).

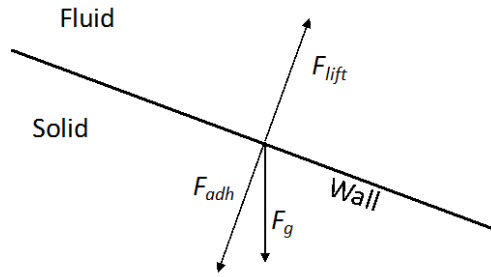


Figure 2-2 Particle rebalance force balance.

The Wichner resuspension model is based on equations derived by Wichner [Young 2015], and can be described in this force balance context using the following force models:

$$F_{\text{lift}} = \alpha A_p \tau_w \quad (2-1)$$

$$F_{\text{adh}} = 10^{-9} \frac{r}{\varepsilon} \quad (2-2)$$

where α is a lift coefficient (nominally 5.0), τ_w is the wall stress and ε is the surface roughness. Unlike the original form by Wichner, we also consider gravity forces in our model (Figure 2-2).

Because of the empirical nature of the above force terms (being representative for only specific datasets), we have chosen to implement the force terms generally, so the lift and adhesion force can be specified individually at runtime as any arbitrary function of A_p , τ_w , $\overline{\tau_w}$, k , r_p , μ_f , ρ_f , ε , t , and $\partial \overline{\tau_w} / \partial t$. The overbar on wall shear stress indicates a time average, while the value of τ_w includes *turbulent* variations, described in a subsequent section.

2.1.1.2 Stochastic Resuspension Model

One limitation of the basic resuspension model described above is that it does not have a mechanism to account for variations in particles other than diameter (e.g. shape or aspect ratio) or variations in local surface properties. To account for this, we introduce a resuspension probability function that can depend on any of the variables the lift and adhesion force depend on. When the resuspension probability function is active, each particle is assigned a random number from a uniform distribution between 0 and 1. The force balance shown in Figure 2-1 is still applied first to see whether a particle could re-suspend. If so, the resuspension probability is calculated at the current conditions and if the calculated probability is greater than the particle's random number the particle is removed from the surface, re-inserted into the fluid flow, and assigned a new random number. For example, one could use a force-based version of this probability function, defined as

$$P = 1 - \exp\left(-\frac{F_{\text{lift}}}{F_{\text{adh}}}\right), \quad (2-3)$$

where the lift and adhesion forces used here are those defined in [Young 2015] (Eqns. 2-1 and 2-2).

2.1.1.3 Wall Shear Stress Calculations

The wall shear stress used in the resuspension calculations described previously is calculated at the walls using models which depend on the selected turbulence model to be solved during the fluid mechanics iteration. When considering laminar flow, no wall models are used and wall shear is simply

$$\tau_w = \mu \frac{\partial u}{\partial y}. \quad (2-4)$$

For turbulent simulations, an appropriate wall model is used to determine the wall friction velocity (u_τ), which is used to calculate wall shear stress as

$$\tau_w = u_\tau^2 \rho_f \quad (2-5)$$

The friction velocity can be calculated either assuming local equilibrium between production and dissipation, as

$$u_\tau = C_\mu^{0.25} \sqrt{k} \quad (2-6)$$

Or using Newton iteration to solve

$$\frac{u_{||}}{u_\tau} = \frac{1}{\kappa} \ln(Ey^+) \quad (2-7)$$

Since y^+ also depends on u_τ .

To model the effects of turbulence in the fluid flow on particle motion, fluid velocity the particle experiences is perturbed by a normal distribution with zero mean and a standard deviation based on the local turbulent kinetic energy. The standard deviation of this distribution is calculated from the expression for the velocity variation (u') as

$$u' = \sigma_u = \sqrt{\frac{2}{3}k}. \quad (2-8)$$

In order to apply a similar effect to the wall shear stress, we leveraged the experimental data [Keirsbulck 2012] from which the wall shear stress variation was measured as a function of friction velocity ranging from 0.015 to 0.08 m/s in a 1 by 15 cm rectangular duct with centerline velocities ranging from 0.26 to 1.6 m/s. Fitting a logarithmic relationship to their results gives the relative wall shear stress variation as

$$\frac{\tau_w'}{\tau_w} = 0.0375 \ln(u_\tau) + 0.482. \quad (2-9)$$

2.1.1.4 Model Input Description

This section duplicates descriptions from the Fuego input section on the particle wall interaction models in the code manual [SIERRA 2016]. See Table 2-1 for the list of the keywords used in the interaction models.

Particle-wall interactions are specified in Fuego using a reflection model and an adhesion model. When a particle impacts a wall, the reflection model is called first to determine if it reflects or shatters. If not, then the adhesion model is called to determine if it sticks, re-suspends, or is

simply removed from the simulation and accumulated on the wall in a scalar field. The various models available are described in the following:

Reflection Models

The no reflection model does no calculations and simply moves on to the adhesion model for every impact. It is specified by:

REFLECTION MODEL = NONE

The rebound model causes the incoming particle to rebound at an angle based on its incident angle. It never calls through to the adhesion model. It is specified by:

REFLECTION MODEL = REBOUND

The Yoon rebound model uses a conditional rebound for liquid particles and always rebounds for solid particles (see additional options and keywords in [SIERRA 2016]).

REFLECTION MODEL = REBOUND_YOON

The Brown shatter model uses Mundo condition for shattering for liquid particles. Solid particles impacting a wall with a shatter model are simply rebounded. A detailed explanation and keywords used for this model is explained in [SIERRA 2016].

REFLECTION MODEL = SHATTER_BROWN ... keywords

Adhesion Models

The no adhesion model simply deletes the particle and accumulates it in the scalar accumulation variables on the surface. This reproduces the behavior of both the old STICK and PASS_THROUGH interaction types. It is specified using:

ADHESION MODEL = NONE

The stick model is similar to the no adhesion model, except the particle is not deleted from the simulation, but remains on the surface and is marked as stuck. It is specified using:

ADHESION MODEL = STICK

The Wichner resuspension model described in Eqs. 2-1 to 2-2 allows the resuspension of the deposited particles. A number of keywords and parameters are specified (see explanations and options in [SIERRA 2016]).

ADHESION MODEL = RESUSPEND_WICHNER ... keywords

The Generic resuspension model is a superset of the Wichner model described previously. Instead of hardcoding the form of the lift and adhesion forces as described in the Model

Overview section above, they are specified by the user in the input file. See [SIERRA 2016] for the detailed description of the parameter inputs.

ADHESION MODEL = RESUSPEND_GENERIC ... keywords

2.1.2 Model Testing

In this section, we present two test cases to demonstrate the resuspension model and wall-interaction capabilities. The first test case is used to examine particle size dependence of wall impact with a perpendicularly impinging laminar jet on a wall (absent gravity forces). The second demonstration case involved depositing a log-normal size distribution of particles on a surface and blowing an air jet over the particles at a velocity calculated to produce a high enough wall shear stress to remove particles from the wall.

2.1.2.1 Wall Impact Testing

The wall impact test uses a T-shaped channel with a 0.5 m/s air inflow, a channel width of 3 cm, a uniform mesh size of 1.5 mm, and no gravity forces (see Figure 2-3). The particle momentum effect on the fluid is disabled so that a large number of particles can be inserted consistently into a developed flow field without affecting the fluid motion. A set of particles with a uniform material density of 1 g/cm³, initial velocities of 0.5 m/s aligned with the jet direction, and diameters ranging from 100 nm to 1 cm are inserted 4 mm off-center (towards one of the outflow branches) in the inflow channel at 1.5 seconds into the simulation (after the fluid flow has had time to develop) and their trajectories tracked along with the fluid streamline they are inserted on.

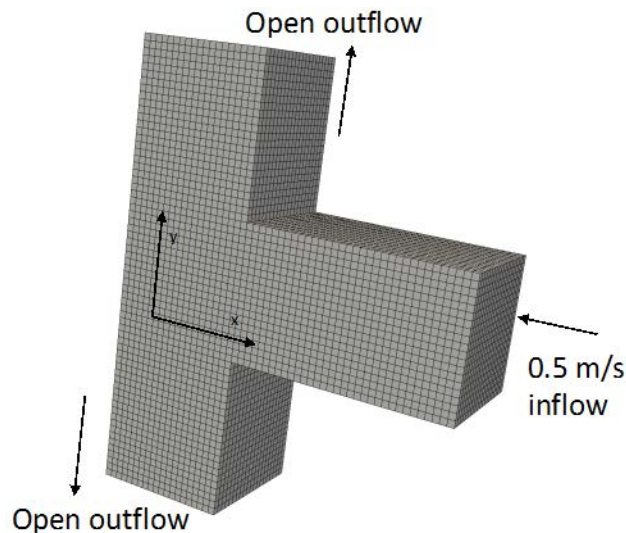


Figure 2-3 Simulation domain for wall impact test.

It is expected that the large particles will have minimal fluid-induced deflection from their initial trajectory and will hit the back wall, while small particles will closely follow the fluid streamline out of one of the domain open boundaries. Intermediate sized particles will have some deflection from the fluid streamline and may impact the wall, or may escape the domain.

To look at the effect of particle diameter on wall impacts, the particle paths were plotted for all diameters along with the fluid streamline that the particles are inserted on. These paths are shown in the near-wall region in Figure 2-4. In this case, the smallest particle that stuck to the wall had a diameter of 80 μm . All smaller particles were deflected enough by the flow to avoid the wall and leave the simulation domain.

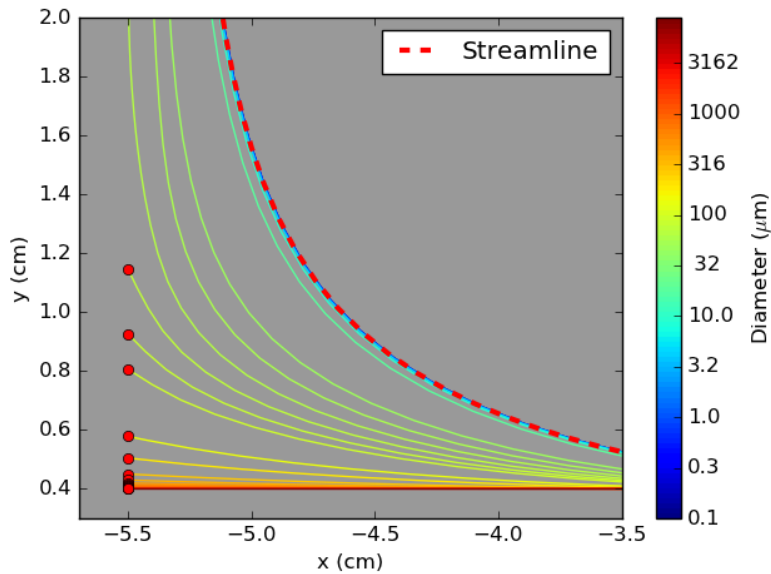


Figure 2-4 Different diameter particle paths near the wall stagnation point.
Stuck particle locations are shown with red circles (along the wall located at $x = -5.5$ cm).

The particles were inserted at an x coordinate of 2 cm, and their path down the inlet channel is shown in Figure 2-5. The small particles here (below about 10 μm) do not significantly deviate from the fluid streamline, and the large particles (above about 300 μm) do not significantly deviate from their initial trajectory. The implication of this result is that small particles (less than 10 μm) are unlikely to impact the wall without the addition of external forces since the fluid streamlines by definition will not intersect a closed boundary. We currently have the ability to include gravity/buoyant forces on particles, but to improve the simulation accuracy of the motion of small particles near walls we would need to include additional physical phenomena, such as boundary layer entrainment, electrostatic forces, and Van der Waals forces.

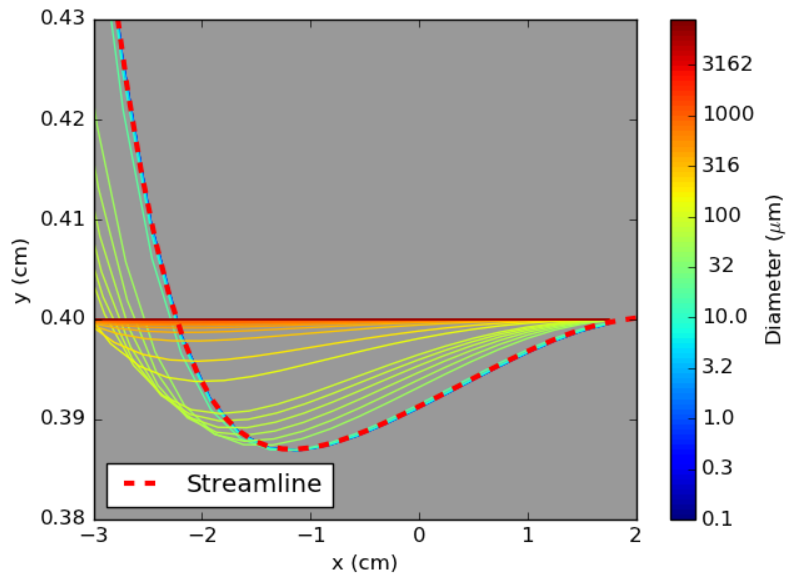


Figure 2-5 Different diameter particle paths in the inflow channel
 (note the y-axis scale difference between this figure and the previous figure).

Finally, we compared the particle deflection with its diameter for the subset of particles that hit the wall (those with 80 μm and larger diameters) in Figure 2-6.

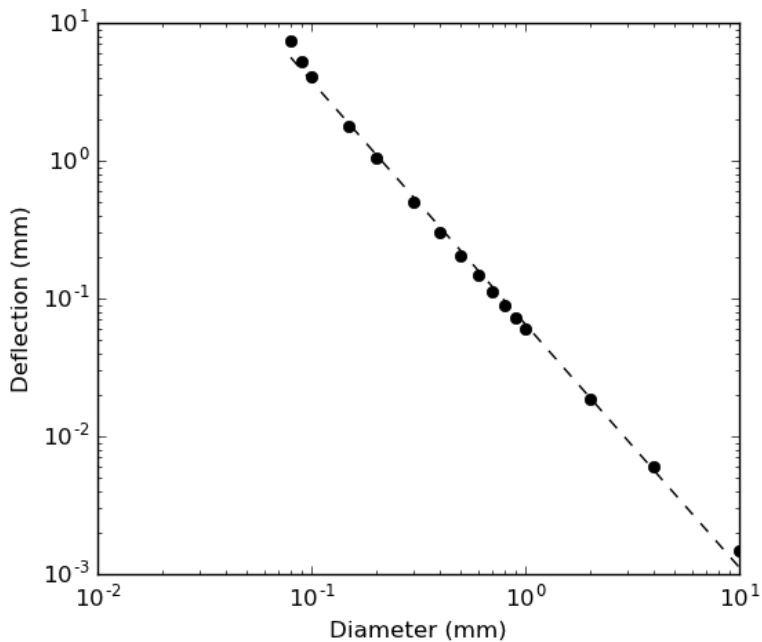


Figure 2-6 Particle deflection at different diameters for particles that hit the wall
 (dashed line is a fit of $y = aD^m$ with $m = -1.76$).

The data in this figure shows an inverse of diameter proportionality constant of 1.76 for the particle deflection in this simulation. The acceleration on a spherical particle at low particle

Reynolds numbers (Eq. 2-10) is a combination of two terms that are proportional to D^{-2} and $D^{1.33}$, so the value obtained here lies within the expected bounds.

$$\dot{V} = \frac{6\pi r \mu_f \Delta \bar{v} \left(1 + \frac{1}{6} \left(\frac{2\rho_f |\Delta v| r_p}{\mu_f} \right)^{2/3} \right)}{\frac{4}{3} \pi r_p^3 \rho_p} \quad (2-10)$$

2.1.2.2 Wall Adhesion Testing

To test the particle resuspension capability, we devised a notional scenario that involves a physical domain with a particle spray in a large box and a smaller air jet that enters the box tangentially to the surface accumulating particles (Figure 2-7). The box is 30 x 30 x 15 cm and the inflow channel is 4 x 4 x 20 cm, with a uniform 5 mm hex mesh. The spray is positioned opposite the inflow channel with a cone angle of 30 degrees, pointed downward and towards the center of the open box. The injected particle diameters are controlled by a mass-weighted log-normal distribution. The particle spray is active for 1 second, after which time it is deactivated, and the surface roughness is 50 μm . These simulation parameters result in a wall shear stress that should result in a majority of the particles resuspending from the wall. There is an upper and lower particle size that is more likely to resuspend with such a simulation. Small particles have proportionally larger adhesion forces using the Wichner model (since the lift force is proportional to r^2 while the adhesion force is proportional to r), while large particles will be less likely to resuspend due to the gravity force on the particle, which is proportional to r^3 .

Results from two resuspension models are shown here; the model by Wichner [Young 2015] (Eqns. 2-1 and 2-2) using the mean, non-fluctuating wall shear stress, and the same model but including turbulent variations in wall shear stress (Eq. 2-9). Under the conditions in these simulations, the variation in wall shear stress is expected to be as high as 50%.

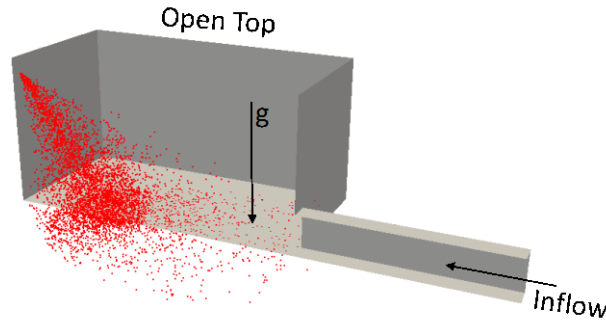


Figure 2-7 Resuspension test domain (cut in half), showing spray location.

After the 1second particle injection is complete, the particles are allowed to settle for 0.5 seconds before the inflow air velocity is increased linearly from 0 to 10 m/s over 1 second, then held constant at 10 m/s for another 1.5 seconds, giving a total simulation time of 4.0 seconds. This results in a maximum friction velocity of around 0.5 m/s through the center of the particle deposition region. To compare the effects of the different resuspension models, we compare the distribution of particles stuck on the bottom surface of the domain (with respect to gravity) at different times, as well as the diameter distribution of the stuck particles before and after the jet (Figure 2-8). The particle deposition patterns at the base surface of this simulation are shown in Figure 2-9. The spatial distribution of particles just before the jet initiation is shown in (a) of this figure.

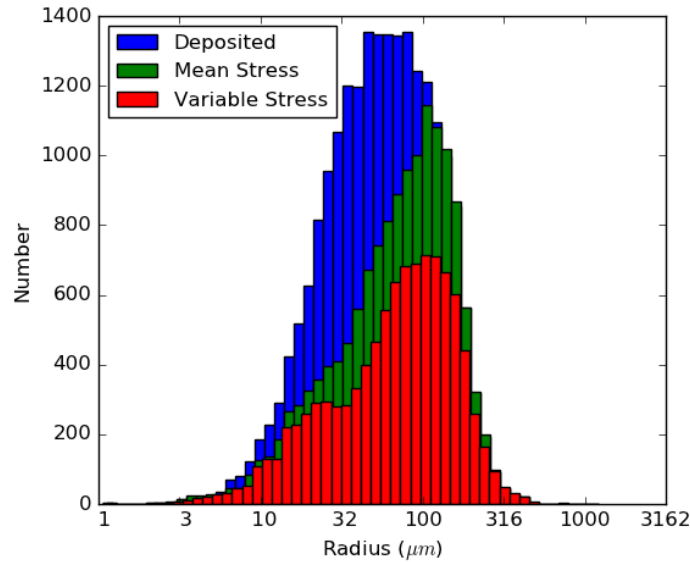


Figure 2-8 Size distribution of particles stuck on base surface at 1.5 seconds (blue) and 4.0 seconds with both the mean (green) and variable (red) shear stress models.

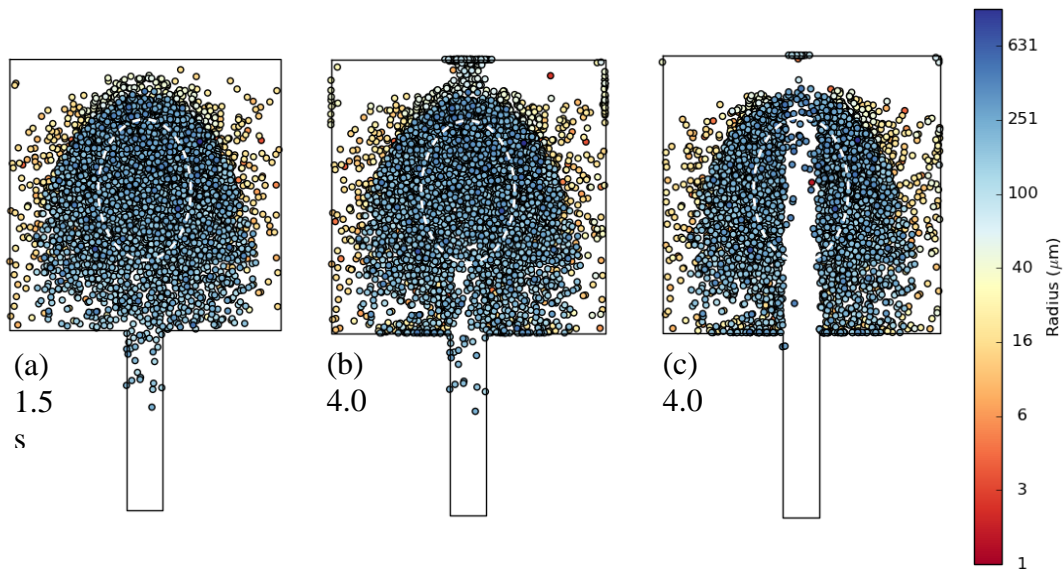


Figure 2-9 Particle deposition pattern on base surface
 (a) just before the jet initiation, with the spray cone intersection ellipse shown by the white dashed line, (b) after being disturbed by the jet using the mean shear stress model, and (c) after being disturbed by the jet using the variable shear stress model.

After the air jet is activated, the particles on the surface are disturbed and some particles are resuspended. Small particles are not resuspended because the adhesion force is greater than the lift force, while large particles are not resuspended because the gravity force is greater than the lift force. For this particular configuration, most of the resuspended particles have radii between 10 and 100 μm . The change in the distribution before and after the jet is shown in Figure 2-8, which illustrates this size dependence.

The spatial distribution of particles at the end of the mean stress simulation is shown in (b) of Figure 2-9. While it is clear that some particles have been removed from the jet path, the larger particles still remain stuck. Near the top of the domain, some of the particles have re-adhered to the surface at the jet stagnation point, where the shear stress is lower. By comparison, the spatial distribution at the simulation end with variable shear stress is shown in (c) of Figure 2-9, where the jet path is almost completely clear of particles.

2.2 Multi-Component Evaporation Model Development

To model multi-component evaporation, such as a contaminated gasoline droplet, the individual constituent components of the droplet must be able to evaporate independently, so that the release of the contaminants can be captured correctly during the evaporation phase. A new multi-component capability has been added to Fuego [Faeth 1983, Law 1982, and Sirignano 1983]. For the purpose of this study, we have enhanced this mechanism to take into account the individual constituent evaporation parameters necessary to evaluate distinct component-level evaporation on a particle mass fraction basis. The new multi-component evaporation model requires additional material parameters for each droplet component such as thermophysical properties of the contaminants and fuel droplets. In this section, we will first describe this new model in terms of the basic evaporation currently in Fuego, and the parameters that influence the evaporation. Then, we will describe the development testing of the newly implemented multi-component evaporation model.

2.2.1 Model Overview

Currently Fuego could be used to simulate evaporating Lagrangian particles within a background fluid. The coupling between the fluid and particle regimes is two-way so that the momentum, energy, and mass source terms are properly exchanged in a loose-coupling approach. That is, the fluid and particle phases are solved separately using source terms provided by the other phase in a staggered approach. The employed evaporation model was consolidated by John Hewson of SNL and is based on theories presented in [Law 1982 and Sirignano 1983]. It has been successfully applied to a variety of scenarios [Brown 2009, Ricks 2011, and Brown et al. 2012]. As mentioned above, Fuego is only able to model evaporation of single component particles. In the new model, we extend the model to allow for particles of an arbitrary number of components. This is particularly useful in scenarios where particles contain spectator or nonvolatile components, which can be present when a contaminant is entrained in liquid droplets. In the following sections, we describe the basic evaporation in Fuego and discuss how we improve the evaporation model by implementation of multi-component capability.

2.2.1.1 Basic Evaporation Model

Fuego supports several varieties of particle dynamics, from simple tracer particles to inertial and heated. Each type couples some properties of the Lagrangian particle to fluid properties. These particle dynamics methods solve a series of ordinary differential equations (ODEs) on the particle variables of interest at each simulation timestep. For the single component evaporation model, these variables are the position (x , y , z), velocity (u , v , w), temperature (T), and mass (M). The right-hand side or source terms calculated are the time derivatives of the variables at the current particle timestep, which can be significantly smaller than the Eulerian (fluid) timescale through the use of user-specified timestep subcycling. This subcycling approach is useful for scenarios like evaporation where the requisite timescale for the particle physics can be significantly smaller than the necessary fluid timestep. For evaporation, the calculation of the temperature and mass terms are coupled through conserved scalar equations. For the new multi-component evaporation model, the mass equation is now replaced with species mass equations, one for each specified droplet component.

2.2.1.2 Evaporation Mechanism Specifics – Position and Velocity

At each particle timestep, a derivative method is called for each particle which determines the time rate of change of each of the relevant particle variables. The first calculation determines the rate of change of the position vector, which is simply the current velocity of the particle.

$$\frac{dx_p}{dt} = v_{p,c} \quad (2-11)$$

Next, the time derivative of the particle velocity is calculated. This, of course, is the particle acceleration, which is the ratio of the net force on the particle to its mass. The force on the particle is the sum of a fluid drag term and a buoyancy force. The drag force is calculated as:

$$f_{\text{Drag}} = -Cf_D v_{\text{rel}} \quad (2-12)$$

Where v_{rel} , the particle relative velocity, C is the drag coefficient, and f_D is the drag correction factor. The particle relative velocity is given as:

$$v_{\text{rel}} = v_p - (v_F + v_{F,f}) \quad (2-13)$$

Where v_p is the particle velocity, v_F is the fluid velocity, and $v_{F,f}$ is the fluctuating fluid velocity, which is determined by the turbulence model used.

The Drag correction pre-factor in Eq.(2-12) is defined as a function of the Reynolds number of the particle, Re_p as:

$$f_D = \left(1 + \frac{Re_p^{\frac{1}{3}}}{6}\right) \text{ for } Re_p < 1000 \quad (2-14)$$

$$f_D = \frac{0.424}{24} Re_p \text{ for } Re_p \geq 1000 \quad (2-15)$$

The Drag coefficient in Eq.(2-12) is defined as:

$$C = 6\pi\mu_F r_p \quad (2-16)$$

where ρ_p , r_p , μ_F are the particle density, particle radius, and fluid viscosity, respectively.

The buoyancy force is calculated as:

$$f_{\text{Buoy}} = -\Delta Mg \quad (2-17)$$

Where g is the gravity, and ΔM is the particle/fluid mass difference, which is defined as:

$$\Delta M = M_p - \frac{4}{3}\pi\rho_F r_p^3 \quad (2-18)$$

where M_p is the particle mass.

The time derivative of the particle velocity is then simply:

$$\frac{dv}{dt} = \frac{f_{\text{Drag}} + f_{\text{Buoy}}}{M_p} \quad (2-19)$$

In the next section, the temperature and species masses from a multi-component droplet are calculated.

2.2.1.3 Evaporation Mechanism – Temperature and Mass

For this purpose, a temperature corrected effective fluid velocity is calculated as:

$$\mu = \mu_F C_\mu \quad (2-20)$$

where

$$C_\mu = \left(\frac{T_\infty + T_p + T_x}{3T_\infty} \right)^{0.7} : T_x = T_{\text{Flame}} \text{ (if specified), } T_x = T_p \text{ (if not)} \quad (2-21)$$

with T_∞ the far field (or fluid) temperature, T_p the particle temperature, and T_{flame} the flame temperature for the evaporating material, if specified by the user. The particle's Reynolds, Nusselt, and Sherwood numbers are determined in the following equations [Ranz 1952]:

$$\text{Re}_p = \frac{2\rho_F r_p v_{\text{rel}}}{\mu_F} \quad (2-22)$$

$$\text{Nu}_p = 1.0 + 0.3\text{Pr}_p^{1/3} \sqrt{\text{Re}_p} \quad (2-23)$$

$$\text{Sh}_p = 1.0 + 0.3\text{Sc}_p^{1/3} \sqrt{\text{Re}_p} \quad (2-24)$$

Where Pr_p and Sc_p are respectively the user specified particle Prandtl and Schmidt numbers.

The evaporation algorithm iterates over all particle species for which an evaporation mechanism has been specified. For each species the heat of vaporization at the current particle temperature is calculated. The heat (enthalpy) of vaporization follows the form:

$$h_{\text{vap}} = h_{\text{vap,ref}} \left(\frac{T_{\text{crit}} - T_p}{T_{\text{crit}} - T_{\text{vap,ref}}} \right)^{0.38} \text{ for } T_p < T_{\text{crit}} , h_{\text{vap,ref}} \text{ 0 for } T_p \geq T_{\text{crit}} \quad (2-25)$$

The vaporization enthalpy $h_{\text{vap,ref}}$ of each species is temperature dependent and falls to zero at the critical point temperature T_{crit} (if one is specified). If no T_{crit} is supplied, the vaporization

enthalpy is set to the reference value for all particle temperatures. The above equation is an empirical relationship between the vaporization enthalpy at the particle temperature and that at the reference vapor temperature as discussed by Lefebvre [Lefebvre 88].

Next the mass and heat transfer numbers (B_{FO} and B_{TO}) are calculated.

The mass transfer number (B_{FO}) is then the ratio of the difference between the mass fraction of the evaporating species at the film surface (Y_{Ff}) and in the fluid ($Y_{F,\infty}$) and the difference between the mass fraction of the species in the particle ($Y_{F,p}$) and at the film.

$$B_{FO} = \frac{Y_{Ff} - Y_{F,\infty}}{Y_{F,p} - Y_{Ff}} \quad (\text{if } Y_{Ff} \approx Y_{F,p}, \text{ we set } Y_{Ff} = (1-\varepsilon) Y_{F,p}, \varepsilon = 10^{-8}) \quad (2-26)$$

Next, the heat transfer number (B_{TO}) is calculated as:

$$B_{TO} = (1 + B_{FO})^{f_{B_{TO}}} - 1 \quad (2-27)$$

Where

$$f_{B_{TO}} = \frac{Pr_p Sh_p}{Sc_p Nu_p} \quad (2-28)$$

The relevant pressure for these calculations is the gas reference pressure, P . The Clausius-Clapeyron relationship is used to determine the mass fraction of the evaporating species at the film surface or Y_{Ff} . This is determined through the partial pressure of the evaporating material in the film:

$$P_{Ff} = P_{\text{vap,ref}} \exp \left[h_{\text{vap}} \frac{MW_f}{R} \left(\frac{1}{T_{\text{vap,ref}}} - \frac{1}{T_p} \right) \right] \quad (2-29)$$

Where MW_f is the molecular weight of the evaporating species (such as fuel), $P_{\text{vap,ref}}$ is the reference vapor pressure supplied by the user, R is the ideal gas constant. This allows us to find the mole fraction of the evaporating species at the film surface:

$$X_{Ff} = \frac{P_{Ff}}{P} \quad (2-30)$$

From the molecular weights of the evaporating species and the average molecular weight of the fluid (MW_G), we can find the average molecular weight of non-fuel species as:

$$MW_{NF} = MW_G \frac{1 - Y_{F,\infty}}{1 - Y_{F,\infty} \frac{MW_G}{MW_F}} \quad (2-31)$$

where the mass fraction of the gas form of the evaporating species in the fluid phase at the particle position ($Y_{F,\infty}$) is found from the local fluid phase data. Then the mass fraction of the evaporating species in the film is simply:

$$Y_{Ff} = \frac{X_{Ff}MW_f}{X_{Ff}MW_f + (1 - X_{Ff})MW_{NF}} \quad (2-32)$$

The time derivative of the current species mass is found through:

$$\frac{dM_F}{dt} = 4\pi r_p \mu \frac{Sh_p}{Sc_p} \log(1 + B_{FO}) Y_{F,p} \quad (2-33)$$

If a thermal radiation transport model is specified, the radiant flux to or from the particle is then calculated as thermal radiation heat (Q_{rad}). The enthalpy of the gas phase at the gas temperature (H_{T_∞}) and at the particle temperatures (H_{T_p}) are calculated. An effective enthalpy difference is determined as:

$$H_s = H_{T_\infty} - H_{T_p} \quad (2-34)$$

For this evaporating species, we then calculate the ratio of the time derivative of the species mass to the heat transfer coefficient calculated above, taking into account the limiting case of a heat transfer coefficient close to zero:

$$R_{mdot,BTO} = \frac{dM_F}{dt} \frac{1}{B_{TO}} \text{ if } (B_{TO} > \text{tol}), = 4\pi r_p \mu \frac{Nu_p}{Pr_p} Y_{F,p} \text{ if } (B_{TO} < \text{tol}) \quad (2-35)$$

Normally the tolerance (tol) is set to 1.0×10^{-12} .

We can then calculate the time derivative of the temperature (associated with this particle species) as:

$$\frac{dT_p}{dt} = \frac{1}{M_p C_p} \left(-\frac{dM_F}{dt} h_{vap} - Q_{rad} + R_{mdot,BTO} H_s \right) Y_{F,p} \quad (2-36)$$

where C_p is the particle specific heat. There is a contribution to dT_p/dt for each particle constituent material. A predictor corrector scheme using LSODE [Radhakrishnan 1993] solver is used for all ODE integrations. Once convergence is achieved on the above set of equations for the current time step, the particle field variables are updated with the converged values. Source terms for the fluid phase are simultaneously calculated and are transferred to the fluid at each Eulerian time step.

2.2.1.4 Example Evaporation Scenario

In the example input file section below, we demonstrate an evaporating particle mechanism within Fuego. In this case, multi-component particles are introduced into the simulation through a particle insertion file. This method allows for the specification on a particle-by-particle basis of the position, velocity, diameter, temperature, parceling (each computational particle represents a parcel of numbers of particles of identical makeup), and time of insertion through a separate user input file (indicated as particles.dat here). A single particle interface is allowed for the evaporating particle dynamics in Fuego. At this scope the user specifies a particle Prandtl and Schmidt number as well as a flame transport temperature (if desired) as described in the evaporation model section above. The particle interface can contain multiple particle

evaporation mechanisms depending on the number of particle species. Two evaporations are defined here, one for each of the particle materials whose properties are also specified. For each evaporation species, both an evaporating particle and gas species are defined with an indicated stoichiometric coefficient; -1.0 indicates that a one molar quantity of the particle material would evaporate to become one mole of the specified gas species. A reference temperature, pressure, heat of vaporization, and critical temperature are also defined, which are used as indicated in the model description above.

Example Particle Evaporation Input Section:

```
BEGIN PARTICLE INTERFACE evapInterface

PRANDTL_NUMBER = 0.9
SCHMIDT_NUMBER = 0.9
FLAME_TEMPERATURE_FOR_TRANSPORT = 2500.0

BEGIN PARTICLE EVAPORATION evaporation1

PARTICLE SPECIES material1 -1.0
REFERENCE_HEAT_OF_VAPORIZATION = 22.694e6 #erg/g
REFERENCE_TEMPERATURE = 373.0
CRITICAL_TEMPERATURE = 647.0
REFERENCE_PRESSURE = 1.0 # in atm
GAS SPECIES H2O 1.0
END PARTICLE EVAPORATION evaporation1
BEGIN PARTICLE EVAPORATION evaporation2

PARTICLE SPECIES material2 -1.0
REFERENCE_HEAT_OF_VAPORIZATION = 22.694e9 #erg/g
REFERENCE_TEMPERATURE = 3730.0
CRITICAL_TEMPERATURE = 6470.0
REFERENCE_PRESSURE = 1.0 # in atm
GAS SPECIES H2O 1.0
END PARTICLE EVAPORATION evaporation2

END PARTICLE INTERFACE evapInterface

BEGIN PARTICLE MATERIAL material1
DENSITY = 791.3e-3 # g/cm^3
SPECIFIC_HEAT = 4.184e7 # erg/g-K
ABSORPTIVITY = 0.75 # no units
END PARTICLE MATERIAL material1

BEGIN PARTICLE MATERIAL material2
DENSITY = 791.3e-2 # g/cm^3
SPECIFIC_HEAT = 4.184e7 # erg/g-K
```

```

    ABSORPTIVITY = 0.75 # no units
END PARTICLE MATERIAL material2

BEGIN PARTICLE DEFINITION multi_particles
    PARTICLE TYPE IS EVAPORATING_PARTICLE
    ADD PARTICLE MATERIAL material1
    ADD PARTICLE MATERIAL material2
    ADD PARTICLE INTERFACE evapInterface
END PARTICLE DEFINITION multi_particles

BEGIN CREATE PARTICLES FROM FILE myFileBlock
    PARTICLE DEFINITION = multi_particles
    FILENAME = particles.dat
    mass_fraction material1 = 0.5
    mass_fraction material2 = 0.5
    LENGTH_SCALE_FACTOR = 1.0

END CREATE PARTICLES FROM FILE myFileBlock

```

2.2.2 Model Testing

Below, we demonstrate the multi-component evaporation model's use in a simple scenario based on the example input deck provided in the previous section. 9 particles of size ranging from 0.3 mm to 2.7 mm in 0.3 mm increments, each at an initial temperature of $T_{p,i} = 300\text{K}$ are introduced at $t = 0$ and with zero velocity into a 100cm^3 box with top and side heated walls at 500K and open lower boundary at 350K (Figure 2-10). The box is initialized with O_2 at 0.233 mass fraction and N_2 at 0.767; no other gas species are initially present. The open lower boundary condition has a mass fraction constraint consistent with this specification. The fluid temperature is initialized to 500K throughout the domain.

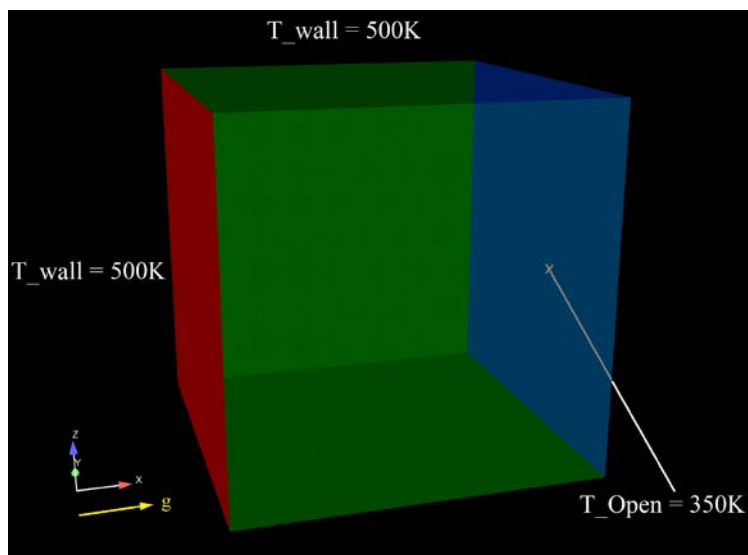


Figure 2-10 Evaporation test domain.

Simulation Domain for Evaporation Example 1. For ease of visualization, the gravity vector is pointed to the right. The upper (left) and side boundary conditions are walls are set to $T = 500\text{K}$, and the lower boundary condition (right) is open with $T = 350\text{K}$.

Buoyancy (gravity) and drag forces affect the particles, forcing them to fall through the domain. As the particles fall through the domain and receive a flux of thermal energy through exchange with the surrounding fluid, the more volatile component, material1, evaporates to produce the gas species H_2O . The less volatile component, material2, (note the enhanced reference and critical temperature) remains mostly un-volatilized so that at late times, a core of nonvolatile material2 remains in the particle.

We note several features. First, as we would expect, small particles fall more slowly than larger particles, consistent with the dependence of the drag and buoyancy forces on the particle size. Second, the smallest particles evaporate off their volatile component quickly, and the mass fraction of the nonvolatile component rises faster for small particles. This can be predicted by the above relationship between the species evaporation rate and the particle size. Combining:

$$\frac{dM_F}{dt} = 4\pi r_p \mu \frac{Sh_p}{Sc_p} \log(1 + B_{FO}) Y_{F,p} \quad (2-37)$$

and:

$$Y_F = \frac{M_F}{M_F + M_{NF}} \quad (2-38)$$

where M_F and M_{NF} are the mass of the evaporating (fuel) and non-evaporating particle components, respectively, we get:

$$\frac{dM_F}{dt} = \frac{4}{3}\pi\rho r_p^3 \frac{dY_F}{dt} \quad (2-39)$$

$$\frac{dY_F}{dt} \sim \frac{1}{r_p^2} \quad (2-40)$$

This indicates that the initial rate of change of the mass fraction of the evaporating species Y_F is higher for small particles (assuming initial mass fractions of particles are the same), just as we observe here.

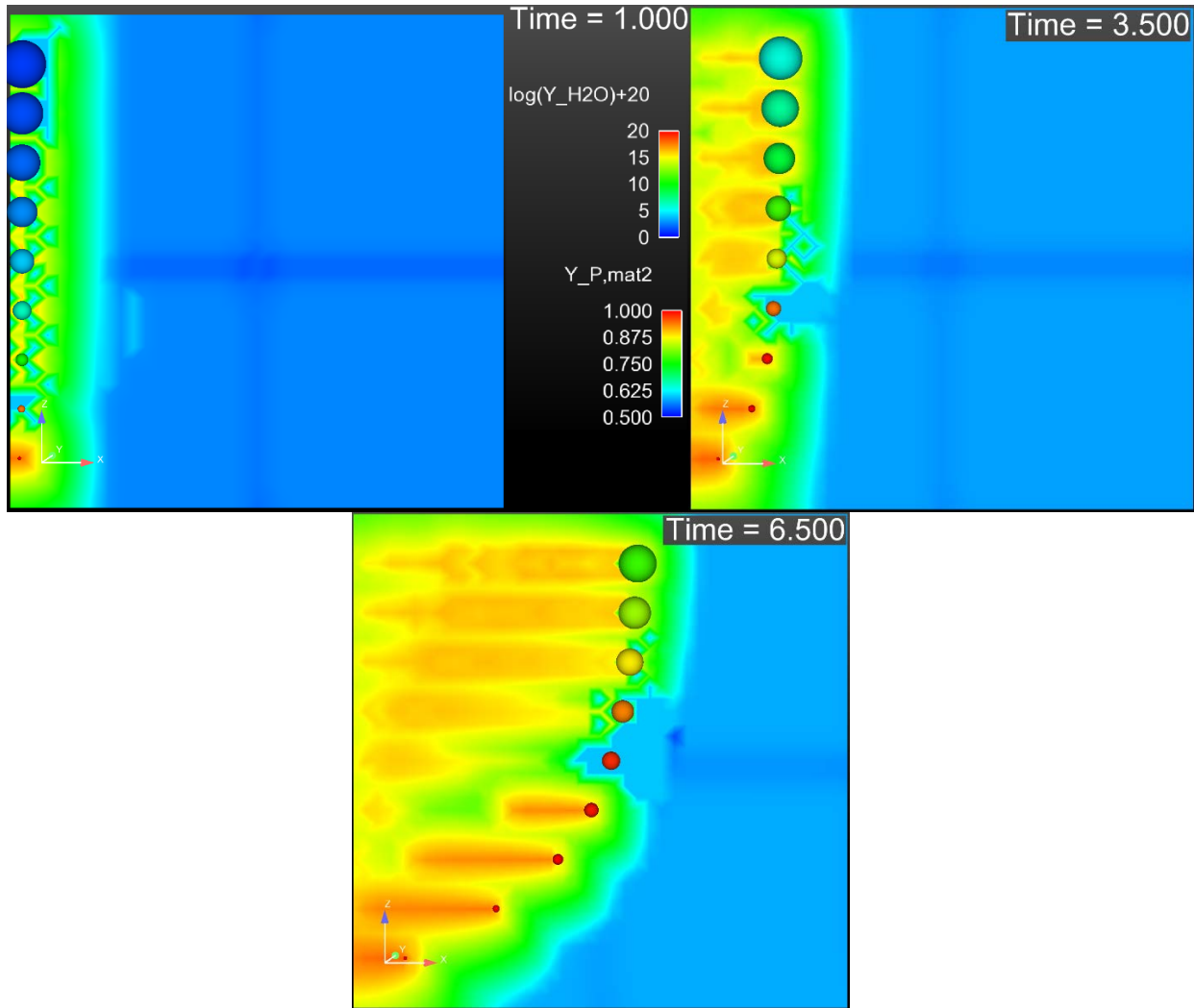


Figure 2-11 Time dependent evaporation of 2 component particles of various sizes (0.3mm – 2.7mm) at 3 different times (t = 1, 3.5, 6.5 sec).

The background fluid region is colored by a logarithmic function of the mass fraction of the volatile species (Y_{H_2O}) to simplify visualization of the evaporation. Particles (exaggerated in size) are colored by the mass fraction of the inert species ($Y_{P,mat2}$) which increases toward 1.0 as the volatile species (mat1) evaporates.

As material1 volatilizes, it produces H_2O in the fluid phase of the domain. This can be seen as a trail of H_2O in the cut plane shown in Figure 2-11. As shown in this figure, particle sizes are exaggerated for clarity. The gravity vector points to the right (+x direction). Particle radii vary from 0.3 mm to 2.7 mm. All particles start with equal mass fractions (0.5) of material1 (volatile) and material2 (volatile2) as discussed in the example input deck section. Particles are colored by the mass fraction of material2 (ranging from 0.5 to 1.0). As particles fall through the domain, material1 evaporates off, and the relative mass fraction of material2 increases. The clip plane shown is colored by the logarithmic mass fraction of the evaporating species (H_2O) which can be seen trailing from the evaporating particles as they fall through the domain.

2.2.2.1 Example Evaporation Scenario 2

The second evaporation example demonstrates the use of the multi-component evaporating particle mechanism within a scenario involving a boiling fuel surface within a cylindrical chamber. This scenario replicates a case from the Handbook. The geometry for this case is shown in Figure 2-12. As shown in this figure, Surfaces are labeled S1-S6. S1 is a fuel ($C_{12}H_{23}$) inflow boundary condition (BC) at a boiling temperature of 473K, and is also the position of evaporating multi-component particle insertion into the domain. S2 is an open (outflow) surface with a specified temperature of 293K and gas species mass fractions specified as $Y(O_2) = 0.233$ and $Y(N_2) = 0.767$. S3 through S5 are wall boundaries at an environment temperature of 293K. S6 is an air inflow boundary condition at a temperature of 293K and mass fractions specified as $Y(O_2) = 0.233$ and $Y(N_2) = 0.767$.

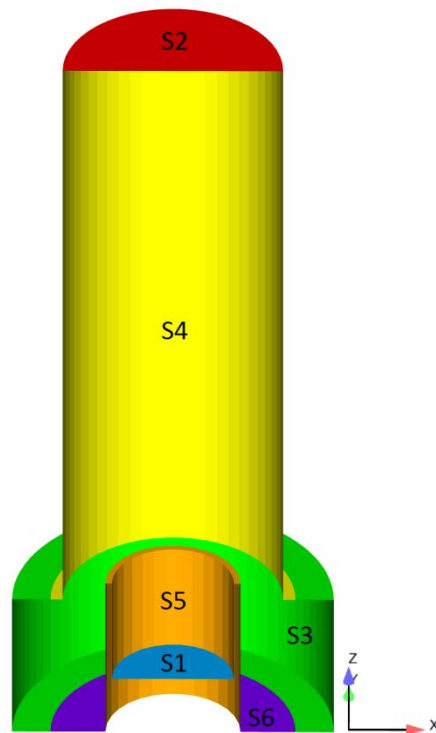


Figure 2-12 Geometry for Evaporation Example 2.

Particles representing multicomponent droplets composed of $C_{12}H_{23}$ (fuel), tributyl phosphate (TBP), and UO_2 are emitted from the boiling fuel inflow surface (S1 in Figure 2-12). As in the previous evaporation case, these particles are introduced into the simulation through a particle insertion file. Over the course of this 6.0s simulation, 12000 particle parcels, each representing a large number of physical droplets, are inserted into the simulation domain. Droplets range in diameter (d_p) from $1\mu m$ to $300\mu m$. Particle size distributions for this scenario are discussed by Brown [Brown 2015]. All introduced particles have relative mass fractions of 0.6($C_{12}H_{23}$): 0.3(TBP): 0.1(UO_2). After an initialization period of 0.2s, ignition occurs, and the gas phase fuel begins to burn, as seen in Figure 2-13. As shown in this figure, particle sizes are exaggerated for clarity and scaled as $r^{1/2}$. The lower fuel surface is colored by the particle mass deposition density (ρ). The upper escape surface is colored by the deposition density of the inert

component (UO_2). Particles are colored by the mass fraction of UO_2 ($Y_p(\text{UO}_2)$). The cut plane through the simulation domain is colored by the temperature of the fluid (T). All particles start with equal mass fractions (0.5) of material1 (volatile) and material2 (volatile2) as discussed in the example input deck section. Particles are colored by the mass fraction of material2 (ranging from 0.5 to 1.0). As particles fall through the domain, material1 evaporates off, and the relative mass fraction of material2 increases. The clip plane shown is colored by the mass fraction of the evaporating species (H_2O) which can be seen trailing from the evaporating particles as they fall through the domain. The burning gas phase fuel heats the fluid, resulting in the evaporation of volatiles $\text{C}_{12}\text{H}_{23}$ and TBP from the particles. This causes the particles to both decrease in size and experience an increase in the mass fraction of the inert component (UO_2), some becoming almost completely UO_2 as the volatile components vaporize. We observe this effect at various times during the simulation in this figure, where some evaporating particles transition from relatively large unevaporated mostly-fuel (blue) to small mostly-inert (white) following vaporization of nearly all of the volatile components. Not all particles fully evaporate to this extent. Many of them fall back to the fuel inflow surface and are reabsorbed as we see on the lower fuel surface (S1) in this figure, which is colored by the absorbed mass density from the particles. Just following ignition, the highly evaporated particles (white) are lofted and some escape the upper open boundary condition (S2) as we see in Figure 2-13 at a time of 0.35 sec. Though this can occur at later times, it is far less likely, in part due to the fact that fully evaporated inert core particles are at a significantly higher density than mostly-fuel droplets and are thus likely to fall back to the fuel surface. The upper boundary (S2) is colored by the mass density of UO_2 (inert) that has been lofted through the upper boundary. The majority of this escape occurs just following the initial ignition event. At late times, both the inflow fuel from the boundary condition at S1 and that from the evaporating particles combusts, contributing to the steady flame whose temperature profile we see in the cut plane at each time frame in Figure 2-13. Previous to this work, our ability to accurately predict the fate of the inert contaminant (UO_2) entrained in the initial mostly-fuel droplets was challenged by our lack of adequate multicomponent evaporation models. This work has enabled us to enhance our physical description of this and similar problems to provide a credible determination of the fate of non-volatile contaminants in entrainment scenarios.

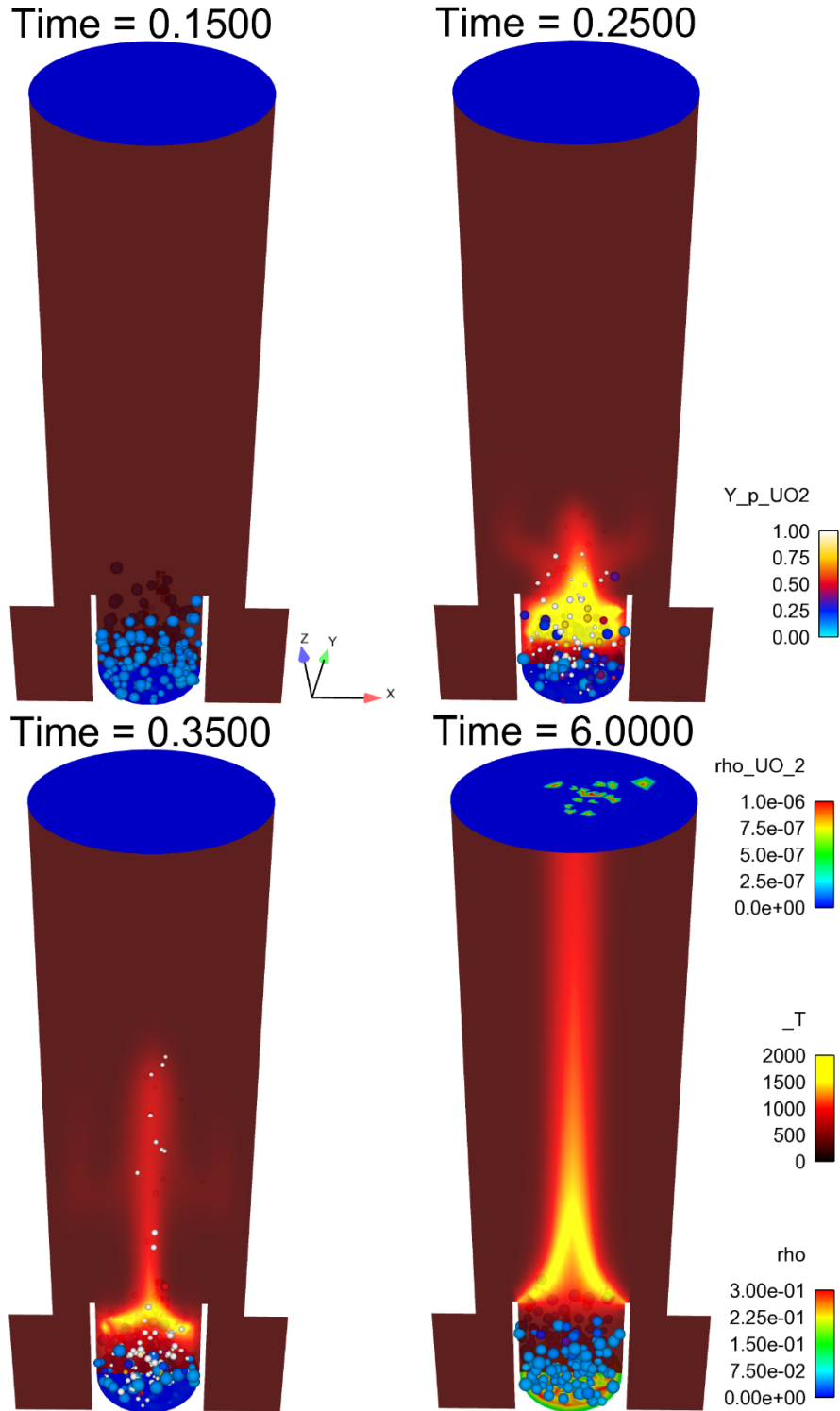


Figure 2-13 Time dependent evaporation of particles of different sizes.
 4 time snapshots ($t = 0.15, 0.25, 0.35, 6.0$ sec) for 2nd evaporation example. Particles colored by the mass fraction of UO₂ (Y_{p_UO2}), cross section through the domain colored by temperature (T), lower fuel surface colored by the mass deposition density (ρ) and upper escape surface colored by the mass deposition density of UO₂ (ρ_{UO_2}).

2.3 Summary and Conclusion

This chapter describes the enhancement to Fuego to allow particle resuspension from deposited surfaces, and to allow better characterization of multi-component effects on evaporations. In the resuspension model, we attempt to characterize the model by using a number of parameters that can be input to Fuego, allowing the modeling of various flow and particle conditions. We have provided development test problems, which demonstrate the usefulness of the model. However, this model may be only suitable for a certain range of particle and flow velocities.

Regarding the multi-component evaporation model, we have provided the basic evaporation model theory, and demonstrated the simplified approach to model multi-components of an evaporating droplet. We also provided development example inputs for testing this model. The latter one describes the beaker fire experiment which will be described in detail in Chapter 4 of this report. The resuspension model will be used in Chapter 3 for analyzing an experiment from the Handbook.

In conclusion, we have provided the code improvement to Fuego to allow us to model the particle resuspension and multi-component evaporation of liquid droplets. Fuego improvement will continue, as the code applications demand additional models. In particular, the deposition (or sticking) of particles with low Stokes numbers (small diameters of particles) in the turbulent boundary layer can be improved. The deposition process is dependent on the boundary layer, fluid velocity, particle size and flow direction. In addition, the particle agglomeration is an important process. Work has begun to implement a particle attractive force model.

3 RESUSPENSION MODEL TESTING AND APPLICATION

This chapter provides documentation for the testing of the particle resuspension model provided in Section 2.1 of this report. In particular, this chapter suggests a way to substantiate the Handbook data by examining the particle resuspension capability in the SIERRA/Fuego code relating to the improvements described in Chapter 2. In this chapter, we first describe resuspension data in the Handbook and the difficulties associated with building confidence by comparing the model to these data. We also attempt to model a reactor experiment for measuring resuspension of particles in a high velocity fluid flow inside a pipe. This reactor experiment is a part of the international standard problem test series, called STORM –SR11 [NEA 1999]. We have developed a Fuego model to simulate the STORM experiment; however, we did not have success modeling the scenario in part due to the fast velocity found in the pipe during the tests. Concurrently, we initiated a separate effort investigating the same experiment using the MELCOR code as reported in another NSRD project [Louie 2016]. Because of the difficulties relating to the test velocity, we did not proceed further to examine the STORM experiment in Fuego.

During an accidental release of radioactive aerosol inside a facility, aerosol particles will deposit on the floor, ceiling, and walls. These deposits are not permanently fixed to the surfaces and therefore pose a potential hazard if disturbed and resuspended. At the time the Handbook was written, the resuspension phenomenon was not well understood. This deficiency was well recognized because, as stated in the Handbook (pages 5-28, 29),

- “Both theoretical and experimental studies of the suspension of solid particles from solid surfaces are still in an elementary state.”
- “Due to an incomplete understanding of the turbulent boundary layer, and more precisely of the bursting phenomenon, uncertainty exists as to the removal forces acting on particles.”
- “The wide range of values for adhesive forces and the lack of models to explain the influence of roughness (both substrate and particle surface) results in great uncertainty.”

Since the writing of the Handbook, considerable progress has been made in terms of understanding resuspension [e.g., Ziskind 2006; Henry 2014]. As given in these review papers, resuspension has been studied for idealized flat surfaces and for some rough surfaces, more characteristic of what would be expected in nuclear facilities. Furthermore, there have been tremendous computational advances in the past 30 years such that we can now model complex facilities using detailed, high-fidelity fluid and aerosol dynamics.

Currently, the Handbook relies on sparse experimental data to obtain reasonable or conservative estimates of ARF and RF of resuspended aerosol. We propose using computational modeling to obtain accident-specific ARFs and RFs. This would be more realistic and not rely on extrapolation and scale-up of small-scale experiments. However, before transitioning to computational modeling, one needs to first demonstrate that the modeling can reproduce results similar to those obtained experimentally. This would provide confidence that the modeling is at least as good as the current Handbook approach. Basically, the computational modeling must first be validated to establish confidence in our approach.

For validating the resuspension model, we used the incompressible Fuego code that can readily model millions of Lagrangian aerosol particles that are tracked individually. The particles are able to move along the flow field, and can become stuck onto walls. If particles do not stick, they can reflect or bounce off the boundary. In addition, under the appropriate conditions, stuck particles can become resuspended. For the validation data, we used the best characterized experiments reported in the Handbook for resuspension. We found the work of Fish et al., [Fish 1967] to be appropriate. At the time of the experiment, real-time aerosol measurements were not widely available or practical, so only time-integrated values were reported. Despite this issue, the critical measurement is the resuspension factor. According to the Handbook, page 4-88, “Resuspension factors are defined as the ratio between the airborne concentration of a pollutant per cubic meter directly over a contaminated surface and the areal pollutant surface contamination.” We therefore compared the resuspension factor determined by experiment with the computational results.

3.1 Fish Experiment Description

At the time of the Fish experiment, real-time aerosol measurements were not widely available or practical, so only time-integrated values were reported. Nonetheless, the critical measurement is the resuspension factor. According to the Handbook, page 4-88, “Resuspension factors are defined as the ratio between the airborne concentration of a pollutant per cubic meter directly over a contaminated surface and the areal pollutant surface contamination.” We therefore compared the resuspension factor determined by experiment with the computational results.

The experiment occurred in an 8’x8’x12’ room. ZnS particles were dispersed into the room and the air was physically agitated until the particles were homogeneously distributed throughout the volume [Fish et al., 1967]. Figure 3-1 shows the schematic of a human walking in a room for modeling resuspension of particulates. The particles were then allowed to gravitationally settle onto the floor for 48 hours. Thereafter, a set of experiments was performed in an attempt to suspend the particles off the floor and into the air based on various degrees of human activity. We simulated the experiment with the most human activity, which involved vigorous walking and sweeping. This lasted for ten minutes, at which point measurements were taken. The resuspension factor was measured as $1.9 \times 10^{-6} \text{ cm}^{-1}$. Some of the key parameters used in the simulation were ZnS particle diameter, particle density, and the areal particle concentration, which were $3.1 \text{ }\mu\text{m}$, 4.1 grams/cm^3 , and $2.44 \times 10^{-6} \text{ particles/cm}^2$, respectively. We note that for this experiment, the walking and sweeping speeds were not recorded.

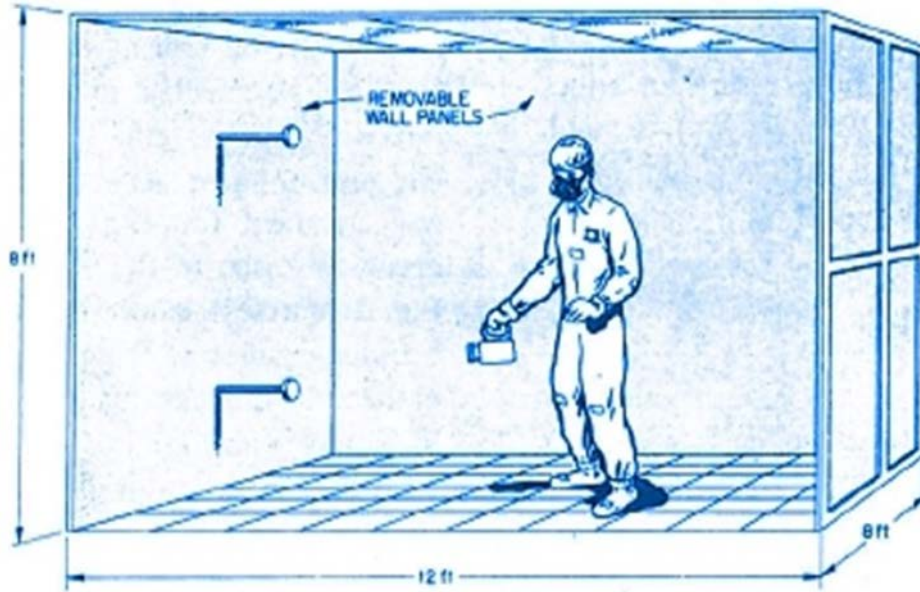


Figure 3-1 Schematic of the Human Activity Experiment [Fish 1967].

3.1.1 Fuego Aerosol Model

We generated various meshes that are compliant with NRC guidelines and CFD journal recommendations, with meshes containing 100,000 to 4,000,000 hexahedral elements [Sierra, 2016; Zigh and Solis, 2013; Fluent, 2012; Rodriguez, 2013; Rodriguez, 2014]. The geometry involved a three-dimensional (3-D) rectangular room, and our meshes used uniformly sized hexagonal elements. The element length was generated such that it was sufficiently small to capture the integral and Taylor eddy turbulent physics, while still providing answers in a reasonable amount of time. The dynamic Smagorinsky large eddy simulation (LES) turbulence model was selected to capture the large energy-containing eddies that had the greatest influence on the particle's motion. Furthermore, the sweeping and walking motion generated lots of swirl, especially as the fluid motion reached the walls. The LES model is suitable for low to intermediate swirl [Wilcox, 2006].

The mesh boundaries were broken up into side sets (i.e., boundary conditions (BCs)). The ceiling and the four lateral walls consisted of zero-velocity wall BCs. In turn, each of the four lateral walls had a small BC that enabled us to estimate the amount of particle suspension on the walking man. Due to budget constraints, our approach consisted of estimating the number of particles that become suspended and then trapped onto a small section of the lateral walls, and then those results were extrapolated based on the man's surface area.

The floor was then divided into 24 BCs of equal surface area, in an attempt to mimic the person as he walked and swept through the room. Each of these BCs was given a time-dependent velocity distribution, that is, an x-y-z velocity component. Each BC activated as the man walked and swept through the room, and deactivated as he proceeded in his motion.

100,000 particles were tracked and were placed on the floor at the start of the simulation. The ceiling and walls were given a stick boundary condition for the particles. This means that if any

given particle contacted any of the stick boundaries directly, it attached to the wall through the remainder of the simulation. Each of the 24 floor BCs allowed particle resuspension based on the Wichner resuspension model [Young, 2015].

3.1.2 Fuego Results and Discussions

The floor was swept through once, which corresponds to 24 seconds of vigorous human activity. Figure 3-2 and Figure 3-3 show the particle spatial distribution at 40 seconds and 115 seconds, respectively. The particles were allowed to resettle for an additional 576 seconds. The first particle stuck within 1.5 seconds of the simulation. At the end of the 600 seconds, a resuspension factor was calculated from the simulation based on the number of stuck particles on the small, lateral wall BCs, and prorated to the man's frontal surface area. This resulted in a resuspension factor of $9.5 \times 10^{-6} \text{ cm}^{-1}$ compared to the actual experimental measurement of $1.9 \times 10^{-6} \text{ cm}^{-1}$. This is shown in Figure 3-4. We noted that the resuspension factor had a strong dependence on the velocity vector magnitude of the walking-sweeping side sets.

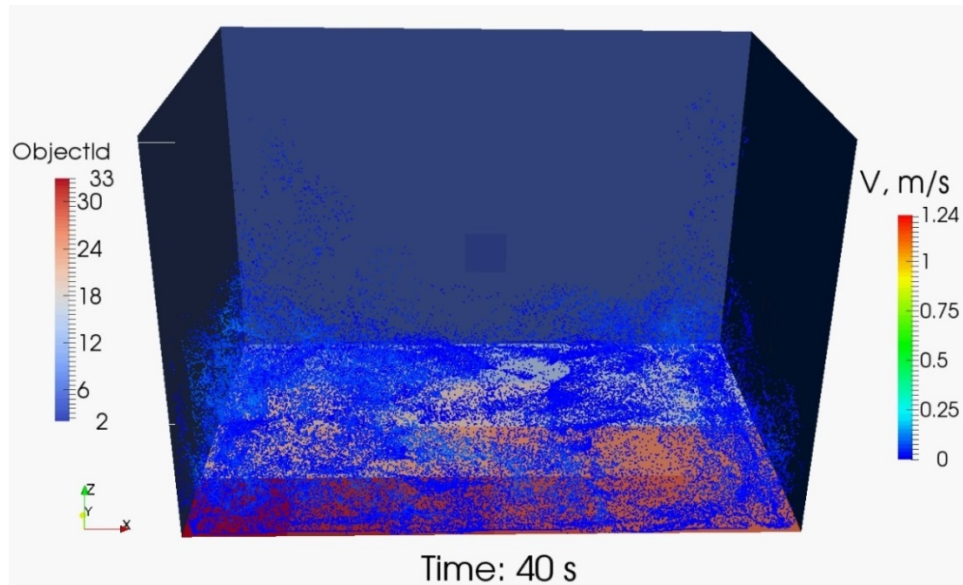


Figure 3-2 ZnS Particle Spatial Distribution at 40 seconds.

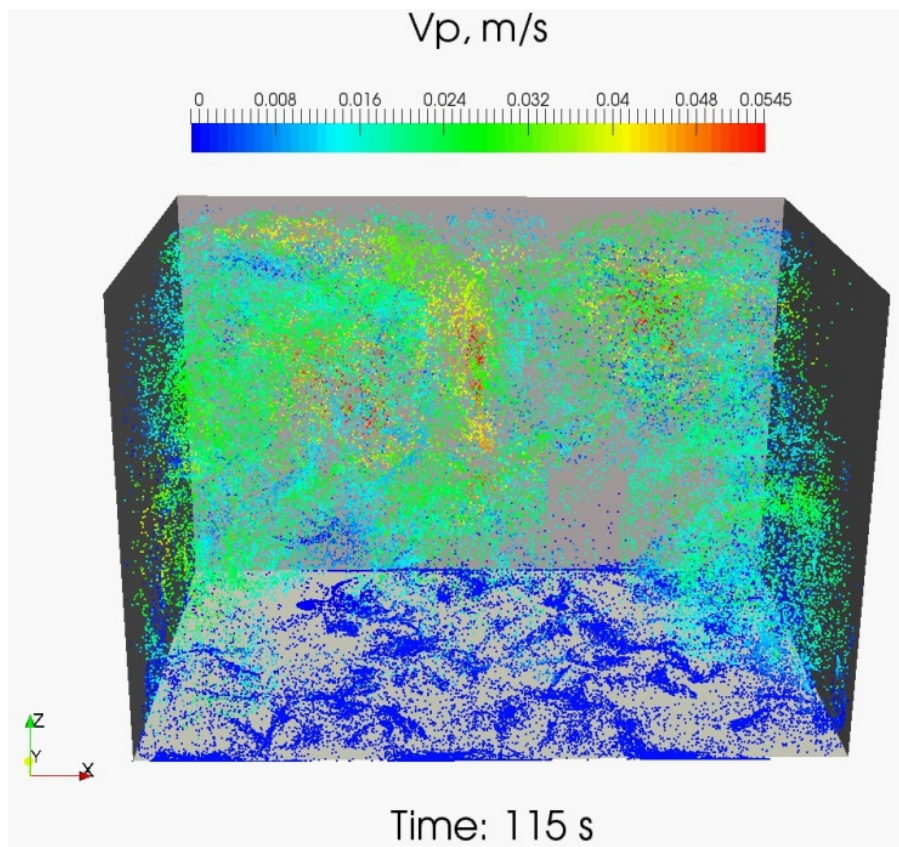


Figure 3-3 ZnS Particle Spatial Distribution at 115 seconds.

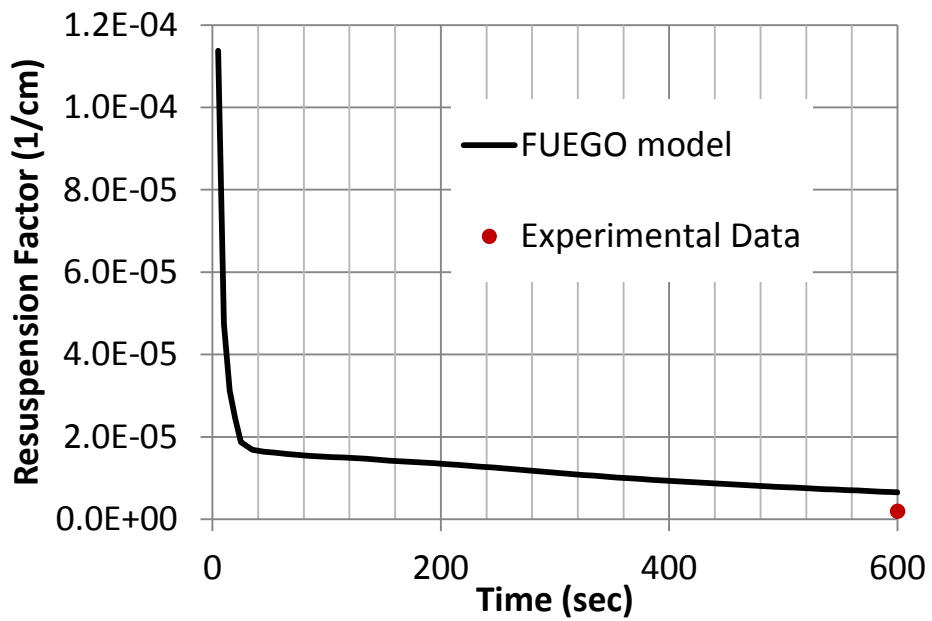


Figure 3-4 Comparison of computed and measured resuspension factor.

3.2 Summary and Conclusion

Chapter 3 attempts to test the resuspension model described in Chapter 2 by using the resuspension data in the Handbook. We were able to model the human activity in a room that results in resuspension of particles.

The Handbook uses data generated about 50 years ago to estimate a resuspension factor. This is only a single number to provide a time and spatially integrated value for the fraction of aerosol particles that would be resuspended above a contaminated surface for a range of activities. The experiments were not well characterized by today's standards since measurement equipment and diagnostics were limited. Nonetheless, the resuspension factor is used and provides a basis for assessing computational modeling of the resuspension process.

By using our existing flow modeling software and state-of-the-art computer hardware, we demonstrated that it is possible to simulate a resuspension experiment. The simulations have tremendous fidelity in terms of where and when aerosol particles would be resuspended for accidents of interest. In this work, we compared the computed resuspension factor to the measured value for particles of known size and physical properties that were deposited on a floor. The computations were within an order of magnitude of the measured resuspension factor. This is desirable considering that the conditions of the experiments were not provided in detail.

The ability to model a human walking in a simulation is a challenging task, particularly when the experiment description is not clear and specific enough. However, in addition to the above conclusions, we can use the Fuego code to simulate human activity in environments with aerosol concentrations.

4 REANALYZING FIRE EXPERIMENTS

Chapter 4 re-analyzes the fire experiments that were reported in Year 1 [Louie 2015]. The improvement in the particle models described in Chapter 2 of this report should provide a better substantiation of the Handbook data. In Chapter 2, both the particle resuspension model and a multi-component evaporation model have been implemented in Fuego. It is important to use the multi-component evaporation model to analyze the beaker fire experiment (see Section 4.1 below) because the evaporation model used in Year 1 was a single component only. With a multi-component evaporation model, both contaminant and fuel can be modeled as a single component. With the multi-component evaporation model, the contaminant and fuel can be modeled as a separate component. For the gasoline pool fire experiment (see Section 4.2), the resuspension model should provide insight about the resuspension after the fire is gone by capturing particle resuspension from the residues remained in the pan.

4.1 Beaker Fire Simulations

Section 4.1 re-analyzes the beaker fire simulations from Year 1. However, the improvement of the multi-component evaporation model as described in Chapter 2 should provide a better estimate of the ARF than the reported value from Year 1.

4.1.1 Introduction

Brown and Louie [Brown 2015a] described the various mechanisms of droplet formation and contaminant entrainment. We will only summarize that discussion here. Fuel droplets with entrained contaminants are presumed to result from the rupture of bubbles at the boiling surface of the fuel/air interface. A review of these mechanisms can be found in Kogan and Schmacher [Kogan 2008] and Bagul [Bagul 2013]. Droplet formation can basically be described as being either in the film breakup regime, where droplets result from collapse of the bubble dome or the jet regime where droplets are created from pinching of liquid tendrils following bubble collapse. The first regime produces droplets mostly in the 1-100 μm range, the second in the 100-300 μm range [Borkowski 1986]. A third droplet formation mechanism exists where droplets are produced by air flow over the surface of the liquid fuel through stretching and collapse of surface waves. A final mechanism can be present when the fuel has burnt almost completely off and the burning fuel surface and residual layer of contaminant are coincident (or nearly so) or when material previously deposited on a surface evaporates to evolve droplets back into the fluid region.

[Louie 2015 and Brown 2015a] utilized the entrainment model of Kataoka and Ishii [Kataoka 1983], described from the Handbook [DOE 1994]. To summarize, the Kataoka and Ishii model calculates an entrainment factor which is the ratio of the evolved droplet mass flux to the evolved gas phase mass flux and depends only on the ratio of the liquid fuel (ρ_f) to gas (ρ_g) density:

$$E_{fg} = 4.84 \times 10^{-3} \left(\frac{\rho_f}{\rho_g} - 1 \right) \quad (4-1)$$

Brown and Louie [Brown 2015] discussed the possibility of entrainment of contaminants from the residual layer following the burn off of most of the liquid fuel when the fuel burn surface

nearly coincides with the residual layer, as well as possible entrainment of contaminant from surfaces where deposition had previously occurred as described by Henry and Minier [Henry 2014], but these models were not used, in part due to the complexity of describing all of the relevant governing factors.

In this work we focus on improving on the previous efforts by Brown and Louie [Brown 2015a] investigating contaminant entrainment at a boiling liquid fuel surface through the introduction of more detailed Lagrangian particle physics into the CFD code that was used, the Sierra low Mach module Fuego [Domino 2003]. We hope to improve on the predicative nature of our simulations through these enhanced physics models. Whereas the previous paper used heated inertial particles as surrogates for evaporating multi-component droplets, coupled to the background fluid through drag (momentum) and heat (energy), we have implemented and utilized a model for multi-component evaporation that allows independent evaporation of the distinct volatile droplet components and conversely no volatilization for inert components. Volatilized particle species provide mass and enthalpic transfer to the surrounding gas phase as well as the momentum and heat transfer seen in the inertial particles previously used. As in the previous work, the experimental scenario that is simulated comes from the 1973 experiments of Mishima and Schwendiman (MS) [Mishima 1973a], a primary data set of the Handbook [DOE 1994], which we will subsequently refer to as the MS or beaker-fire scenario.

4.1.2 Methods and Simulation Details

The entrainment model of Kataoka and Ishii [Kataoka 1983] has been used in this study as in the previous work, consistent with the model referenced by the Handbook. As in the Handbook, Borkowski's 1986 [Borkowski 1986] data set on droplet sizes has been used here as well to inform the size distribution of droplets used in our simulations. The resulting bimodal distribution as a probability density function (PDF) is reproduced from Brown and Louie [Brown 2015] in Figure 4-1.

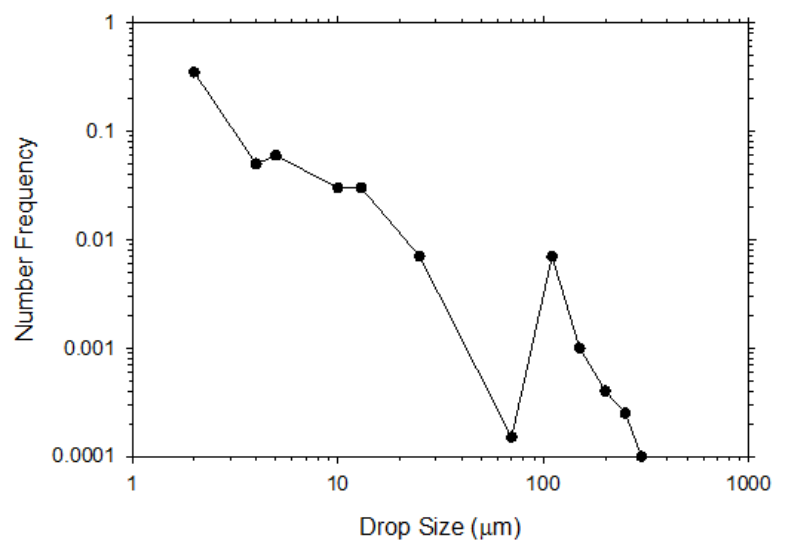


Figure 4-1 Borkowski's number vs. droplet size PDF. [Borkowski 1986]

MS's [Mishima 1973] beaker-fire experiments started with kerosene and 30% TBP contaminated by other materials. Similarly, in the current study, all droplets are initialized as 60% fuel (kerosene), 30% TBP [Nazar'ko 1981], and 10% contaminant by mass. Contaminant properties are modeled as UO_2 [IAEA 1965, Popov 2000]. Material properties for these components are specified in the references above or are readily available. In this scenario, both fuel and TBP are modeled as volatile. Additional parameters such as the heat of vaporization and critical point temperature were required to populate the models sufficiently. Other than the specification of multiple components within the droplets, the same particle data set generated for use in the previous study was used here.

As in the earlier study, the surface of the fuel was pre-heated to the boiling point. The fuel was placed in a 50mL beaker, filling 25mL of the volume, and ignited. The beaker had a 56 mm height and outer diameter of 42 mm.

4.1.2.1 Evaporation Mechanism Specifics – Particle Integration

See Evaporation Model description in Chapter 2 of this report.

4.1.2.2 Additional Simulation Details

In the previous study, the insertion of droplets over the surface was uniform. Simulations were performed over time frames near the beginning and end of the fuel burn (at the start and near fuel burn-out), in part due to computational constraints and in part because Fuego lacks the ability to model fuel surface recession. The fuel surface started about 20mm from the bottom of the beaker and ended with 4-9mL of residue accumulated at the bottom of the beaker. Droplets were inserted with upward velocities of between 0 and 1 m/s. Turbulence at the inlet is modeled as minimal. At the start of the simulation, the beaker is full of air ($\text{YO}_2 = 0.267$, $\text{YN}_2 = 0.733$) at ambient temperature and pressure. The fuel surface burning was modeled to produce a constant mass flux of 7×10^{-6} kg/sec.

SIERRA low-Mach module Fuego [Domino 2003] is developed at SNL under the Advanced Simulation and Computing (ASC) program and is designed to work on high performance computing clusters of thousands to tens of thousands of cores with ongoing work to enable it to work at scales of hundreds of thousands to millions of cores. Fuego is an incompressible (low Mach number) CFD code that allows a range of physics including reacting flows, two-way Lagrangian particle coupling, and sophisticated turbulence models.

Particle parceling is used in Fuego to allow one particle entity to represent N particles of equal size and constituency that transport and evolve as a single entity. This is particularly useful in scenarios where millions or even billions of real physical droplets are present in a system, and computational limitations prevent solving this number of independent sets of ODEs for each and every particle. Parceling is akin to particle binning to represent a PDF. When parceling is used, source terms between the particle and fluid phases are scaled accordingly. Care must be used when parceling is employed so that one does not lose too much information in the tails of the distribution which may represent possible but lower probability outcomes.

When particles collide with a surface, they are removed from the simulation domain, and their mass and individual species masses accumulate on the impacted surface element. This allows

for the calculation of total mass and species mass across surfaces of interest including the pool surface, beaker side walls, and upper escape surface. Gas phase reactions are modeled with the eddy dissipation concept (EDC) model of [Magnussen 1981].

Table 4-1 below displays the full matrix of simulation parameters varied in this study which is consistent with those from the original computational study [Brown 2015a]. Pool height, particle insertion file, and turbulence parameters were varied in these studies. The baseline cases are labeled Base (1-5). These cases differ by specific particle insertion data. Variations on turbulence parameters at the pool surface are labeled TurbMod7(A-D) and TurbMod8(A-D). Late time scenarios, where the pool surface has receded to near the bottom of the beaker are labeled as Late Base (1-6), again with variation on the particle insertion data. One additional variation was made, using a pool with initial height of 40mm, indicated as Early Base (1-6), again varying particle insertion data.

Table 4-1 The simulation matrix showing all parameters varied in the simulations, including duration, particle data file used, turbulence parameters at the pool surface, and pool height.

<i>Simulation</i>	<i>duration (sec)</i>	<i>particle file</i>	<i>turbulent KE</i>	<i>turbulent dissipation</i>	<i>pool height(mm)</i>
EARLY					
Early Base 1	160	short1a_1.txt	1.1130E-06	1.1230E-06	40
Early Base 2	160	short1a_2.txt	1.1130E-06	1.1230E-06	40
Early Base 3	160	short1a_3.txt	1.1130E-06	1.1230E-06	40
Early Base 4	160	short1a_4.txt	1.1130E-06	1.1230E-06	40
Early Base 5	160	short1a_5.txt	1.1130E-06	1.1230E-06	40
Early Base 6	160	short1a_6.txt	1.1130E-06	1.1230E-06	40
MID					
Base 1	6	start6s1.txt	1.1130E-06	1.1230E-06	20
Base 2	6	start6s2.txt	1.1130E-06	1.1230E-06	20
Base 3	6	start6s3.txt	1.1130E-06	1.1230E-06	20
Base 4	6	start6s4.txt	1.1130E-06	1.1230E-06	20
Base 5	6	start6s5.txt	1.1130E-06	1.1230E-06	20
TurbMod7A	60	short_input.txt	5.9480E-05	1.5300E-04	20
TurbMod7B	60	short_input.txt	5.9480E-05	1.9200E-06	20
TurbMod7C	60	short_input.txt	5.9480E-03	1.5300E-01	20
TurbMod7D	60	short_input.txt	5.9480E-03	1.9200E-03	20
TurbMod8A	60	short_input1.txt	5.9480E-05	1.5300E-04	20
TurbMod8B	60	short_input1.txt	5.9480E-05	1.9200E-06	20
TurbMod8C	60	short_input1.txt	5.9480E-03	1.5300E-01	20
TurbMod8D	60	short_input1.txt	5.9480E-03	1.9200E-03	20
LATE					
Late Base 1	200	end_200s1.txt	1.1130E-06	1.1230E-06	0
Late Base 2	200	end_200s2.txt	1.1130E-06	1.1230E-06	0
Late Base 3	200	end_200s3.txt	1.1130E-06	1.1230E-06	0
Late Base 4	200	end_200s4.txt	1.1130E-06	1.1230E-06	0
Late Base 5	200	end_200s5.txt	1.1130E-06	1.1230E-06	0
Late Base 6	200	end_200s6.txt	1.1130E-06	1.1230E-06	0

4.1.3 Results and Discussions

Figure 4-2 shows a cross section of the Fuego simulation domain for one of the simulations with droplets present at 0.1 seconds, just before ignition begins at 0.2 seconds; ignition occurs at the same time for each scenario. The bounding surfaces (pool, beaker side walls, surface escape) are colored by the deposition number density which is the number of particles per area that have fallen on that section of each surface. Here, at the beginning of the simulation, the surfaces are almost completely free of any deposition. The droplets are exaggerated in size for clarity and are

colored by the mass fraction of the contaminant species (UO_2). Before ignition, the particle mass fractions are nearly the same as at initiation, as seen in these droplets near the lower fuel surface (contaminant 10%). Each simulated scenario has a similar appearance at this point. Particle parcels are exaggerated in size and colored according to their mass fraction of the contaminant $Y(\text{UO}_2)$, at these early times nearly unchanged from the initial value of 10%. Near the start of the simulation, as here, the deposition density is close to zero.

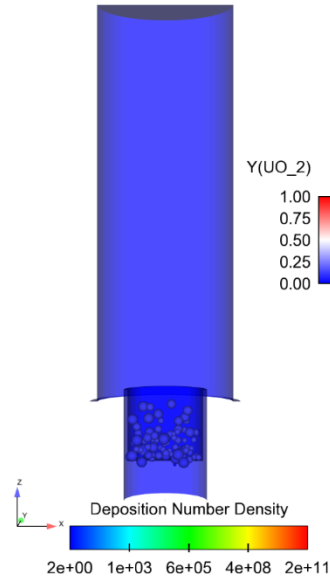


Figure 4-2 Illustration of the predicted liquid droplet entrainment from one of the MS tests (Base 1) at 0.1 seconds, before ignition at 0.2 seconds.

Figure 4-3 displays the fluid phase flame temperature and droplets/deposition surfaces for one of the scenarios in the test matrix as simulated in Fuego at 0.3 seconds, just following ignition at 0.2 seconds. As shown in this figure, the frame on the left displays the fluid temperature on an axially aligned cross section through the simulation domain. The right frame displays the same data as in the Figure 4-2. A number of highly evaporated droplets (mostly contaminant) remain following volatilization of the fuel species, with others near the fuel surface at intermediate stages. No deposition on the top and side walls is observed. The presence of lofted, highly evaporated, mostly contaminant particles is obvious. There are also particles in various stages of evaporation near the burning fuel surface. Deposition on the side walls has already begun. The ignition phase of the fire leads to significant lofting of the particles, resulting in escape of the contaminant through the upper surface. As the fire progresses, the escape rate decreases. At later times we observe increased surface deposition on the various bounding surfaces, as seen in Figure 4-4. As shown in this figure, the left and right frames display the same data as in Figure 4-3. Significant deposition has occurred by this point on the beaker side walls as well as at the top surface (colored by number deposited). At late times, smaller particles can still escape. Larger particles likely end up returning to the fuel surface from which they originated due to increased gravitational forces vs. lofting forces.

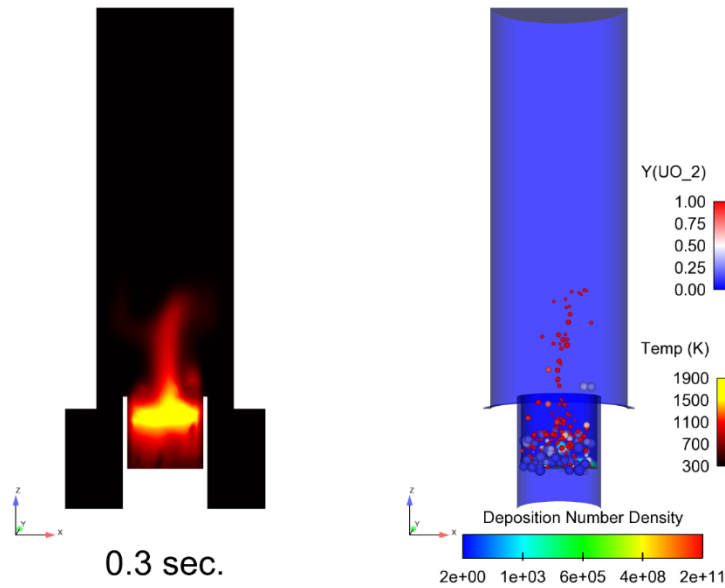


Figure 4-3 An illustration of the predicted liquid droplet entrainment from one of the MS test scenarios (Base 1) at 0.3 s, following ignition at 0.2 s.

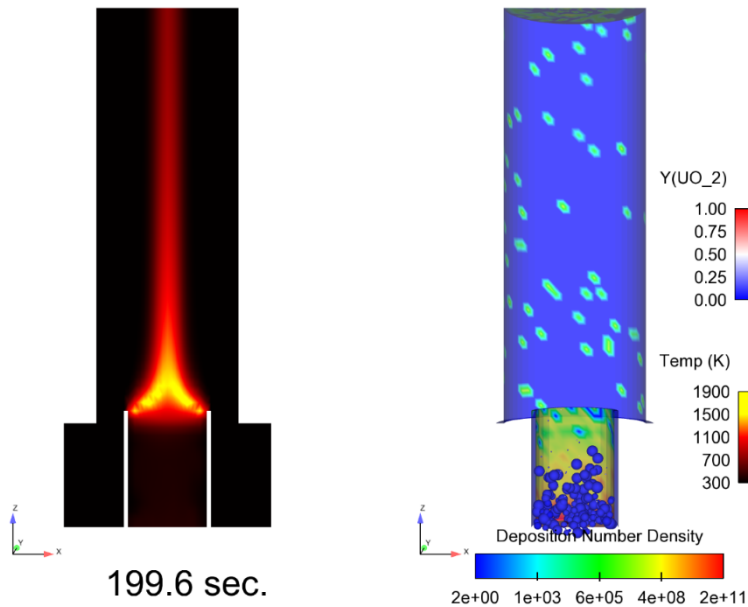


Figure 4-4 An illustration of the predicted liquid droplet entrainment from one of the MS test scenarios (Late Base 1) late in the simulation.

Unlike the previous work, we are now able to track the deposition of the contaminant mass separately from the other particle materials. This allows us to make a determination of the fate of the contaminant directly vs. indirectly through the total mass deposited. There is some distinction here, however. Since we are no longer dealing with simpler, non-evaporating inertial particles, the full mass of the droplets that enters the system is not accounted for by the sum of the mass deposited on the surfaces. Some of the particles included as parts of the volatile components enter the fluid phase through evaporation. The evaporated fuel can subsequently

burn. Since the contaminant is inert, tracking the deposition of the contaminant does give us a part of the information we need in determining the fraction of contaminant that is lost to the environment through the upper escape surface, the ARF. However, this calculation is complicated by several factors. First, a large fraction of the particles which are introduced above the fuel surface return to it and are reabsorbed. These could potentially be reintroduced into the system through subsequent boiling of the fuel. Second, the fuel surface doesn't recede within an individual simulation. Recession of the fuel surface will alter the rate at which contaminant is lost to the escape surface and what is deposited on the beaker side walls as well as what remains in the beaker. Therefore, in order to determine the fraction of the contaminant material that escapes from the surface, we must interpolate the release rates between early and late times, which includes the geometric variation of the pool height.

In Figure 4-5 we display the temporal evolution of contaminant mass that is deposited at the pool surface, beaker sides, and escapes through the upper boundary for an early time scenario (Base 1 from the Table 4-1). As shown in this figure, this flare-up is caused by rapid evaporation of fuel species from the droplets and subsequent combustion. Like the ignition mechanism, this process can lead to transport of contaminant species to the upper escape surface. Note that a significant amount of contaminant mass escapes the upper boundary between 0.5s and 0.9s. This pulse was observed in the previous computational work and is thought to be due to the initial dynamics of the developing flame. Subsequent to this initial pulse, there is only a marginal rate of contaminant escape. Following ignition, the flame steadies and its structure becomes more or less constant. After the initial 1 second, the rate of contaminant deposition on the pool and beaker side surfaces remains nearly constant..

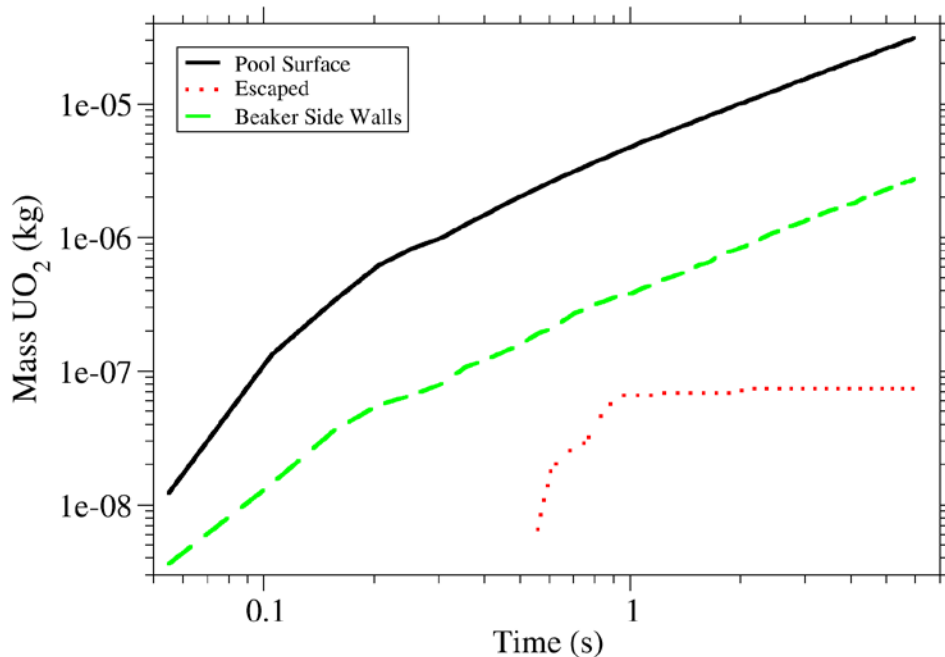


Figure 4-5 Predicted mass of contaminant (UO_2) deposited on pool surface, beaker side walls, and escape surface for the early period of the beaker-fire burn (Base 1).

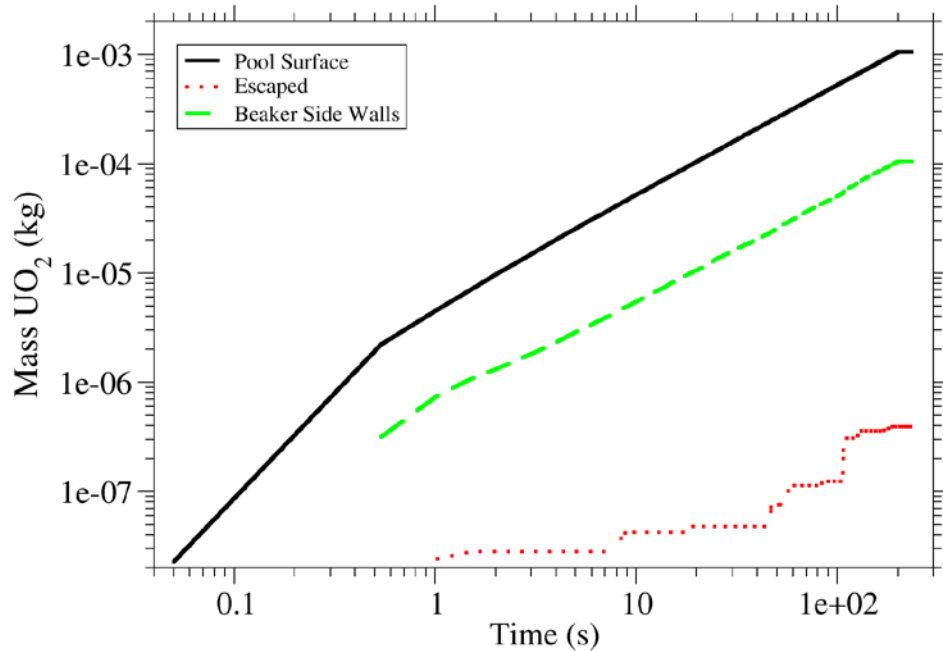


Figure 4-6 Predicted mass of contaminant (UO₂) deposited on pool surface, beaker side walls, and escape surface for the late period of the beaker-fire run (Late Base 1).

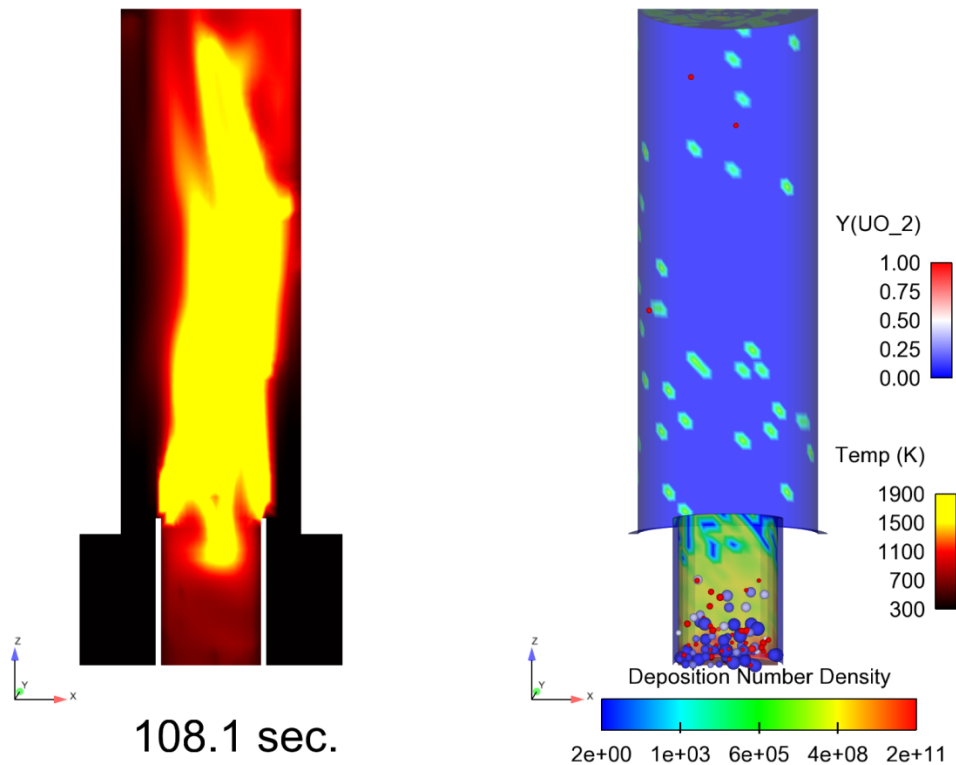


Figure 4-7 A flare-up event seen in one of the MS scenarios at late times in the simulation (Late Base 1).

In Figure 4-6, the deposition vs. time on these surfaces for the later scenario is shown, where the flame surface is near the base of the beaker. Note that the surface and beaker side wall deposition rates are still approximately constant. However, we observe some interesting features in the escape from the upper surface. There are periods of rapid release of contaminant mass. As shown in Figure 4-7, an example of such an event was seen through the flame temperature and particles in the domain. We find similar flare-up events in all of the late time scenarios, though not always as intense. Though intermittent, they can result in a significant flux of contaminant mass to the upper escape surface.

In the earlier study, the later time scenarios resulted in a greater rate of contaminant escape through the upper surface. Our Year 1 report [Louie 2015] postulated that flame motion within the beaker was responsible for lifting the droplets more easily to the escape surface despite the increased pool depth. This effect brought into question how conservative the experimental studies were, as pool height variation was not explored in the experimental effort. As in the previous computational study [Louie 2015], we used the same set of particle input files that have the same mean droplet mass insertion rate and particle size distribution but vary statistically in where and when particles are inserted. We also, as in the Year 1 study, observed variation in the surface contaminant deposition rates due to differences in the particle insertion files. In our case, this is consistent with the flare-up events which are affected by the specific characteristics of particle insertion. Even without flare-ups, we would expect some differences as reported in Year 1.

As in the original study, we find a significant portion of the contaminant mass deposits on the beaker side walls through collision of droplets with the side walls. Though physically one might expect some of this contaminant material to be re-entrained at later times, we have not included this effect in this study. This is an important consideration for future work, and is a direct mechanism suggested by the authors of the experimental study. We have also not included a mechanism for material deposited on the side walls to transport vertically downward toward the pool due to gravitational effects, although the assumed particle source term rate implicitly includes this effect.

Our calculation for ARF is as follows. From the experimental study, the pool initially contained 25mL of fuel with contaminant and self-extinguished after a time period between 42 and 56 minutes when the pool contained between 4mL and 9mL of sludge [Mishima 1973]. This sets an average consumption rate for the pool of between 0.29 mL/min and 0.50 mL/min (4.8×10^{-9} m³/s and 8.3×10^{-9} m³/s). Though the rate may not have been constant, we have no data to indicate the details of the rate of pool consumption, so we assume a constant rate. The radius of the beaker in our scenario is 1.9 cm. This leads to a linear regression rate of the pool of between 4.2×10^{-4} cm/s and 7.4×10^{-4} cm/s. Since our base scenarios and scenarios, Turbmod7 and TurbMod8 used an initial height of 20mm (2cm), and the Late Base Scenarios were at 0mm, this would indicate a total burn time of between 2700s and 4800s (45min and 80min).

The initial pool condition is 10% mass fraction UO₂ in our scenario. The average density of the pool is:

$$\rho = \left(\frac{Y_{\text{UO}_2}}{\rho_{\text{UO}_2}} + \frac{Y_{\text{TBP}}}{\rho_{\text{TBP}}} + \frac{Y_{\text{fuel}}}{\rho_{\text{fuel}}} \right)^{-1} = 8.44 \frac{\text{g}}{\text{cm}^3} \quad (4-2)$$

The volume of the pool is:

$$V = \pi r^2 h = \pi(1.9\text{cm})^2(2\text{cm}) = 22.7\text{cm}^3 \quad (4-3)$$

Thus the total mass of the consumed material is 191 g, which includes the total mass of 19.1g UO₂ (all scenarios identified in Table 4-1, except Early Base). For the Early Base scenarios, the volume of fuel consumed is 45.4 cm³ which at the rates given above would take between 5400s and 9600s to consume. Thus, the original samples for the Early Base scenario would contain a total of 38.2g UO₂, which indicated that half of the UO₂ mass were released.

At the end of the burn, using the Late Base scenarios, the average rate of escape of UO₂ from the upper surface is calculated to be $(1.03 \times 10^{-6} \pm 7.3 \times 10^{-7})\text{g/s}$. For each of the other scenarios, we calculate an initial pulse and the initial rate of UO₂ mass escape. We then calculate an average ARF for each of the base (Base 1-5) and turbulence modified scenarios (TurbMod7A-D, TurbMod8A-D) as well as for the cases with 40mm initial fuel height (Early Base 1-6).

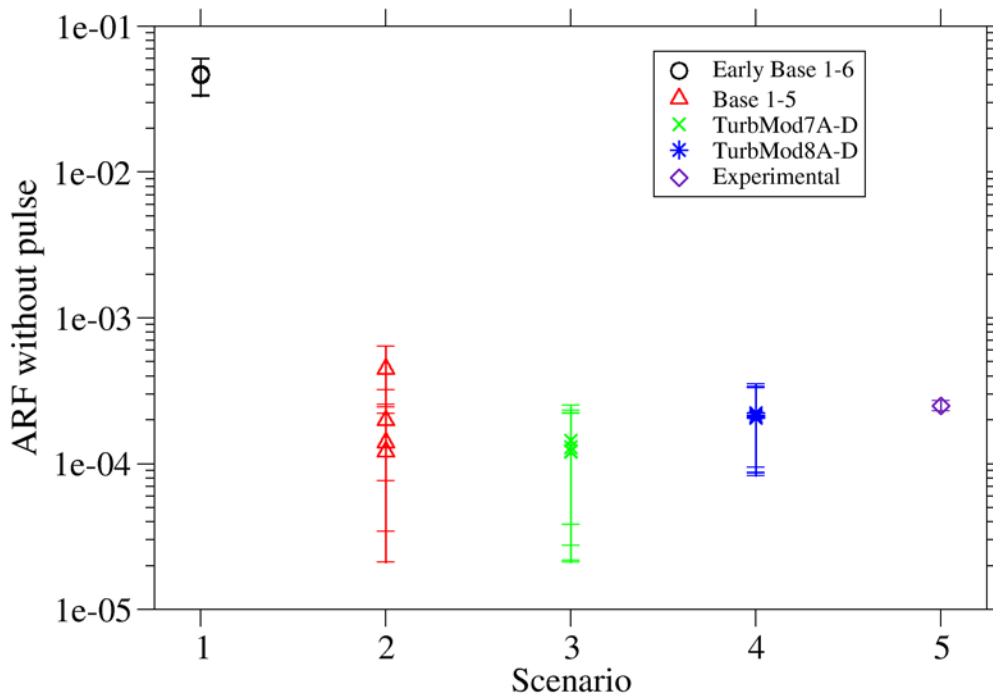


Figure 4-8 ARF for all Scenarios starting at 20 mm (Base 1-5, Turbmod7 A-D, TurbMod8 A-D) or 40mm (Early Base 1-6) pool height without inclusion of the contaminant mass from the initial ignition pulse.

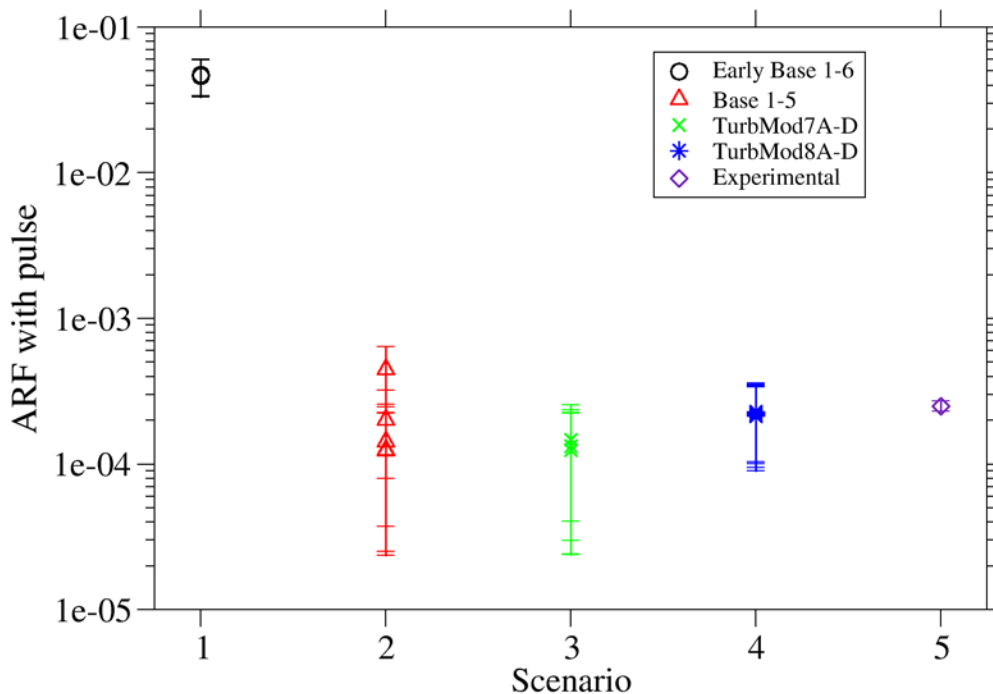


Figure 4-9 ARF for all Scenarios starting at 20 mm (Base 1-5, Turbmod7 A-D, TurbMod8 A-D) or 40mm (Early Base 1-6) pool height with inclusion of the contaminant mass from the initial ignition pulse.

Figure 4-8 and Figure 4-9 display the calculated ARFs for each of the scenarios in our test matrix both without and with inclusion of the initial contaminant mass pulse at the escape surface due to ignition, respectively. Shown in these figures are the first four scenarios as the Fuego simulations in the legend. Scenario 5 is for the experimental data. The error bars are also given based on minimum and maximum times to burnout. Error bars within each simulation are due to uncertainty in the fuel consumption rate as indicated above. The results between inclusion and exclusion of the initial pulse are nearly indistinguishable, indicating that overall the ignition pulse is relatively unimportant. We observe significant variation in the ARF due to particle insertion data within the baseline, though within the error bars there is significant overlap between these variations. We note that TurbMod8 scenarios differ from corresponding TurbMod7 scenarios only through the specifics of the particle insertion data. Thus the variations in turbulence which occur between A-D variations have little effect on contaminant escape in comparison to the specifics of particle insertion. This may be a result of the flare-up events we observed in each of the scenarios, which, like ignition, result in relatively high transport of contaminant to the upper escape surface. The Early Base scenarios (initial pool height 40mm) have little observable variation due to particle insertion file, and have significantly higher ARF. A steady stream of highly evaporated, mostly UO_2 particles transits through the escape surface in these scenarios. Also, the Year 1 report indicated the observation of a larger steady flux of particles through the escape surface due to entrainment in the plume. As shown in Figure 4-9,

ARFs here are mostly indistinguishable from those without inclusion of the ignition pulse. This indicates that the pulse is a relatively minor phenomenon.

4.1.4 General Discussions

Inclusion of a multi-component evaporation model [Brown 2015] resulted in ARF predictions that vary from those seen in the original work for baseline and modified turbulence scenarios. Mishima and Schwendiman [Mishima 1973] report an ARF of $0.025 \pm 0.002\%$ (2.5 ± 0.2) $\times 10^{-4}$ for UO_2 . Our calculations for ARF for baseline cases as well as the turbulence modified scenarios starting at a pool height of 20mm are in good agreement with this data. The higher initial pool height (40mm) resulted in ARF values much higher than the other scenarios, which as we discussed earlier, occurs due to increased ability of the particles to escape the beaker. However, Mishima and Schwendiman [Mishima 1973] did not vary pool height in their experimental study. Unlike the previous study, we have seen that the ignition pulse that was believed to be an artifact of the numerical ignition model, does not play a large role in the total ARF after including the multi-component drop model.

As in the earlier study [Brown 2015] we observe large deposition on the beaker side walls. Re-entrainment from these deposits could play a significant role in the escape of contaminants [Mishima 1973], but this remains a topic for future study and was not investigated here.

We also concur with the original computational study that pool height plays a large role in contaminant release. The Early Base scenarios which started at 40mm pool height had the highest ARF by a significant margin, and the Late Base Scenarios at 0mm pool height showed higher escape rates than the baseline cases at 20mm. Mishima and Schwendiman [Mishima 1973] did not vary the pool height, and this could play a role in evaluating the conservative nature of these results for use in the Handbook.

Our results indicate that contaminant release from a burning fuel with entrained contaminant droplets is not principally due to initial flame dynamics, though that was observed in the original computational study [Brown 2015] with non-evaporating inertial particles. The variation of the particle insertion data played the largest role, with the turbulence model variations near the pool surface exhibiting less importance. The initial pool height had the largest impact on the predicted ARF, and as in the earlier study, it is clear that more experimental results would be helpful in exploring this variation. Since the goal of the DOE handbook is to provide conservative estimates for these scenarios, and greater contaminant release rates were observed both at lower (0mm) and higher (40mm) pool heights than the nominal of 20mm, variation in pool height should be explored further.

4.2 Gasoline Fire Simulation

This section describes the re-analysis of the gasoline fire experiment from Year 1 [Louie 2015]. Here, we apply both the multi-component evaporation model and the resuspension model to re-substantiate this experiment.

4.2.1 Introduction

In addition to the beaker fire simulations, larger scale simulations were done on an experiment focusing on particle entrainment from a gasoline pool fire contained in a wind tunnel [Mishima

1973a, Brown 2015a, Louie 2015]. This experiment is more germane to a potential transportation accident because pool fires generally transition from laminar to turbulent as the diameter increases approximately past one meter [Drysdale 1998]. The SIERRA/Fluid Mechanic code Fuego was used to perform the beaker and gasoline fire simulations for this report [SIERRA 2016d]. Several modified scenarios were also investigated to account for uncertainties from the reported physical experiments and to determine parameter sensitivities.

The previous studies assumed a single, non-volatile component for the particle type, which ignores evaporation phenomena. This scenario is unrealistic as the gasoline in the entrained contaminated particles would evaporate, leaving the smaller, non-volatile contaminant. Therefore, additional physics have since been implemented into the code suite to support the improved modelling capability for these scenarios, prompting reanalysis of both previous simulations. The added capabilities included the ability to specify multiple species components in a single particle and track volatile evaporation and individual species deposition onto boundaries. A model to adhere and subsequently resuspend particles ‘stuck’ on boundaries was also implemented. This paper describes the Fuego simulation comparisons of the gasoline pool fire experiment with the experimental results, as well as the previous simulated results [Brown 2015a]. The goal of this effort is to determine the impact magnitude that the inclusion of multi-species tracking and resuspension has on the previous predicted results.

4.2.2 Theory

4.2.2.1 Entrainment Mechanisms

For pool fire scenarios, four particle entrainment mechanisms shown in Table 4-2 were identified from the literature to be potentially active during fires of this nature. A more detailed description of the meaning and justification for these phenomena is presented in previous work [Brown 2015a].

Table 4-2 Entrainment mechanisms believed to be potentially active in this scenario.

Mechanism	Conditions for Activity	Parametric Functional Sensitivity	References
Evaporation Induced Entrainment (EIE)	Liquid is actively evaporating	Particle size distribution Density Exposed Surface Area Rate of evaporation Vapor pressure of the solvent Evaporating species molecular weight	[Mishima 1968]
Surface Agitation by Wind	Existence of a substantial wind and a liquid surface	Wind Speed Surface Tension Viscosity Density Fire dimensions Fuel layer depth Geometry present	[Derakhti 2014]
Surface Agitation by Boiling	Pool temperature approaches boiling point of liquid	Rate of Boiling Size of bubbles Viscosity Surface Tension Density	[Mishima 1973, Kogan 2008, Bagul 2013, Borkowski 1986, Kataoka 1983]
Residue Entrainment (Resuspension)	Wind, vibration, or other activating factors, and no	Wind Speed Particle sizes	[Roberts 2003, Lick 2009, Sehmel 1984, Henry 2014,

	remaining liquid	Density Viscosity Particle forces	Young 2015]
--	------------------	---	-------------

4.2.2.1.1 Evaporation induced entrainment (EIE)

The fuel pool consists of gasoline that will evaporate at ambient conditions. Evaporation is enhanced by the presence of the fire. Despite the liquid temperatures being well below the evaporation temperature of the contaminant, releases have been observed in prior testing of this nature [Kogan 2008]. The mechanism driving this release is not completely clear. It likely relates to the momentum or energy carried by evaporating gases imparted onto the smallest non-volatile contaminant near the pool surface. This is the source of the name ‘evaporation induced entrainment.’ This mechanism was observed in previous work [Mishima 1968].

4.2.2.1.2 Surface agitation by wind

This mechanism entrains particulates through surface instabilities and wind related disturbances. This process does not require a fire to be active, rather a strong wind flowing across a fuel pool surface can agitate the liquid and create waves. A frothy layer of mixed liquid and gas fuel can form along with pinching of wave tips, both with the possibility to entrain contaminant. A detailed description of this mechanism and contributing components can be found in previously presented work [Derakhti 2014].

4.2.2.1.3 Surface agitation by boiling

This mechanism is studied more extensively. It is particularly active in deep pools near the boiling temperature and shallow pools at near burn-out conditions. It begins with the formation of bubbles in the pool which rise and rupture at the liquid surface. Previous work focused primarily on this mechanism, as the experiment being simulated was designed to highlight this entrainment mechanism [Mishima 1973a, Brown 2015a, Louie 2015]. Work done by Borkowski et al. [Borkowski 1986] provided the basis for the particle size distribution, while the superficial evolution was determined from correlations of Kataoka and Ishii [Kataoka 1983]. The equations used to determine source terms for the below scenario are presented in detail in previous work [Brown 2015b]. This study observed that the model predicted that the boiling mechanism was significantly dominant over the evaporation induced entrainment mechanism. The correlations used are thought to be applicable to problems insofar as the materials are similar to boiling water, which was used to develop the fit parameters.

4.2.2.1.4 Residue entrainment (resuspension)

Resuspension of particles adhering to surfaces may have a significant contribution to the overall ARF. Resuspension occurs as air flows across a particle-laden surface, and the lift force experienced by the individual particles overcomes the adhesion and gravitational forces. The resuspension model is based on work done by Wichner and summarized by Young [Young 2015]. The equations used in the force balance are (2-1) and (2-2) from Chapter 2. The gravitational force acting on the particle is also included in the force balance this model. The validation of the resuspension model is as yet incomplete.

4.2.2.2 Multi-Component Particles

In the experiments, the contaminant was dispersed in the fuel. Assuming the boiling mechanism is dominant, entrained particles will be a combination of both the liquid fuel and the solid contaminant. The solid contaminant is non-volatile as its melting temperature exceeds the temperatures experienced in this system by approximately 800 °C. It is suspended in the evaporating fuel droplet. Due to the fact that the fire was generally well above the boiling temperature of the fuel, the liquid phase fuel in the entrained particles evaporates rapidly, leaving the smaller contaminant particles entrained in the fluid flow. With the multi-component particle model described in previous sections, particles can evaporate volatile components separately. Particle diameters are reduced through fuel evaporation, resulting in just the trace contaminant particles after the fuel fully evaporates. Particles interacting with the boundaries deposit components accounted for separately for individual species deposition analysis.

4.2.3 Methods

Simulations of historical tests are made feasible by combining components of the models described above in the theory section. This section describes the CFD capabilities and parameters used to perform simulations on the gasoline pan fire experiments performed by Mishima and Schwendiman [Mishima 1973a]. New interpretation of the experimental effort is obtained as the simulations provide higher fidelity insight into the various contributing phenomena and their relative importance to the overall solution.

4.2.3.1 Computational Capabilities

Simulations were performed using the SIERRA/FM predictive code suite allowing multi-physics on the parallel computing resources available at SNL. The suite tool Fuego was employed for calculations. Fuego is a low-Mach number code suited for flow, fire and particle dynamics simulations. It solves the Navier-Stokes equation for reacting flows. For the calculations presented here, the TFNS turbulence model [Magnussen 1981] was selected, as was the EDC reaction model [Tieszen 2005]. Particles were simulated with a Lagrangian/Eulerian two-way coupling scheme between the fluid and particles.

4.2.3.2 Experimental Conditions

Simulation parameters were based on sub-tests SA-17a and SA-17b from Mishima and Schwendiman [Mishima 1973b] experiments. In SA-17a, particles were released from a gasoline pool fire contained within a wind tunnel with a flow of less than four miles per hour. Depleted uranium dioxide (UO₂, representing plutonium) was distributed by hand into the 15-inch diameter stainless steel pan, prior to the addition of gasoline. One gallon of gasoline was added via a nozzle directly above the pan, and subsequently ignited. High Efficiency Particulate Air (HEPA) filters collected the entrained contaminants during the nine-minute burn. The filters were removed after burnout and the collected contaminant was analyzed. For experiment SA-17b, the filters were replaced and the flow resumed for 4.7 hours, after which the filters were again removed for analysis.

4.2.3.3 Input Boundary Conditions

From the previous work it was determined that, while present for the majority of the burn, EIE is not a significant contributing entrainment mechanism when compared with the release values predicted from the boiling mechanism. A visual representation of the model prediction during the boiling phase is seen in Figure 4-10. The boiling mechanism is initiated near the end of the

burn as the pool begins to boil. The precise boiling onset time for the experiment simulated here is unknown, as it was not recorded in the physical experiment. Particle source terms are determined from correlations and are based on similar experiments in the literature. Previous Fuego simulations employed a 1-D pool model to represent the evaporation of the gasoline in the steel pan. During the boiling phase, the evaporation of the particles will be a major contributor to the gas fuel source term. The magnitude of this was estimated, and the pool boundary condition was modeled with a fuel source term equal to the steady-state burn rate minus the estimated particle fuel source term. The fire was initiated 3 seconds prior to the addition of particles to reach steady state. Boiling was active until burnout and the simulation continued for an additional five seconds, allowing all particles to exit the domain.

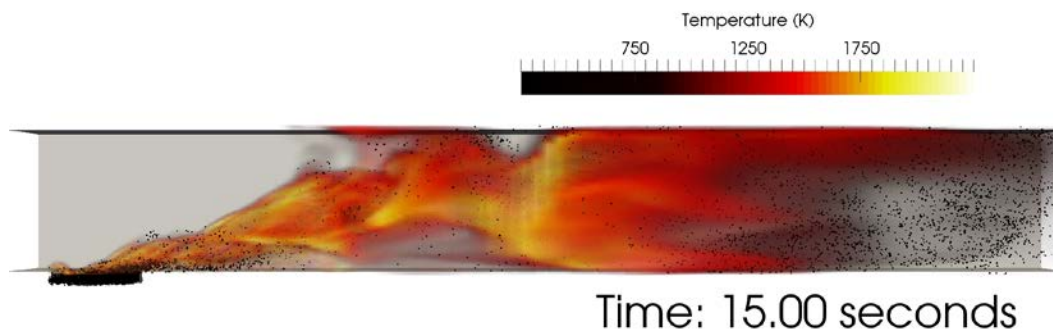


Figure 4-10 Boiling scenario: Contaminant entrainment prediction, parcels enlarged for visualization.

Resuspension of contaminants was of interest in the original physical experiment, and the code suite now has the model framework to predict resuspension. As of this publication, the multiple species particle evaporation and tracking capability were not integrated into the same version of the code as the resuspension model; therefore, the simulation particle parameters were reverted to be identical to those assumed in the previous work. This included using the 1-D pool model. Contaminants were released in a fire and allowed to deposit on boundaries using the new particle deposition model. After burnout, the input air flow remained, and the particles were allowed to resuspend in this flow.

4.2.3.3.1 Computational mesh

A wind tunnel mesh, unchanged from mesh in the previous work, was generated using the experimentally reported dimension, as seen in Figure 4-11. The wind tunnel is modelled at 4.57 m long with a .66 m square cross-section. Surface 1 is the air inflow boundary, with a fixed flow rate and temperature of 1 m/s (2.2 mph, assumed from the test report) and 298 K respectively. Surface 2 represents the stainless steel tunnel walls, modelled with a 1.3 cm conducting wall boundary condition, with a backside temperature set to 298 K. Surface 3 is the outflow boundary condition placed near the experimental filter location, set to collect entrained particles. Surface 4 represents the dirt ring in which the fuel pan is set, modelled as a 1.3 cm thick 1D conducting surface. Surface 5 represents the fuel pan. The circular pan measured 0.381 meters in diameter and is assumed in the model to be filled with pure heptane fuel (C_7H_{16}) as a surrogate for the gasoline used in the physical experiment. Heptane liquid and the gas phase thermodynamic properties represent the more complex gasoline fuel mixture used in the experimental test.

Finally, surface 6 is the exposed lip of the stainless steel pool, modelled as a conducting boundary condition.

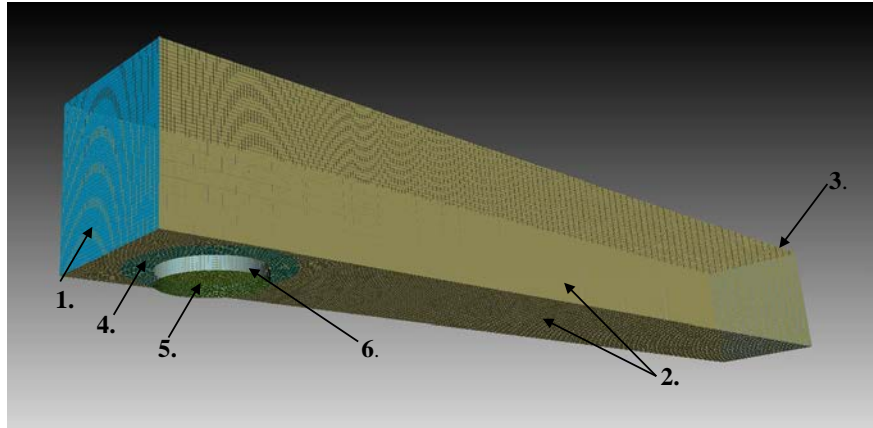


Figure 4-11 Wind tunnel mesh: Geometry and surfaces.

Previous work simulated two different lip heights to account for the “near-full” and “near-empty” fuel height conditions. This work only uses the “near-empty” mesh, as that corresponds best to the boiling and resuspension mechanisms. The lip height was set to 51 mm, and multiple mesh refinements were made to determine mesh convergence. Minor variations between simulations using the above described mesh and simulations involving further refinements indicated that baseline mesh exhibited adequate mesh convergence. It was therefore selected as a baseline. The mesh was relatively uniform with 12.7 mm spacing near the fuel pan, and increased spacing downstream to improve the computational speed. The baseline mesh had 709,856 elements.

To determine the mass deposition on various boundaries, the mass deposition density for each surface is integrated at the end of the simulation. The simulations were run for 5 seconds past the last particle injection time to account for settling of suspended particles. Particles are permitted to deposit on the walls, pool, lip, dirt ring and outflow of the tunnel. Both species (fuel and UO₂ contaminant) are integrated separately.

4.2.3.3.2 Turbulence parameters

Precise turbulent boundary condition parameters could not be gathered from the experimental report and this therefore was treated as a free parameter. It was assumed that a grate would be present to protect against large foreign objects entering the blower, so 10 cm, or 15% of the duct size, was chosen as a length scale. The base inflow and wall turbulence intensity was set to 20%, but, due to the experimental uncertainty, it was increased in one scenario to 100% to study the effect on entrainment. The turbulence was modelled using TFNS, which is a hybrid LES-RANS model [Magnussen 1981]. The turbulence parameters used are listed below in Table 4-3. K is the turbulent kinetic energy and ϵ_{turb} is the turbulent dissipation parameter.

Table 4-3 Turbulent boundary conditions for surfaces and scenarios.

Turbulence Location	K	ϵ_{turb}
Inflow Boundary Surface (1, Figure 4-11)	2.0×10^{-2}	4.64×10^{-3}
Pool Surface (5, Figure 4-11), not Boiling	1.13×10^{-6}	1.12×10^{-6}

Pool Surface, Boiling	3.11×10^{-4}	1.23×10^{-4}
Inflow Boundary, 100% Turbulence Intensity	5.0×10^{-1}	9.7×10^{-1}

4.2.3.3.3 Pool model

The fuel pool was modeled as if fuel vapor is injected with a constant speed normal for the fuel surface, referred to as vapor velocity. Gaseous fuel is injected into the system at the surface of the fuel pan at a constant rate. The injection rate is estimated from the steady-state burn rate minus the amount of fuel located in the particle injections. Prior to the injection of particles at 3 seconds, the vapor flow rate was 1.004 kg/s. The flow rate was reduced to 0.301 kg/s to compensate for the evaporating fuel from the entrained particles. Upon burnout, the rate was reduced to 0.100 kg/s to represent near burnout conditions. The fuel velocities are summarized below in Table 4-4.

Table 4-4 Vapor velocity for pool model at various times (baseline)

Simulation Time (seconds)	Vapor Velocity (kg/s)
0-3	1.004×10^0
3-20	3.011×10^{-1}
20-25	1.004×10^{-1}

4.2.3.3.4 Particle injection method

Particle parcels are introduced to the simulation through an input data file. This file contains parameters for position, initial velocity, temperature, diameter, particles represented by a single parcel, and the injection time of each parcel. The parcels are randomly distributed across the pool area and sized based off a distribution [Borkowski 1986]. The particles are assumed to be solid UO₂ contaminant suspended in a fuel droplet. The droplet mass fractions of heptane and uranium dioxide contaminant were chosen to be 0.98 and 0.02 respectively, based off of the pool mass fraction. The injection height was fixed at 10 mm off the pool surface for the base scenario, and parcels were given a random velocity normal to the pool. The particles were birthed at an assumed temperature of 370 K, one degree lower than the boiling point of heptane. Quantitative grounds for injecting particles are outlined in the above sections.

4.2.3.3.5 Radiation boundary conditions

The radiation boundaries were modeled with an emissivity of 0.9. Emissivity and absorptivity are assumed to be equal through Kirchoff's law. The tunnel wall material was modeled as stainless steel using a 1-D conduction model.

4.2.3.3.6 Particle boundary conditions

All surfaces in the multi-component boiling scenarios were assumed to be 'stick' boundaries, which collect particles that collide with that boundary. Species mass, total deposited mass, and number of particles represented per parcel are recorded on the boundary nodes. The resuspension scenario employed the general resuspension boundary that calculates a force balance on collided particles to determine if they adhere. Subsequently, the force balance is applied to adhering particles to determine if they will resuspend into the flow. For all other scenarios, any particle collision on a boundary sticks the particle without the possibility of re-emerging, because the surfaces of the facility were assumed to be easily wetted. For the

resuspension scenario, the surface roughness, ϵ , was 5.0×10^{-5} m, and the lift and adhesion forces were equations (2-1) and (2-2) respectively.

4.2.3.3.7 Simulation Scenarios

The parameters and uncertainties described in the above sections were used to create a set of variations from the base simulation. Table 4-5 lists the simulation number and their variations on individual parameters. The suffix “B” denotes the boiling entrainment mechanism, while the suffix “R” denotes the resuspension entrainment mechanism. Only one resuspension simulation was performed as the parameters and form for the model have yet to be verified to be accurate for this scenario. The injection height is the distance above the pool surface where the parcels are birthed, and the duration is the duration of the boiling regime (i.e. as the time over which particles are injected).

Table 4-5 Entrainment Scenarios

Run	Sim. Time (s)	Boiling Duration (s)	Fuel Pool	Injected Mass (kg/s)	Particle Size (um)	Turbulence	Injection Height (mm)	Parcel Temperature (K)
1B	25	17	Gas vel.	8.3×10^{-3}	Dist.	Normal	10	370
2B	35	27	Gas vel.	8.3×10^{-3}	Dist.	Normal	10	370
3B	25	17	Gas vel.	8.3×10^{-3}	Dist.	High	10	370
4B	25	17	Gas vel.	4.15×10^{-3}	Dist.	Normal	10	370
5B	25	17	Gas vel.	1.25×10^{-2}	Dist.	Normal	10	370
6B	25	17	Gas vel.	8.3×10^{-3}	Dist.	Normal	5	370
7B	25	17	Gas vel.	8.3×10^{-3}	Dist.	Normal	10	361
1R	50	17	1D pool, 0.002 m	8.3×10^{-3}	Dist.	Normal	10	370

A text description of each variation is listed in Table 4-6. The uncertainty of the boiling duration and height are represented in 2B, where boiling is extended from 17 seconds to 27 seconds, while 4B and 5B alter the fuel height from the base 2mm to 1mm and 3mm respectively. Scenario 3B increases the turbulence intensity from 20% to 100%. The particle injection height was another unknown, so 6B lowered the injection height to 5mm. Uncertainty existed as to the exact temperature of the volatile component in each parcel, so the temperature of the particles was lowered to 361K in scenario 7B. Scenario 1R was the resuspension scenario, which experimentally ran for 4.8 hours, but was modeled for 20 additional seconds in the simulation.

Table 4-6 Entrainment Simulation Variations

Case	Variation from Baseline
1B	Baseline. 25 second simulation, 10 mm particle injection height, particle size distribution, empty pan (high lip) mesh, 370 K particle injection temperature, and gas velocity representing the fuel pool.
2B	Simulated for 35 seconds with particle injections from 3 to 30 seconds.
3B	Turbulence parameter increased to 100%
4B	Fuel pool height lowered to 1 mm.
5B	Fuel pool height increased to 3 mm.
6B	Particles injected at 5 mm above the bottom of the fuel pan.
7B	Particle injection temperature decreased to 361 K
1R	Resuspension mechanism. 50 second simulation 1-D pool model [Brown 2006], 2 mm fuel height, 50 μ m surface roughness.

4.2.4 RESULTS AND DISCUSSION

The filter location in the original experiment and the outflow model boundary are closely situated, meaning the accumulated mass on this surface is representative of the experimentally collected mass.

4.2.4.1 Multiple Species Entrainment

The contaminant mass deposition on various surfaces is plotted as a function of time for the baseline scenarios in Figure 4-12. Figure 4-13 displays the number deposition prediction. Deposition values become constant shortly after the particle injections stop at 20 seconds as the suspended mass finishes depositing. The majority of the particles emitted during the boiling phase are predicted to deposit back on the pool or the pool lip. Some deposit on the walls of the facility, but more find their way out of the facility to the model 'outflow' boundary.

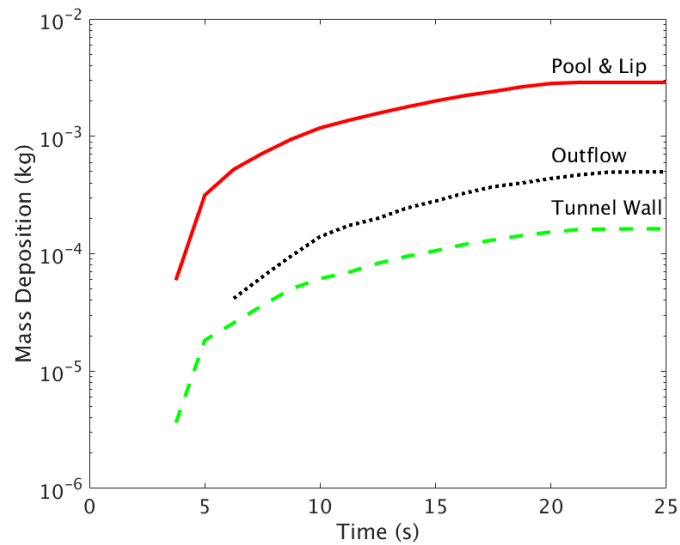


Figure 4-12 Boiling: Predicted contaminant mass deposition vs time (1B).

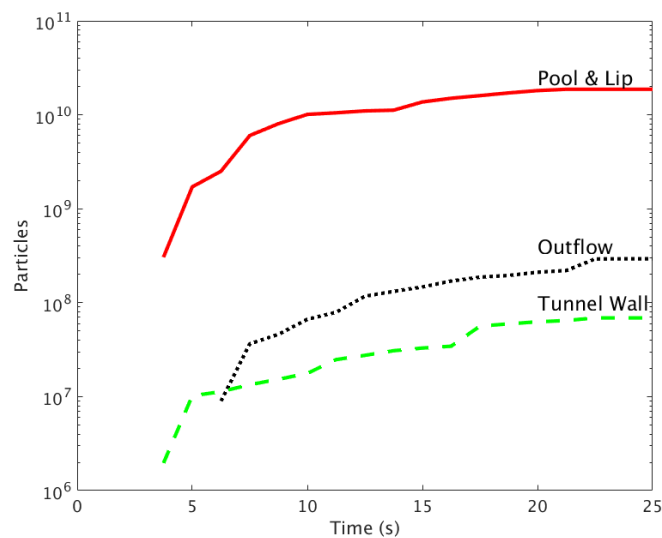


Figure 4-13 Boiling: Predicted number deposition vs time (1B).

Figure 4-14 and Figure 4-15 display the predicted final mass location for the heptane fuel and the uranium dioxide contaminant respectively. For the heptane fuel, only a portion of the injected fuel is deposited, while the rest evaporates in the flow. Of the deposited mass, the majority settles back onto the pool surface, followed by a significant percentage being deposited onto the pool lip. Less than 0.2% of the deposited fuel is located on the walls or outflow, so representation of this is omitted from the figure. The majority of the contaminant similarly deposits on the fuel pool, followed by the pool lip. However, a significant portion of the contaminant collects on the tunnel walls and outflow. More contaminant deposits on the outflow compared to the previous work that did not model the multi-component evaporation of the particles. In the current work, the fuel component of the particles is seen to evaporate quickly, leaving the smaller solid contaminant particles more susceptible to the flow due to enhanced entrainment of smaller particles in air flows. Previously reported in Year 1, only 0.6% of the injected mass deposited on the outflow, compared to 5% here.

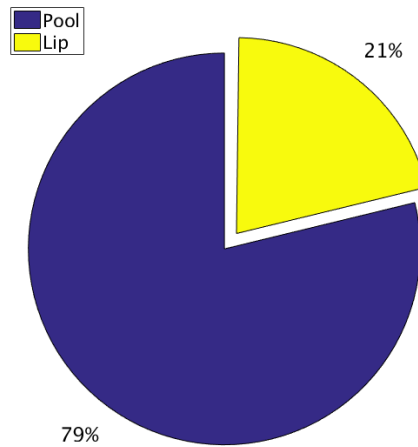


Figure 4-14 Predicted mass fate for heptane; boiling case 1 (1B).

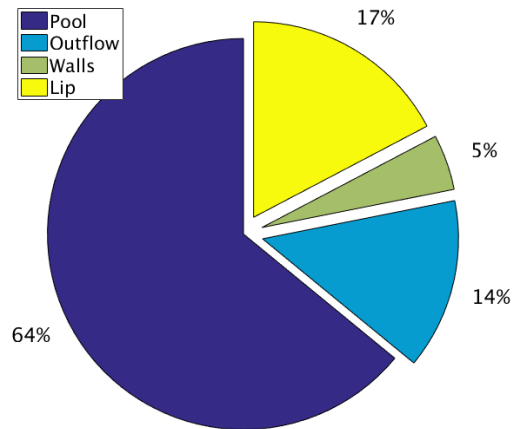


Figure 4-15 Predicted mass fate for the contaminant; boiling case 1 (1B).

The final deposition breakdown of the contaminant for all scenarios is shown in Figure 4-16. The values were calculated by comparing the deposited contaminant mass on the various surfaces to the total deposited contaminant mass.

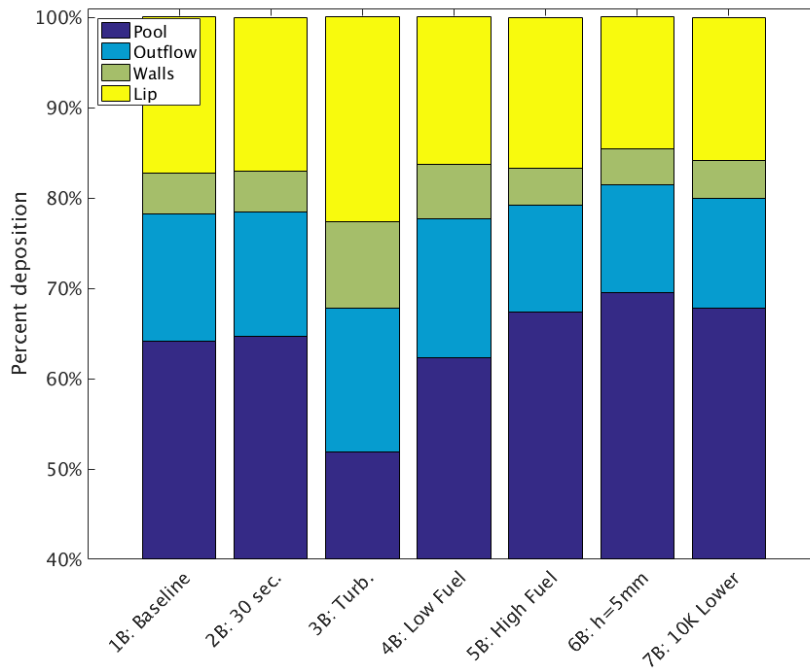


Figure 4-16 Predicted contaminant boiling atomization entrainment scenario: UO₂ mass deposition.

Comparing case 2B to 1B shows that the surface deposition percentages do not change appreciably with an increased boiling time. As seen in the previous work, increasing the turbulent intensity increases the percent of contaminant deposited on the lip, walls, and outflow.

Particle transport is affected by the turbulence parameters through a continuous random walk model that mimics the effect of sub-grid eddies. Lowering the fuel height (4B) did not significantly alter the deposition percentages, while raising it (5B) slightly increased the deposition on the lip and pool surfaces. Lowering the injection height (6B) increased the pool deposition mass. Lowering the temperature assigned to each particle at the injection time (7B) slightly increased the amount of contaminant deposited on the pool while lowering the outflow deposition percentage. Of the parameters varied, the results were most sensitive to the turbulence parameter variations.

Figure 4-17 displays the predicted airborne release fractions for the various scenarios alongside the reported experimentally determined release fraction. Lacking certain experimental feature information such as turbulence conditions, boiling duration and inflow velocity contributed to the discrepancy between experimental and predictive values.

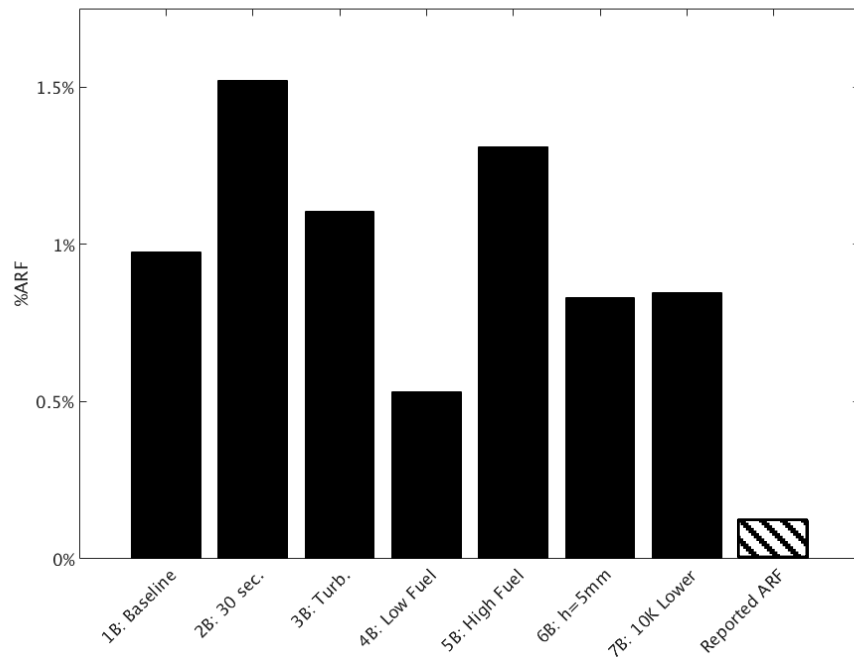


Figure 4-17 Predicted and Reported Airborne Release Fraction.

Compared to the previous work, the majority of the scenarios presented here involving multiple species particle tracking result in higher ARF values than those seen in the single component scenarios. While this deviates more from the reported ARF, the multiple species involve increased physical fidelity. The increase in ARF was expected, since the volatile fuel evaporates off from the particle surface, leaving the significantly smaller solid contaminant. The reduced particle diameter enables a greater percentage of contaminate to entrain into the flow and pass through the outflow boundary, while the previous work saw more particles descend back to the pool surface. In comparison with experimental data, our simulations with multi-component evaporation model predict higher ARF.

4.2.4.2 Resuspension Entrainment

The newly implemented resuspension capability results are included in this simulation. While particles resuspend (Figure 4-18), outflow contaminant levels did not change in the additional 20 seconds of simulation time. Given a longer simulation time and with tuned resuspension parameters, additional contaminant would be expected at the outflow boundary. Particles were observed to leave the pool, lip, and wall surface; however, they were only observed to redeposit nearby.

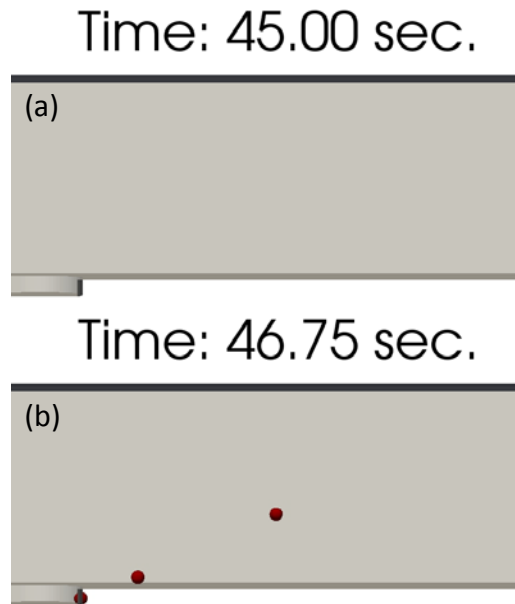


Figure 4-18 Resuspension mechanism: (a) all particles have adhered to surfaces or exited the domain, and (b) resuspended particles have re-entered the flow. Particle size is exaggerated for visibility.

The mass departure and addition rates from the various surfaces were not found to be linear in the simulation time, and therefore no attempt was made to predict entrainment. While a simulation prediction of the experimental resuspension entrainment was not successful in this work, the framework exists and was shown to be capable of providing such a prediction.

4.2.4.3 GENERAL DISCUSSION

Including the multi-component particle capability in this study provided significant insight into the entrainment dynamics observed in the boiling scenarios. Observing that the volatile fuel component evaporates rapidly, the solid, non-volatile contaminant is seen to entrain through the outflow in higher volumes, as the smaller particle size is more easily suspended in the flow. If a particle escaped the pool, above the lip, the contaminant would likely entrain and deposit on either the tunnel walls or the outflow.

An effort to determine the resuspension entrainment contribution to the ARF did not provide the anticipated level of insight, but the capability was shown to be functional. One consideration is that the resuspension model presented here is formulated for solid particles. No consideration towards the adhesive force from the surface tension is included.

As in the previous work, the time duration of boiling appears to be the most critical of parameters in determining the entrainment for the boiling mechanism. A boiling time of less than 5 seconds is projected from existing simulation results to match the experimental results. A separate project is currently developing a volumetric model for a burning liquid fuel layer using a volume of fluid model. This effort may produce a model that can be used in the future to quantify boiling times.

The distribution of the solid contaminant was ignored in this work, as the precise distribution is unknown. A drop including multiple contaminant particles was predicted to behave as a single particle with an aggregate spherical dimension of contaminant. The contaminants are thought to settle to the bottom of the fuel pool in the physical experiment. In this work, there was no way to assess the distribution of particles in the fuel, so the fuel was assumed to have a uniform contaminant distribution equal to the initial distribution. This subtle feature may be significant to the ARF for these scenarios, and needs to be evaluated in more detail than was found in historical experimental work.

Varying the turbulence parameters was shown to result in significant uncertainty in the deposition locations. Precise modeling of turbulence remains a modeling challenge for CFD scenarios, however the large uncertainty assumed is encompassed by the experimental uncertainty due to a lack of reporting of turbulence in the experimental work. This omission could be resolved by additional tests with a closer focus on providing adequate boundary condition descriptions for model predictions.

4.3 Summary and Conclusion

This chapter reanalyzes the beaker and gasoline pool fire simulations described in Year 1 of this project. Both the new resuspension I and the multi-component evaporation models for Fuego improvement were used in the simulations reported in this chapter.

We concluded the following:

Beaker Fire Experiment:

Our results indicate that contaminant released from burning fuel via entrained contaminant droplets is not principally due to initial flame dynamics, though observed in the original study [Brown 2015a] with non-evaporating inertial particles. The variation of the particle insertion data played the largest role with turbulence variation near the pool surface showing less importance. Initial pool height had the largest impact, and, as in the earlier study, it is clear that more experimental results would be helpful in exploring this variation. Since the goal of the DOE handbook is to provide conservative estimates for these scenarios, and greater contaminant release rates were observed both at lower (0mm) and higher (40mm) pool heights than the nominal 20mm, variations in pool height should be explored further.

Gasoline Pool Fire Experiment:

For the gasoline pool fire experiment, we concluded the following:

- Multiple entrainment mechanisms were presented as potential methods for hazardous contaminant release from contaminated fuel fires.
- The predicted ARF calculated by a CFD code was compared to the ARF measured in a relevant historical experiment and previous computational work. The addition of multiple species evaporation and deposition for particles provided new insight into the entrainment dynamics. The volatile fuel was seen to evaporate rapidly in the fire above the pool surface, increasing the likelihood that the remaining non-volatile solid contaminant would transport down the wind tunnel and reach the outflow.
- Practical assumptions for the turbulence boundary conditions result in significant uncertainty in the ARF.
- Boiling mechanism duration was again found to be the most significant factor in predicting the ARF. Improved modeling of particle entrainment from pool boiling will help quantitative accuracy of this type of modeling.
- The particle input temperature did not significantly alter the volatile evaporation, resulting in similar contaminant release.
- Future work would include longer duration simulations of the resuspension of deposits left from a multiple component boiling entrainment scenario in order to detect contaminant release at the collection point, potentially enabling a prediction of the resuspension entrainment ARF.

5 REANALYZING POWDER RELEASE EXPERIMENTS

As a part of the re-analysis task in Year 2 for the powder release experiments reported in Year 1 of the project, we include the gravitational spill experiments from the same facility apparatus used in Pacific Northwest Laboratories (PNL) [Sutter 1981]. In Year 1, we did the exploratory simulations for the pressurized powder release experiments [Sutter 1983]. In this year, we re-analyzed the pressurized powder release experiments with Fuego and coupled with Presto code for simulating the 250 psig test. Note that we will not discuss any MELCOR simulations in this project, since the NSRD-10 project is devoted entirely to MELCOR simulations on leak path factor guidance [Louie 2016]. In the NSRD-10, the MELCOR simulations include the powder release experiments as described in this chapter. The intent there is to validate MELCOR 2.1, and at the same time to substantiate the release data in DOE-HDBK-3010 [DOE 1994]. Also note that the Fuego results reported in both spill and pressurized releases will be used in MELCOR simulations, since the aerosols in MELCOR do not affect the hydrodynamic of the fluids. Thus MELCOR treats aerosols as trace elements. The Fuego results, such as induced fluid velocities from the falling of the aerosols in the spill experiments, will be used in MELCOR to simulate subsequent induced fluid movements by the aerosols.

In this chapter, the gravitational spill experiment of a 100 g of TiO_2 is described first. Then the pressurized releases of 100 g TiO_2 for the 3.45×10^5 Pa (50 psig) and 17.25×10^5 Pa (250 psig) tests are described. Note that the meshing method used in the Fuego simulations is different from Year 1. An attempt was made to use a better mesh method to simulate any turbulences and deposition of the particles.

5.1 Gravitational (Free-fall) Spill Experiments

Gravitational or free-fall spills are important in nuclear facilities across the DOE complex since spills tend to occur during handling of the radioactive materials, such as waste drum loading and transportation. A series of spill experiments were conducted at PNL for NRC in 1981 [Sutter 1981]. These experiments were conducted at the RART, which is the same tank as the gasoline pool fire experiments reported in Chapter 4. Figure 5-1 shows the sampling for a free-fall spill apparatus inside the RART with the sampling equipment. As shown in this figure, the RART is 2.9 m in diameter and 3 m height with a total free volume of 20 m^3 . The beaker (~ 1 liter in volume) containing the particulates is located at the center of the RART. The spill is simulated by overturning the beaker. The particulates include both liquid and powders (TiO_2 and depleted uranium dioxide). The spill height is ranging from 1 m to 3 m. Also shown in this figure is the sampling equipment, which contains 4 high-volume filters and a cascade impactor. The locations of the sampling are shown in this figure. The sampling is done by pulling specific air flow through the sampling equipment to be measured as the airborne release amount. The specific flow rate, pulling eight times of RART volume in 30 minutes is described in the next section. Although the experiments were measured as a function of mass (25 g to 1000 g), materials and forms (such as liquid or powders), the specific test in this section focuses on TiO_2 and 100 g of powder. Because of the limitations of the particles being modeled, the Fuego simulation was only conducted for 100,000 particles with each particle associated with a parcel of 1000 as described in the following subsections. The simulation attempts to establish any fluid flow from free-fall of the aerosols simulated. This fluid flow would affect how the aerosols

behave and the influences of the sampling flows, since it pulls the air into the sampling equipment, which can cause disruption of the aerosols falling.

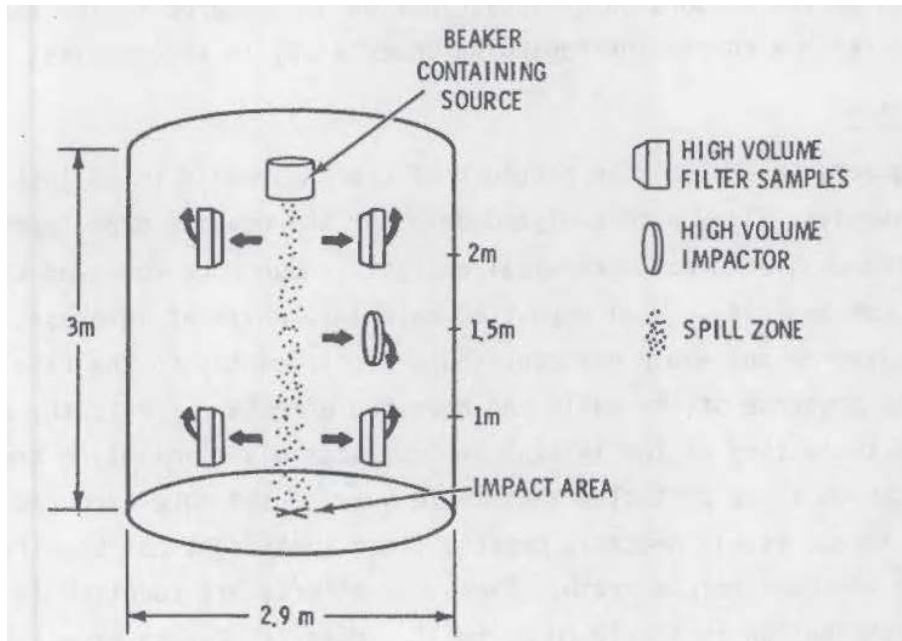


Figure 5-1 Free-fall Spill Experiments in RART [Sutter 1981].

5.1.1 Experimental Data

This section describes the experimental data for the free-fall spill experiment at a spill height of 3m using 100 g of TiO_2 powder. Table 5-1 shows the specific experimental conditions and results for this test. The dimensions of the beaker were not given in the experiment report. It was only identified to have one liter in volume. Also shown in this figure is the flow rate associated to the sampling devices. Using the flow rate, the calculated total flow in 30 minutes is 168 m^3 for all high volume filters, which is slightly higher than the 8 times of RART volume of 160 m^3 . This does not account for the impactor flow of 16.8 m^3 . Table 5-2 shows the initial particle distribution used in the Fuego simulation. As shown in this table, the size of the particles can be calculated.

Table 5-1 Experimental Data for 100 g TiO_2 , 3-m Free-fall Spill Test [Sutter 1981]

Parameter	Value
RART Dimension:	
Diameter, m	2.9
Height, m	3.0
Beaker:	
Volume, liters	1
Powder:	
Mass, g	100*
Material	TiO_2
Drop height, m	3
Filters** specifications:	
Location from the bottom of RART, m	1 and 2
Filter height, width, and assumed thickness, m (inches)	0.2 (8), 0.25 (10), 0.02(1)

Designed flow rate each, m ³ per minute	1.4
Duration, minutes	30
Impactor specifications:	
Location from the bottom of RART, m	1.5
Dimension: height, width, and thickness	Assumed same as filters
Designed flow rate, m ³ per minute	0.56
Duration, minutes	30

*A particle distribution as shown in Table 5-2 is used, instead of mass mean diameter (MMD) of 1.7 μm and standard deviation of 2.

**Glass fiber filters with 99.9% efficient for 0.3 μm

Table 5-2 Source TiO₂* Powder Distribution in Measured Cumulative Mass Percent [Sutter 1981]

Size (μm)	Mass Percent (Cumulative)
20	98
10	97
8	96
6	94
4	88
2	60
1	16
0.8	11

*TiO₂'s density is 4.26 g/cm³ of theoretical density. Note that the total number of particles is 1.455E+13.

5.1.2 Fuego Simulation

This section describes the Fuego simulation conducted for the free-fall spill test as described in the previous section. Because of recent significant development in the particle modeling, such as resuspension, we use an older version of Fuego for the simulations (4.39.8). This version does not contain the latest resuspension particle model described in Section 2.1. The current version (4.40) has the following improvement:

- Changed the legacy “STICK” model to actually stick rather than just deleting the particles
- Added additional input argument checking for the resuspension models.
- Changed wall shear stress “tauw” to include turbulent fluctuations. The non-fluctuating value is “tauw_mean”. This model is described in Chapter 2.
- Added the turbulent kinetic energy as an input option for the resuspension functions.

For this simulation, the particle resuspension is not important since there is no additional flow in the simulation, except the low flow in the sampling equipment. We attempt to simulate the entire run time of the experiment which is 30 minutes. In the following subsections, we will describe our modeling assumptions, discuss the simulation results, and provide a summary and conclusion for the simulation.

5.1.2.1 Modeling Assumptions

This section describes the modeling assumptions that we used. To improve upon Year 1's simulation, we use a finer mesh to represent both RART and PARE volumes of the experiment. The specific data assumptions are described.

Meshes

The mesh described in this section utilizes the techniques commonly found in CFD simulations [Zigh 2013, Tutar 2001, ANSYS 2012, Rodriguez 2013]. The mesh aspect ratios were less than 5, skew was less than 0.5, and growth rates were less than 1.5. We generated meshes containing 1.0, 4.4, 9.0, 18.1 million hexahedral elements. Figure 5-2 and Figure 5-3 show the overall mesh grid and detailed 2-D mesh in the PARE region used in this simulation, respectively.



Figure 5-2 Mesh used for Gravitational Spill Simulation, Containing ~10 Million Elements.

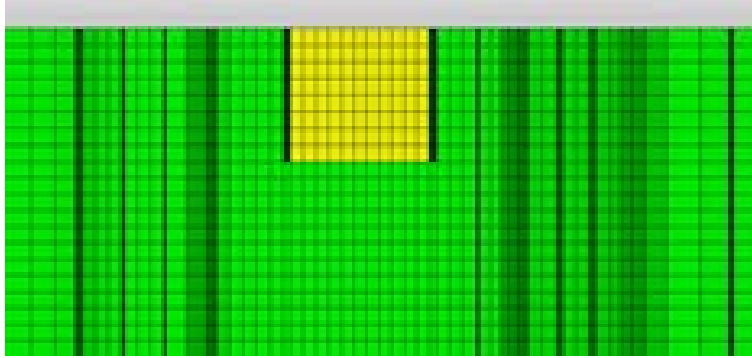


Figure 5-3 Two-Dimensional Mesh Near the Beaker (384 element mesh) at the Ceiling of RART.

Data

The locations of the filters and impactor are shown in Figure 5-4 which are based on the elevations in Figure 5-1. The assumed sampling flow rates are shown in Table 5-1. Note that this flow rate has a ramp rate of 0.1 m/s at 0.1 s for the four filters. Additional assumptions are shown in Table 5-4. The specific inputs for Fuego are included in Table 5-5 for the turbulence model. The parameters shown in this table helped guide the generation of the Fuego mesh and input models. For example, the element length of the coarsest mesh (1.0 million elements) was generated such that it was sufficiently small to capture the integral and Taylor eddy turbulent physics, while still providing results within a reasonable amount of time. The finer meshes were generated to investigate the convergent behavior as the element size decreased, as well as to capture the Kolmogorov eddies.

The geometry and flow characteristics of the experiment guided our choice for turbulence models. The experiment involved a wide range in Reynolds number (Re), from very high within a few seconds of transient initiation, to low Re in the laminar regime after about 40 seconds. The experiments showed considerable swirl caused by the particles and was also influenced by the filter's airflow. Further, the lateral walls were cylindrical and thus had significant curvature. These make large eddy simulation (LES) a great choice to capture the physics of the problem. The dynamic Smagorinsky LES turbulence model was selected to capture the large energy-containing eddies that had the greatest influence on the particle's motion. However, to perform a more comprehensive investigation of turbulence models on aerosol distribution, we also considered the 2006 $k-\omega$ [Wilcox 2006], the k subgrid scale (KSGS) [SIERRA 2016d], and direct numerical simulation (DNS) [Wilcox 2006] turbulence models. For the KSGS LES model, the turbulence initial kinetic energy (k) is a required input parameter. It is noted that at time zero, there was no aerosol motion, and that the aerosol was violently ejected within a few milliseconds. We therefore considered two values for k as sensitivity studies, 0.0 and $2 \times 10^{-3} \text{ m}^2/\text{s}^2$. We note that Fuego is a second-order spatial code, and that, generally, DNS calculations are performed with 4th-order spatial codes. However, the literature also has successful usage of 2nd-order codes to obtain key DNS output [Wilcox 2006, Rodriguez 2014].



Figure 5-4 Locations of the Filters and Impactors Relative to RART Dimension.

Table 5-3 Assumed Sampling Flow Rates

Sample	Designated Flow Rate (m/s)
High Volume Filter*	0.452
Impactor	0.1809

*Ramp rate: 0.1 m/s at 0.1 s and designated rate at 1 s

Table 5-4 Additional Simulation Assumptions

Model	Description/Assumption
Sampling	Each filter/impactor had its own time-dependent air flow boundary
Fluid condition	No fluid motion initially, all induced by the drop of the powders from the beaker.
Beaker dimension	1-liter, but a height of 9.52 cm and 9.92 cm in diameter.
Particle treatment	100,000 particles were modeled, using data from Table 5-2. A particle file has been generated to document the particle coordinate in the beaker. This file is used by Fuego.
Particle deposition	Filters and walls allow for particle deposition or “stick”. All particles that struck on a surface remained attached for the duration of transient
Problem time	1800 seconds as specified in the experiment.

Table 5-5 Turbulence Parameters Used in the Spill Test

Parameter	Values
X_{char} , m	2.9
U_{char} , m/s	0.01 (near transient end)
Re	1.84×10^3
Wall friction velocity, m/s	9.22×10^{-4}
$y(y^+=1)$, m	1.71×10^{-2}

Ratio of turb. visc. vs. viscosity	9.85
Turbulence intensity	6.25×10^{-2}
Specific turb. kinetic energy, m^2/s^2	5.87×10^{-7}
Eddy dissipation, m^2/s^3	1.99×10^{-10}
Integral eddy size, m	2.26
Taylor eddy size, m	6.82×10^{-1}
Kolmogorov eddy size, m	6.67×10^{-2}

5.1.2.2 Discussions of the Simulations

The powder was released vertically from the beaker, allowing gravity to force the particles in a downward direction. The simulation shows the formation of dust clusters that first reached the bottom of the RART at around 50 seconds for the larger particles (see Figure 5-5). As shown in Figure 5-5, the floor consists of 3-ring regions (inner, middle and outer) which is intended to provide data to compare with MELCOR results in the NSRD-10 project [Louie 2016]. The smaller particles first reached to the floor at 200 seconds, and continued settling during the entire transient. Figure 5-6 and Figure 5-7 show the particle velocity and fluid velocity at ~200 seconds. As shown in Figure 5-7, the sampling flow (toward the filter and impactor) had a high degree of influence on particle motion, particularly for the smaller particles which tend to stay airborne.

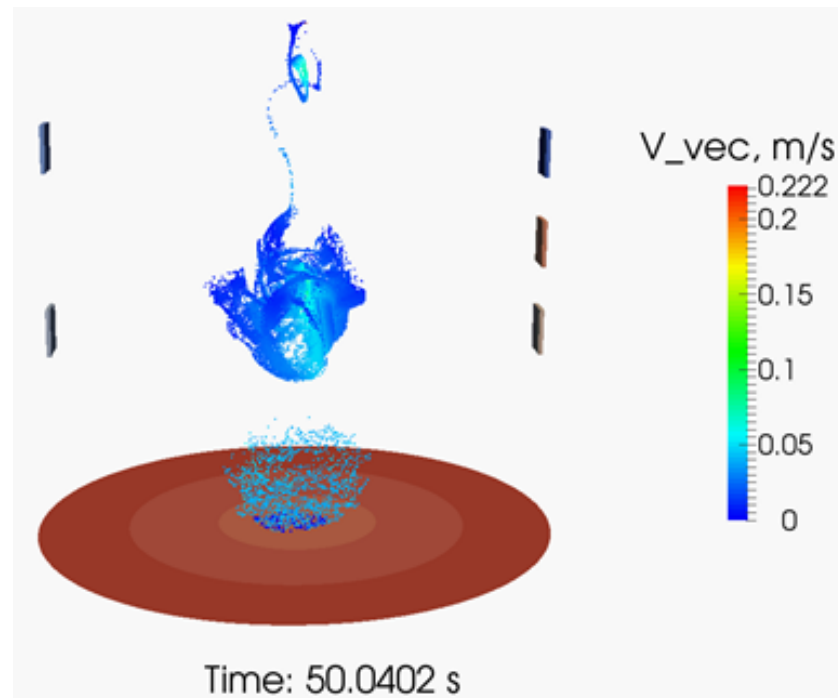


Figure 5-5 Particle Velocity Predictions from 3-m Spill Simulation at ~50 seconds.

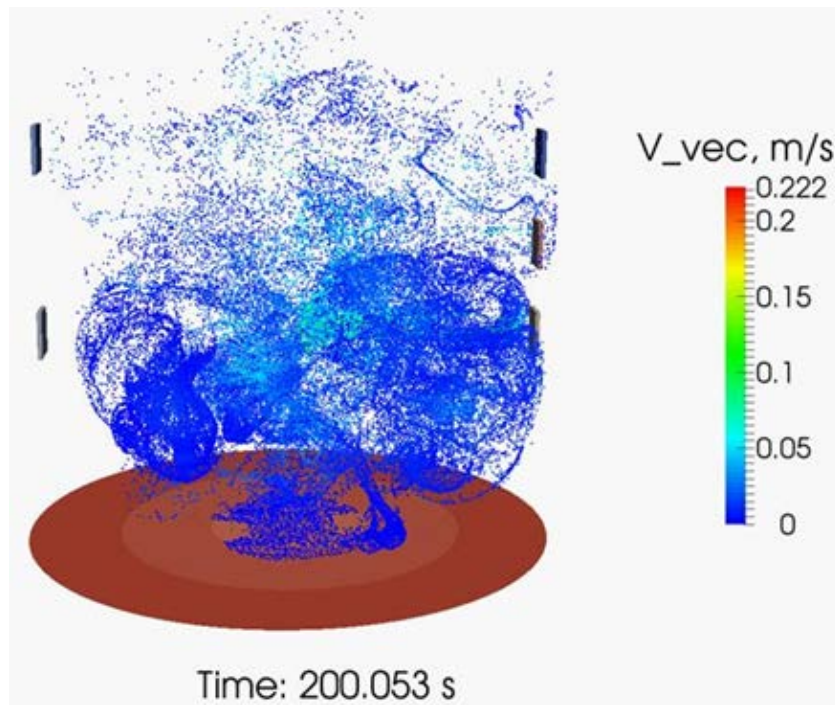


Figure 5-6 Particle Velocity Predictions from 3-m Spill Simulation at ~200 seconds.

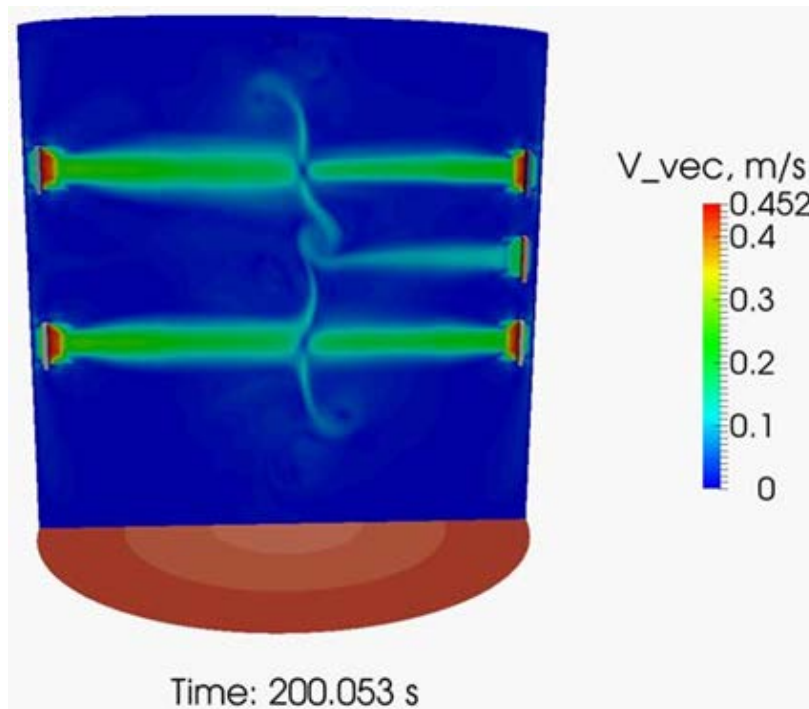


Figure 5-7 Fluid Velocity Distributions from 3-m Spill Simulation at ~200 seconds.

In terms of particle depositions onto the floor and onto the samples (filters and impactor), Figure 5-8 shows the Fuego simulation results. As shown in this figure, the middle ring floor yields the highest value, followed by the outer ring. The least is in the inner ring. This behavior may be caused by the total cross-sectional area in each ring and the sample flow near the outer region of the RART volume so that the particles near the outer region may be pulled by the sampling flow. The middle region may not experience a larger sample flow than the outer region. The lowest deposition is in the inner region, since it was evidenced in early time that the larger particles settled at the inner and middle regions. The deposition in the samples (filters and impactor) as shown in this figure shows about 4 %, compared to the experimental data of 0.11%.

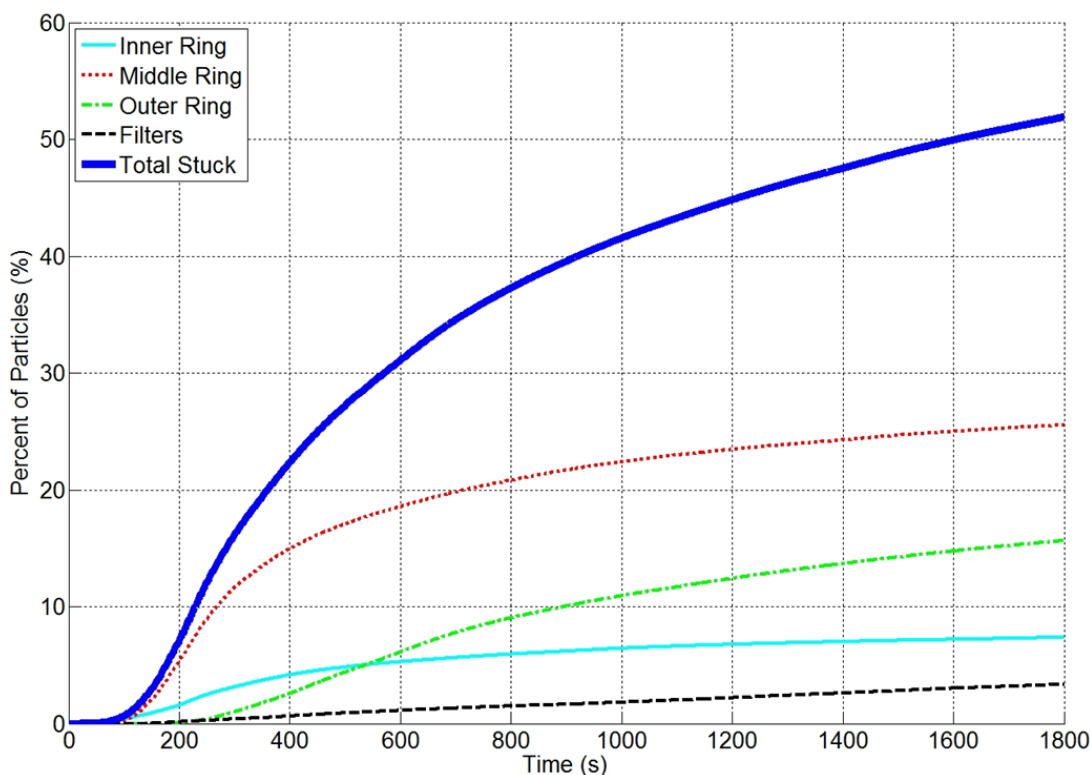


Figure 5-8 Fuego Simulation on the Particle Depositions at Various Locations (Ring location on the floor).

5.1.3 Summary and Conclusion

A gravitational (free-fall) spill simulation of 100 g of TiO₂ powder has been done. We have used a fine mesh for this simulation. We model both the prescribed sample flow and introduce a turbulence model. The drop of the particles influences the hydrodynamic fluid in the RART volume. The induced fluid velocity can be used by MELCOR in the NSRD-10 project [Louie 2016]. We were able to run the simulation to the experiment end time of 30 minutes, which is a great accomplishment in CFD simulations.

However, the aerosol result of the simulation overestimates the ARF in terms of the particles collected in the samples. This difference may be due to the following factors:

- Fuego currently does not model agglomeration, which may cause the settling to occur faster.
- The assumption of 10^8 particles (including the parcel value of 1000) in the model versus the actual number of particles of 10^{13} may overestimate the number of particles pulled through the samples.
- The turbulence flow model used may influence the mixing that causes the overestimation.
- The percent particle collected is a number percent, which may be different from the experimental data as a mass percent.

5.2 Pressurized Release Experiments

This section describes the pressurized release of the experiment conducted in RART as the same volume in the free-fall spill experiment discussed previously [Sutter 1983]. The only difference between this experiment and the spill experiment is the location of the release equipment and method. The release equipment for this experiment is a power enclosure that is called Pressurized Airborne Release Equipment (PARE). Figure 5-9 shows the schematic of the RART configuration for the pressurized release experiment. As shown in this figure, the sampling locations and types are identical to the spill simulation described previously. Figure 5-10 shows the layout of the PARE. PARE is placed on the center floor of RART. The test material is placed inside the PARE and pressurized with air to the test pressure. The release is due to the removal of the air between two designated rupture disks at design pressure. In this section, we describe the simulations of 50 psig (0.34 MPa) and 250 psig (1.72 MPa) tests for the release of 100 g TiO_2 .

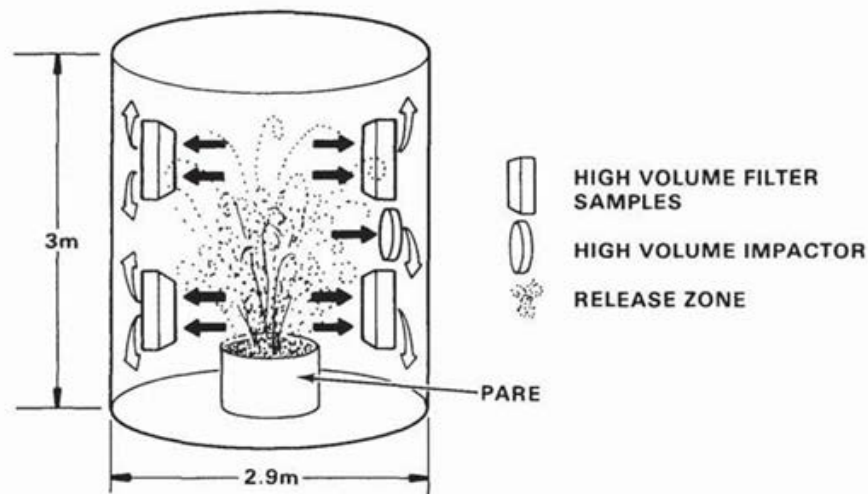


Figure 5-9 Schematic of RART for Pressurized Release Experiment [Sutter 1983].

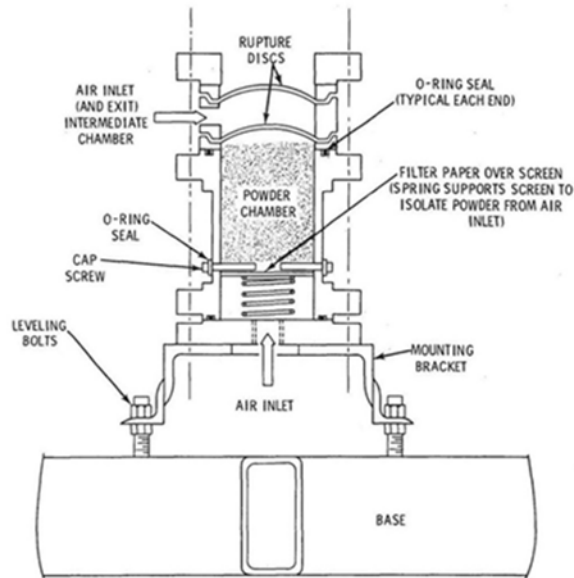


Figure 5-10 Layout of PARE [Sutter 1983].

5.2.1 50 psig (0.34 MPa) Test

This section describes the pressurized powder release of the 50 psig (0.34 MPa) test for 100 g of TiO_2 . This test can be simulated entirely using Fuego, because the Mach number for this test is 0.38, which is marginally in the subsonic range. Fuego is able to compute fluid behavior up to $\text{Ma} \sim 0.7$. In this section, we describe the experimental data we used first. Then we describe our Fuego simulation, along with the calculation assumption. Finally, we present the results and provide the findings of this study.

5.2.1.1 Experimental Data

Much of the data information for this test is similar to the free-fall spill test described in Section 5.1.1. Both tables described in Section 5.1.1 are applicable for this test. However, the release mechanism is pressurized release rather than a gravitational release.

5.2.1.2 Fuego Simulation

Similar to that of the spill test described in Section 5.1, we used version 4.39.8 of Fuego for this simulation. Table 5-6 shows the model assumptions used in the simulations. As in this table, the samplings have their own time-dependent flow boundaries. In addition, the mesh boundaries were broken up into side sets or surfaces [i.e., boundary conditions (BCs)]. The boundary associated with the PARE was set as a zero-velocity adhesive surface, meaning that the velocity at the wall will always be zero, and any particle that contacts the wall will stick and remain immobile for the remainder of the calculations. This makes all of our simulations somewhat non-conservative, as some particles may resuspend or bounce. However, for initial testing of the new aerosol models, this is a reasonable, first-order approximation, and more refined simulations will be conducted in the future. The PARE base was given a time-dependent velocity that accounts for a time-dependent release of the powder (see Table 5-7). This approximation is fairly accurate, as it reflected the behavior of the rupture disk, which requires a small, finite time to release its

pressurized contents. We chose an opening time of 0.5 millisecond, and performed several sensitivity studies for this input parameter to gauge its impact on the solution. The peak velocity (643.0 m/s) was based on a momentum balance. This corresponds to $Ma=0.38$, which is marginally in the subsonic range.

As shown in Table 5-6, the ceiling surface is modeled as a large, circular surface. The opposite side of the beaker was subdivided into three concentric boundaries, primarily so that the dynamic velocity distribution calculated by Fuego can be used as input for future MELCOR calculations (similar to the spill test described in the previous section). The concentric boundaries were set as zero-velocity adhesive boundaries. The filters were modeled using a “combined” aerosol option, causing all particles coming into contact with the filter to stick, with no possibility for reflection or resuspension. By contrast, the filter lateral sides acted as rebounding walls. In addition, the specified turbulence parameters in the simulation are shown in Table 5-8.

Table 5-6 50 psig (0.34 MPa) Test Simulation Assumptions

Model	Description/Assumption
Sampling	Each filter/impactor had its own time-dependent air flow boundary. The flow velocity is shown in Table 5-3.
Pressure Release	To simulate the rupture disk effect using the table function in Table 5-7.
Particle deposition	Filters and walls allow for particle deposition or “stick”. All particles that struck on a surface remained attached for the duration of transient.
Ceiling surfaces	The ceiling surface of RART is modeled as three concentric boundaries consistent to that of the spill experiment for the floor described in the previous section. The concentric boundaries were set as zero-velocity adhesive boundaries. See Table 5-9 for other simulation cases for the treatment of the ceiling surfaces.
Problem time	1800 seconds as specified in the experiment.

Table 5-7 50 psig (0.34 MPa) Test Simulation of Rupture Disk of PARE

Time (s)	Velocity (m/s)
0.0010	0.0
0.0015	643
0.0155	643
0.0160	0.0

Table 5-8 Turbulence Parameters Used in 50 psig (0.34 MPa) Test

Parameter	Values
X_{char} , m	2.9
U_{char} , m/s	0.2 (RART midpoint)
Re	3.67×10^4
Wall friction velocity, m/s	1.21×10^{-2}
$y(y^+=1)$, m	1.30×10^{-3}
Ratio of turb. visc. vs. viscosity	135
Turbulence intensity	4.30×10^{-2}
Specific turb. kinetic energy, m^2/s^2	1.11×10^{-4}

Eddy dissipation, m^2/s^3	5.18×10^{-7}
Integral eddy size, m	2.26
Taylor eddy size, m	1.84×10^{-1}
Kolmogorov eddy size, m	9.34×10^{-3}

For this simulation, we ran the model out to 30 minutes of the experiment. Figure 5-11 and Figure 5-12 show the particle velocity and fluid velocity results at 5 seconds, respectively. As shown in these figures, the particles inducted by the pressure are rising up, while the sampling flow begins to pull. At about 35 seconds (see Figure 5-13 for the particle velocity results and Figure 5-14 for the fluid velocity results), the particles reach the ceiling, while the sampling flow pulled at the center of RART. Although this simulation was able to reach to the end of 30 minutes, there was no significant deposition onto ceiling or by the sampling flow. Figure 5-15 shows the particles stuck to the surfaces versus the particles being airborne. As shown in this figure, about 35% remained in the PARE surfaces early in the simulation. At the end of 30 minutes, the additional 20% fell to the floor of RART. In order to capture the particles onto the filters and impactor, and in the ceiling as shown in Figure 5-9, we have simulated an additional five different cases. The primary reason we conducted these many cases is because there were issues related to the surface deposition (or stick) in Fuego. The open boundary for fluid would allow the particles to stick to the surfaces while the fluid is going through. That is why the cases in Table 5-9 are conducted. As discussed in Chapter 2, the deposition model in Fuego is based on many conditions, including the boundary layer, fluid velocity, particle velocity and size, and the angle of the particle incident to the surface. This model requires mesh refinement near the surface that could be sufficient to be within the boundary layer for the deposition if the particle travels in parallel to the surface. The Fuego developers indicate the improvement of this model is required. Figure 5-16 shows the use of the open boundary for ceiling surfaces at the inner, middle and outer ring. As shown in this figure, the outer ring has the most, because of the large surface area. In the actual situation, the total stuck to the ceiling may be lower than the results shown in this figure, because some particles may bounce back. Similarly, Figure 5-17 shows the comparison of the sampling locations that are being modeled as “no open” and “closed” boundary. The actual value of the percentage particles captured by the samples should be between the two curves as shown in this figure.



Figure 5-11 Fuego Results on Particle Velocity for 50 psig (0.34 MPa) Pressurized Release of TiO₂ at 5 seconds.

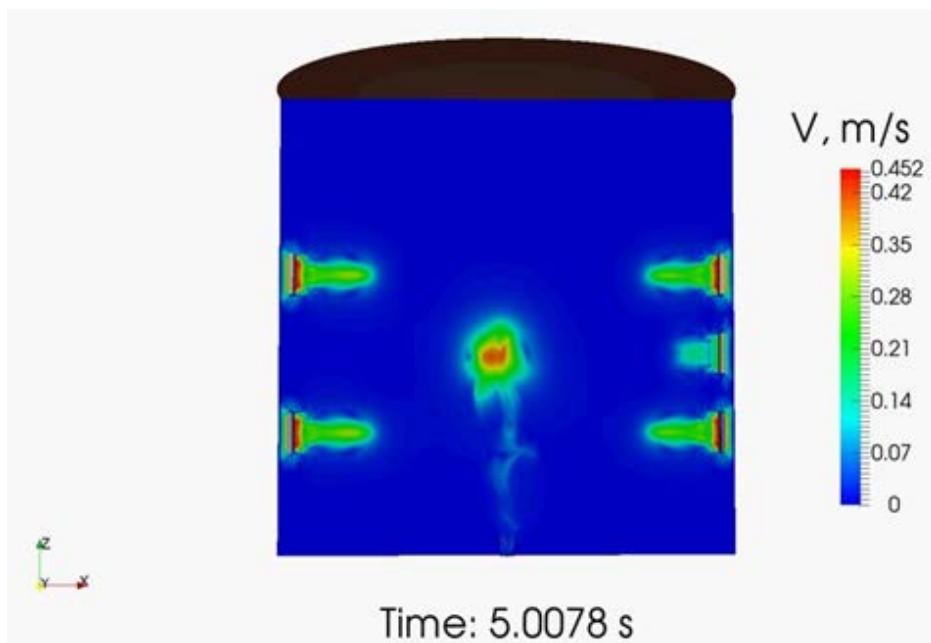


Figure 5-12 Fuego Results on Fluid Velocity for 50 psig (0.34 MPa) Pressurized Release at 5 Seconds.

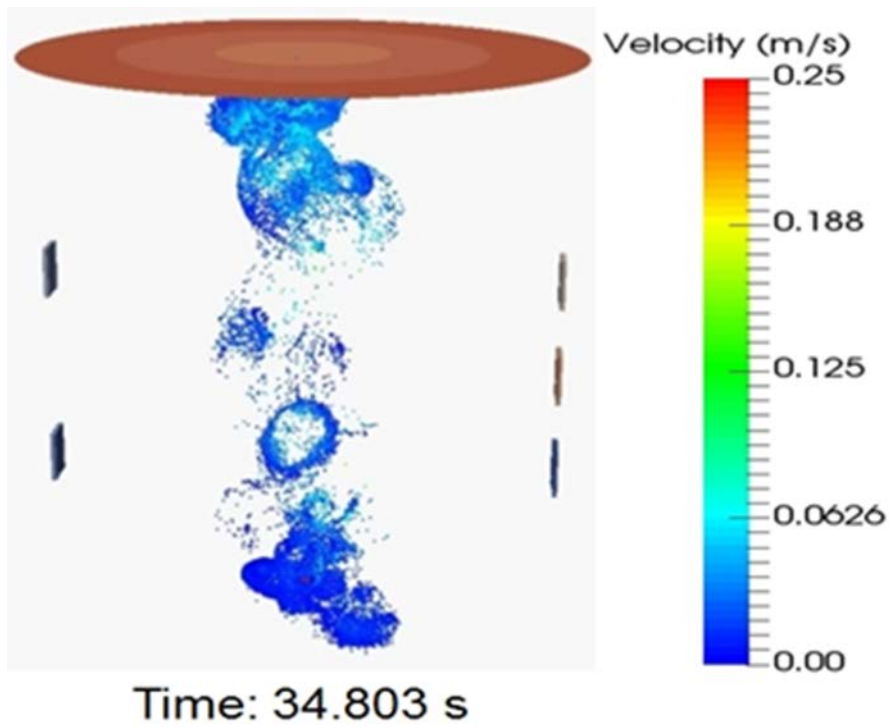


Figure 5-13 Fuego Results on Particle Velocity for 50 psig (0.34 MPa) Pressurized Release at 35 Seconds.

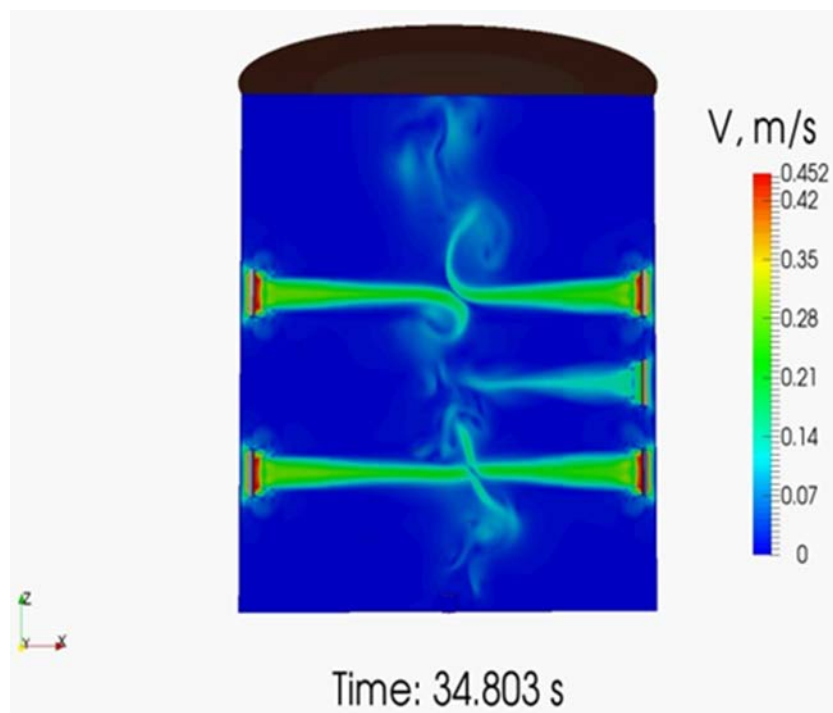


Figure 5-14 Fuego Results on Sampling Flow Effect for 50 psig (0.34 MPa) Pressurized Release at 35 Seconds.

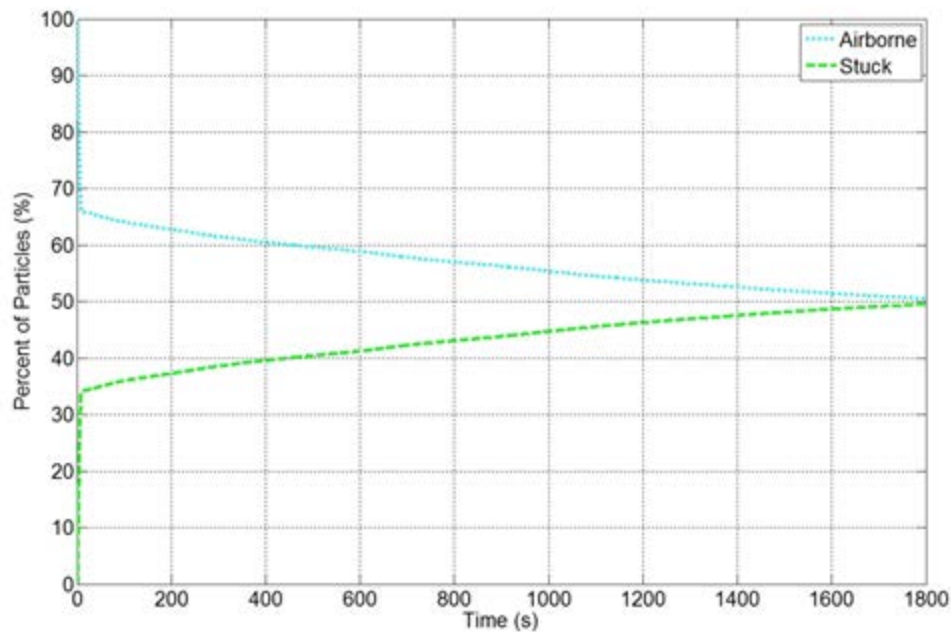


Figure 5-15 Percentage of Particles Airborne Versus Deposited for 50 psig (0.34 MPa) Case.

Table 5-9 50 psig (0.34 MPa) Additional Simulation Cases

Case	Description
No Open	All boundaries as “wall” boundary conditions with a specified time-dependent velocity.
Filter	Sampling surfaces have fluid open boundaries only.
Central	Inner ring at the ceiling has an fluid open boundary.
Middle	Middle ring at the ceiling has an fluid open boundary.
Outer	Outer ring at the ceiling has an fluid open boundary.

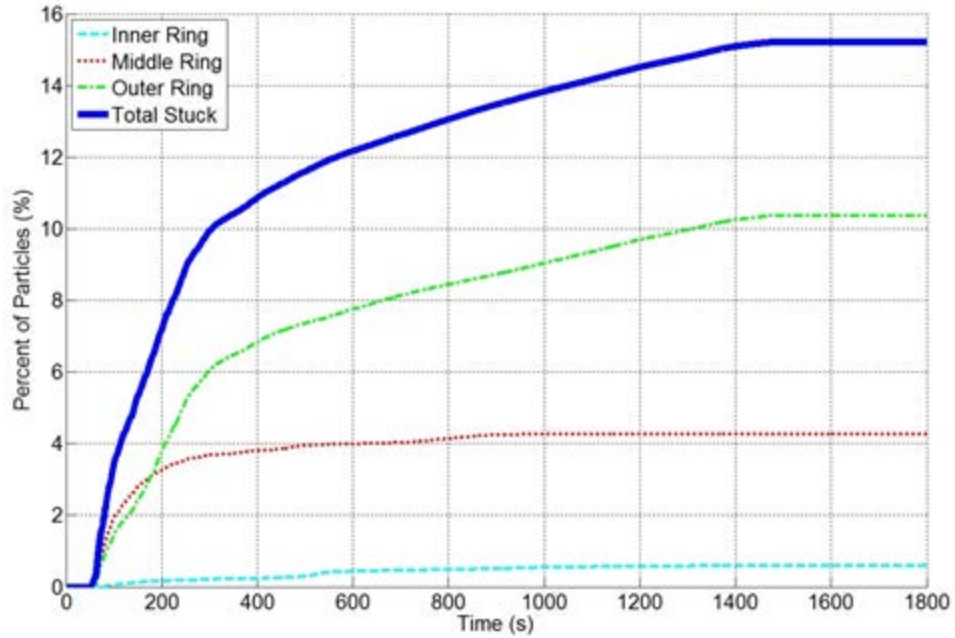


Figure 5-16 Particles Deposition for the Ceiling Surface Treatment for 50 psig (0.34 MPa) Test – Central, Middle and Outer Cases.

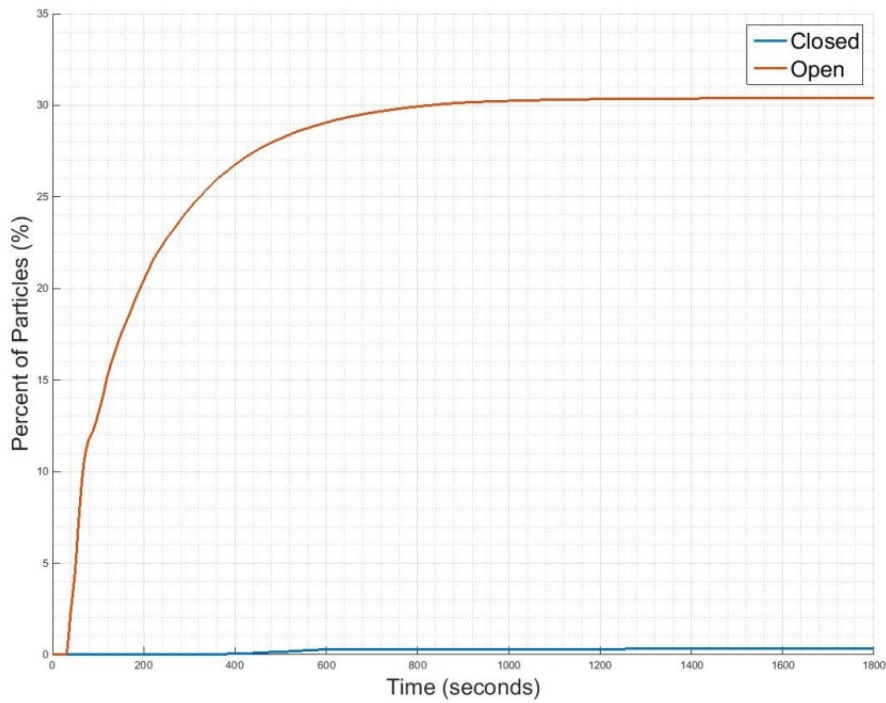


Figure 5-17 Comparison of Sampling Surfaces Treatment for 50 psig (0.34 MPa) Test – No Open and Filer Cases.

5.2.1.3 Summary and Conclusion

The simulations of the 50 psig (0.34 MPa) pressurized release of TiO₂ of 100,000 particles has been demonstrated with an improved mesh model compared to the Year 1's model and approach [Louie 2015]. The simulations were run out to 30 minutes of the experiment end time. During the simulation, the deposition of the particles onto the ceiling seemed to be difficult. As mentioned in Chapter 2, the deposition process is dependent on the boundary layer, fluid velocity, particle's size and flow direction. The combinations of these parameters determine whether or not the particle can be stuck onto the surface. It is also dependent on the turbulence model used in the simulation. As indicated in Chapter 2, the deposition model in Fuego can be improved. Without this improvement, several additional simulations were done for this pressure case to permit particles to deposit onto the ceiling. The ability to deposit onto the ceiling is important, since it would reduce the amount of particles in airborne and captured by the sample flow. This is particularly important for the higher pressure case. Increasing pressure should increase the deposition onto the ceiling which has been reported in the experiment.

5.2.2 250 psig (1.72 MPa) Test

This section describes the pressurized powder release for a 250 psig (1.72 MPa) test using 100 g of TiO₂ powder. The reason we cannot use Fuego to simulate the entire test is because Fuego is a low-Mach fluid dynamics code. It is only valid for Mach numbers less than ~0.7. Therefore, we use the SIERRA/SM code (Adagio or Presto, both are equivalent) to model the first few milliseconds of the calculation and output the necessary input information required for Fuego to continue the simulation. This approach is similar to modeling an explosion condition [Gelbard 2013]. This transfer of data from a solid mechanics code to fluids is considered one-way coupling. No feedback is modeled.

In the following three subsections, we will first describe the solid mechanics simulation to model the pressure release of the TiO₂ particles from PARE. Then, the translation of output from Presto to the input of Fuego is discussed. The only difference between the Fuego input for this coupling and that of the 50 psig (0.34 MPa) case is the additional particle input files. Finally, the Fuego simulations are described.

5.2.2.1 Solid Mechanic Simulation

Presto, the solid mechanics component of SIERRA, was used to simulate the explosive release of powder from a container [SIERRA 2016a]. The powder is modeled as spherical particles and the high pressure explosion is created by imparting an initial load of hydrostatic stress uniformly over all the particles. The material model used for the powder is based on a soil foam material model. A similar material model was used in Year 1 on the impact of an object to the powder can [Louie 2015]. In the SIERRA input deck, this is given by:

```
begin parameters for model soil_foam
  poissons ratio = 0.35          # sand not elastic but 0.3 to 0.4
  bulk modulus   = 502.836e+6    # based on air sound speed
  a0 = 0.0                    # set to zero for hydrodynamics material
  a1 = 0.95
  a2 = 0.0
  pressure cutoff = -1.0
```

```
pressure function = pressure_func
end parameters for model soil_foam
```

As the particles dispersed, they would contact the sides of the container and other particles, until ultimately ejecting upward. The simulation was continued until the total kinetic energy of all the particles reached their asymptotic peak. Beyond this point, the particles were handed off to Fuego to continue the calculation.

For the Fuego calculation, a specific set of particle quantities are needed from Presto. They include their velocities, radii, and displacements along with a sample rate giving the state of the calculation at different times. The specification for this data is given in the Presto input deck as:

```
begin results output results1
  database name = exodus/sprayFuego.e
  at time 0.0 increment = 1.0e-8
  nodal variables = force_external as f_ext
  nodal variables = velocity as vel
  nodal variables = displacement as displ
  element variables = von_mises as vonmises
  element variables = eqps
  element variables = death_status
  element variables = sph_radius
  global variables = timestep
  include = block2_particles s
  exclude = block2
end results output results1
```

As the particles dispersed, they would contact the sides of the container and other particles, until ultimately ejecting upward. The simulation was continued until the total kinetic energy of all the particles reached their asymptotic peak. Beyond this point, the particles were handed off to Fuego to continue the calculation.

There were a total of three different Presto runs to provide the dispersal of particles for the Fuego simulations. The initial run is used to demonstrate that coupling of the Presto to the Fuego simulations can be done. Because the particle size in the first run is on the order of millimeters, the second run containing micron sized particles was needed to match the real life case of respirable particles. However, using only the micron sized particles did not sufficiently inject enough energy into the fluid such that these particles would deposit onto surroundings beyond the container; therefore, a combination of different particle sizes is needed, which is given in the final run. The following three subsections describe the initial run, second run and final run of the Presto simulations.

5.2.2.1.1 Initial Run

The initial simulations tested the feasibility of using Presto. The mesh was coarse with the powder and container regions having only 465 and 596 elements respectively.

For the pressure load, the Presto input deck has the setting:

```
begin initial condition
```

```

block = block_2
initialize variable name = unrotated_stress
variable type = element
magnitude = -1.72e9 -1.72e9 -1.72e9 0.0 0.0 0.0
end

```

where block 2 is the part of the mesh containing the particles. The magnitude of $-1.72e9$ Pa is 1000 times higher than 250 psi (1.72369 MPa). The reason the magnitude of the stress is so much higher is because there is no gas model which could be used as the explosion mechanism. Such a gas could focus the energy such that the powder would be directed out of the container. There are shock and gas models in Presto, but most are ITAR and would limit the reproducibility of the simulations.

These particles were created using the SPH feature in SM which creates particles from a finite element mesh. The initial calculations used coarse meshes with a powder region entirely filling a container having a radius of .0596 m and a height of 0.1053 m. Each of the 465 elements of the powder mesh was converted into 5 particles resulting in a total of 2325 particles. The input deck has the following element to particle conversion block:

```

begin element death gas_death
block = block_2
death start time = 0.0
criterion is always true
begin particle conversion
particle section = sph
max num particles = 5
end particle conversion
end element death gas_death

```

and the SPH particles themselves are set with:

```

begin particle section sph
radius mesh variable = attribute
problem dimension = 3
recalculate radius = off
recalculate volume = off
final radius multiplication factor = 1.0
constant sphere radius
FORMULATION = SPH
end particle section sph

```

Figure 5-18 shows the mesh and the particles at the end of the calculation. The radii of the particles ranged from 4.43 to 6.28 mm. When the results of this Presto calculation were continued in Fuego, it was found that the particle sizes were too large and did not deposit on the surfaces of the enclosure representing the room. The particles needed to be micron sized for this to happen.

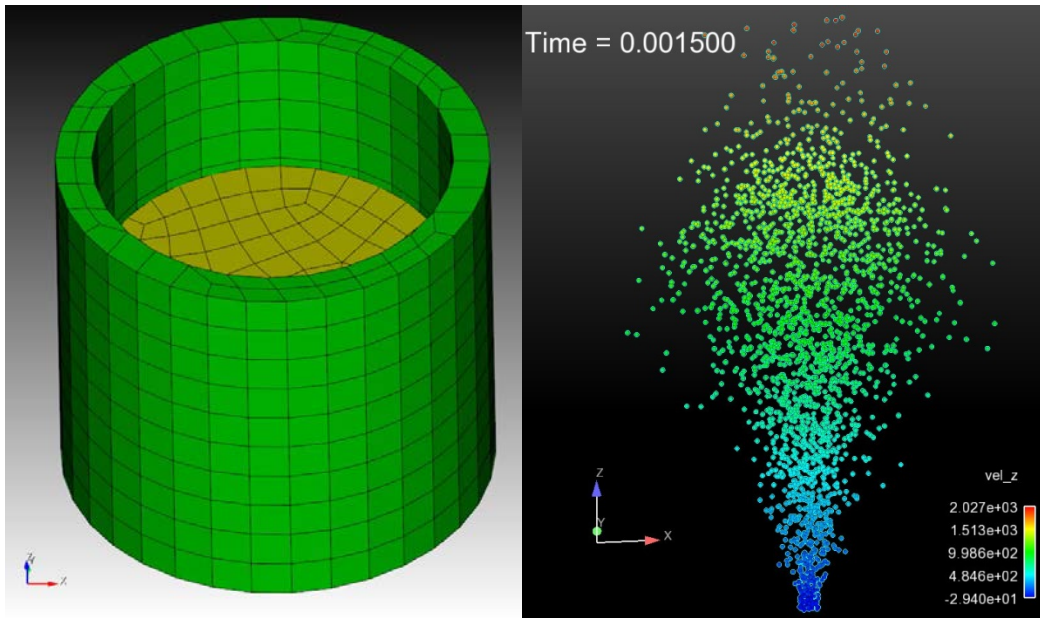


Figure 5-18 Mesh and Calculation Results for Initial Run. Mesh of Powder and container (left), Final State of Particles velocity z in color (right).

5.2.2.1.2 Second Run

In this run, the particle radii were on the order of microns. There were more than 102782 particles. The mesh refinement was such that only one particle was derived from each element rather than 5. With the smaller size, the powder region was made smaller as well to limit the number of particles to about 100000.

The radius of the container was reduced in size to $3.0e-04$ m with a height of $4e-04$ m so that it completely surrounds the powder, forcing the particles to disperse upward as in the initial run. See Figure 5-19 for the mesh and final state of the particles.

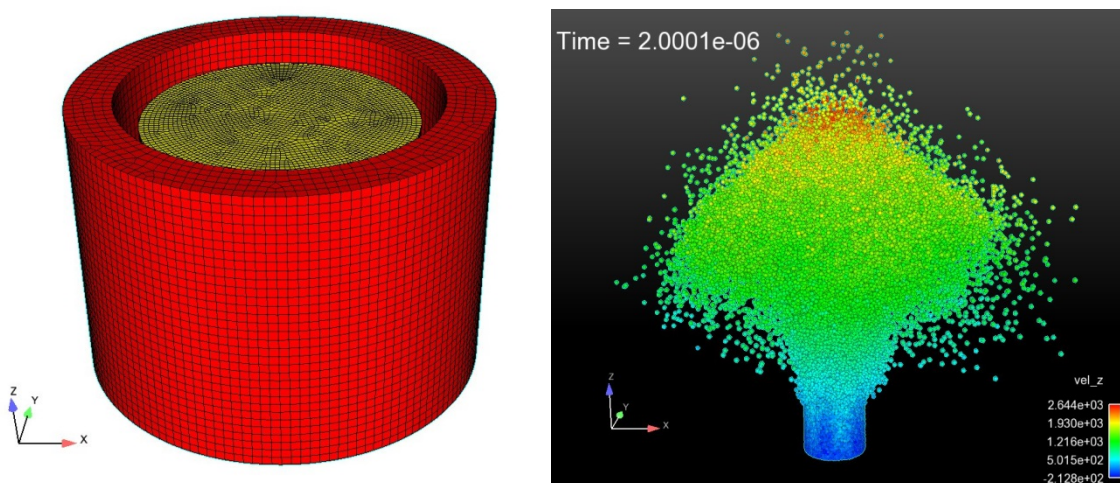


Figure 5-19 Mesh and Calculation Results for 2nd Run. Mesh of Powder and container (left), Final State of Particles velocity z in color (right).

When these particles were imported to the Fuego part of the calculation, it was found that they did not go much farther beyond their location given in Figure 5-19 (right). The reason is that these small particles had very low kinetic energies, which their movement was quickly damped by the fluid. So what is needed is a combination of micron-sized particles and larger-sized particles.

5.2.2.1.3 Final Run

A lot of experimentation was made to find a distribution of particles which would cause some to deposit on the walls of the room. It was not possible to simply include the larger sized particles of the first run along with the smaller ones in the second because having such extremes in particle sizes causes the calculation to dramatically take longer to complete. So the larger particles added could not be more than 2 orders of magnitude bigger than the micron particles. But they had to be large enough to impact the fluid of the Fuego calculation such that the micron-sized particles would be lofted into depositing on the walls.

For the final distribution of particle sizes, the mesh contained 3 cylinders having different levels of element refinement (See Figure 5-20). Each element was then converted into a single particle as in the second run. These particles had radii ranging from 4.847 to 87.85 microns. The 3 mesh regions had, from finest to coarsest, 103671, 4040, and 2754 elements for a total of 109007.

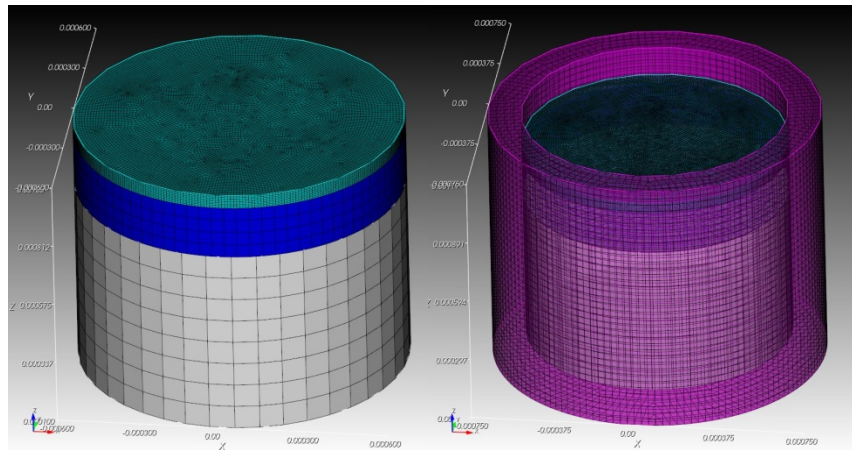


Figure 5-20 Finite Element Mesh for Final Run. Mesh of 3 Powder Region Sizes (left), Mesh of powder region surrounded by container (right).

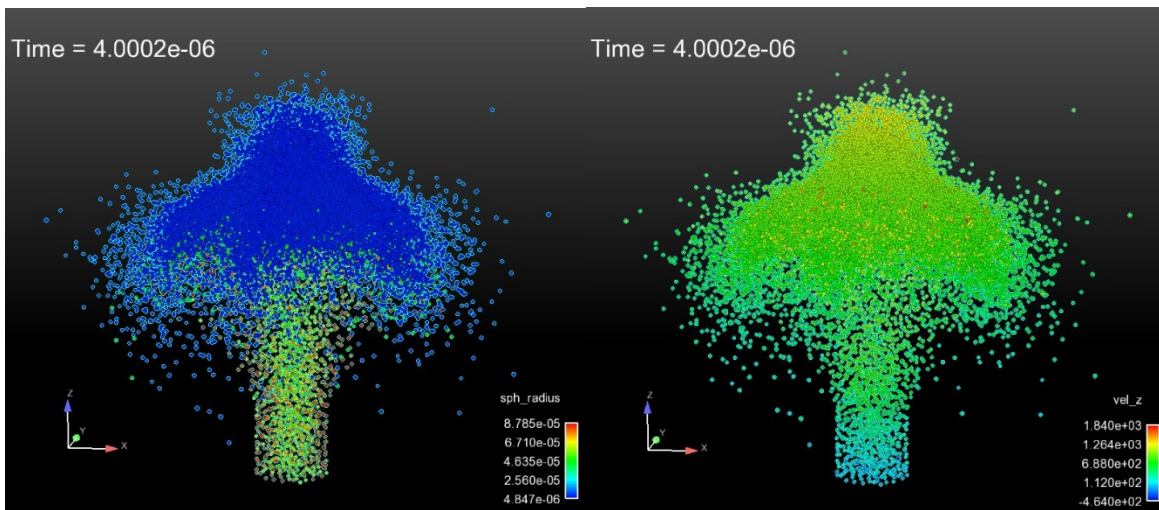
Table 5-10 shows a comparison of the different runs in terms of particle sizes and number of particles. One additional point to add is that the initial hydrostatic stress in the final run is half of what was used in the initial run. This created enough energy to cause deposition.

Table 5-10 Comparison of Particle Sizes and Number of Elements for All Runs

Initial Run Coarse Mesh	Second Run Fine Mesh	Final Run 3 regions of refinement
Particle Radii: 4.43 to 6.28 mm	Particle Radii: 7.091 to 13.07 microns	Coarse region Particle Radii:

Number of Particles: 2325	Number of Particles: 102782	49.6 to 87.85 microns Number of Particles: 2754
		Semi-coarse region Particle Radii: 28.54 to 53.32 microns Number of Particles: 4040
		Fine region Particle Radii: 4.8475 to 11.092 microns Number of Particles: 103671

Figure 5-21 shows the final state of the ejected particles at the end of the Presto calculation. The simulation was run with 128 processors and took 1.5 hours. Figure 5-22 shows a plot of the kinetic energy vs. “time of all the particles.”



a) Particle Radii in Color b) Particle Velocity z in Color

Figure 5-21 Final State of Particles at end of Presto Calculation.

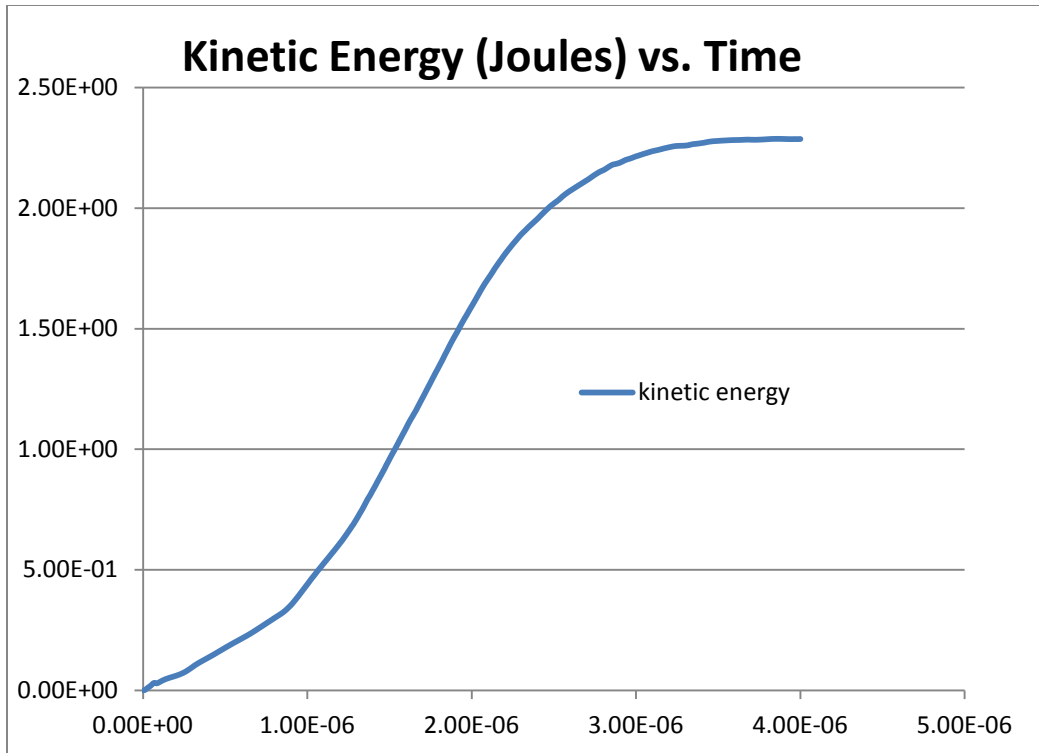


Figure 5-22 Kinetic Energy of All Particles vs. Time.

5.2.2.2 Translation from Presto Results to Fuego Inputs

In order for Fuego to utilize the particle output from Presto, a translation method was used to generate a series of particle files to be read by Fuego. The particle files were generated using a series of scripts designed to extract the Presto outputs.

The Fuego particle files require tab delimited data in the following format:

```

3
2.36e-04 1.44e-04 1.03e-03 -7.11e+01 -5.74e+01 4.36e+02 7.17e-06
-2.06e-04 1.78e-05 1.05e-03 2.43e+01 -8.90e+00 6.74e+02 5.95e-06
-2.13e-04 2.13e-05 1.05e-03 -1.36e+01 1.64e+00 6.97e+02 5.92e-06

```

The first line contains the total number of particles in the file. Each of the following lines corresponds to a single particle and contains information for the x, y, z particle positions, x, y, z velocities, and the particle diameter, which are given in the seven column data.

The Presto exodus output file contains one or more particle blocks. For particle translations, each of the particle blocks have to be separated into its own exodus file and treated separately. The SEACAS tool Ejoin was used in order to split the Presto output into a series of exodus files, one for each sampled time step. A script written by Alexander Brown, prestulcan_convert.exe, was used to extract the particle data corresponding to the seven required columns for particle file inputs for Fuego. The sequent particle files are created according to the time point in the Presto

simulation. The translation will produce the same number of particle files and the corresponding time points being extracted from the Presto simulation.

A second script, `prestulcan_multifile_input.exe`, was used to create the seven column data file format (as described previously) for Fuego to process, except to extract out certain time points for Fuego to use which is described as follows. Note that these final files contain the particles that are to be injected into the Fuego simulation at a given time based on the criteria described below. The files are populated with a particle when the particle first achieves a specified dimensionless separation distance, B . B is defined as the center to center particle distance divided by the particle diameter. For the described 250 psig cases, the value of B used is 1.3. Once a particle reaches the specified B value, it is placed in a single `particles.txt` file and is removed from particle files for future times. The sum of the first lines in the N final particle files is equal to the number of total particles from the Presto simulation.

5.2.2.3 Fuego Simulation

The particle files created in the translation step previously described create particles at specified times in the Fuego simulation. The particle creation step uses Fuego's create particle input block that has the following format:

```
BEGIN CREATE PARTICLES FROM FILE myFileBlock1
    PARTICLE DEFINITION = solid_particles1
    CREATION_TIME = 0.00000001
    LENGTH_SCALE_FACTOR = 1.0
    FILENAME = PART/particles1.txt
    NUMBER REPRESENTED = 100
    TEMPERATURE = 305.0
END    CREATE PARTICLES FROM FILE myFileBlock1
```

The total number of particles created by a single “create particles” block is the number of particles specified in the particle file multiplied by the number represented. For the following Fuego cases described, Number Represented = 1 was used for Case 1 and 2. Number Represented for Case 3 and 4 was set as described in the tables corresponding to those sections (see Table 5-12). A create particles block is needed for every resulting populated particles file from the Presto translation.

The coupling mechanism between Presto and Fuego is complicated by the fact that during particle injection into Fuego from Presto, the particles and their surrounding fluid do not have the same velocity. During the first particle injection into Fuego, the particles are instantly released with velocities on the order of 10^3 m/s into a still fluid. The drag force acting on the particles and the exchange of momentum imparts velocity to the still air. This situation is not physical as the fluid and the particles should be moving with some velocities (accounting for the slip phenomena) during the initial burst from the particle beaker. The coupling between Fuego and Presto as a result will require some additional iterations to be able to fully account for this effect.

Four separate Fuego calculations were performed using different sets of particle files from the translations from Presto to demonstrate the process of the Presto/Fuego coupling with the 250 psig case.

The turbulence parameters from the 250 psig experiment helped to assess the quality of the results of the Presto/Fuego coupling, and is shown in Table 5-11.

Table 5-11 250 psig Experiment Turbulence Parameters

Parameter	RART Case 3: Initial Burst	RART Case 3: Aerosol Impact at Top Wall
X _{char} , m	9.53e-2	2.9
U _{char} , m/s	1.61e3	7.19
Ma	4.6	0.021
Re	1.64e+008	1.32e+006
Wall friction velocity, m/s	4.77e+001	3.04e-001
y(y ⁺ =1), m	1.96e-008	5.20e-005
Ratio of turb. visc. vs. viscosity	2.11e+005	3.11e+003
Turbulence intensity	1.50e-002	2.75e-002
Specific turb. kinetic energy, m ² /s ²	8.80e+002	5.85e-002
Eddy dissipation, m ² /s ³	3.52e+005	6.28e-003
Integral eddy size, m	6.67e-003	2.03e-001
Taylor eddy size, m	1.53e-004	3.84e-002
Kolmogorov eddy size, m	1.24e-006	8.90e-004

5.2.2.3.1 Case 1: Coarse Particles

The first Fuego simulation used large, coarse particles with sizes on the order of millimeters. These particles were translated from the coarse mesh Presto simulation described previously.

The Fuego simulation used 1951 total particles with a mean diameter of 7.2 mm. The particles were released with large initial particle velocities (maximum velocity 1823 m/s) that are similar to the experimental initial burst velocity (see Figure 5-23). The maximum fluid velocity reached was 408 m/s. Due to the relatively large size and mass of the particles (average particle mass 8.61e-4 kg), all particles that escaped the beaker were deposited in 0.2 seconds, as shown by the figure below. At 200 seconds, 96.3% of the particles had been deposited and 8.05% of the particles had been deposited on the filters.

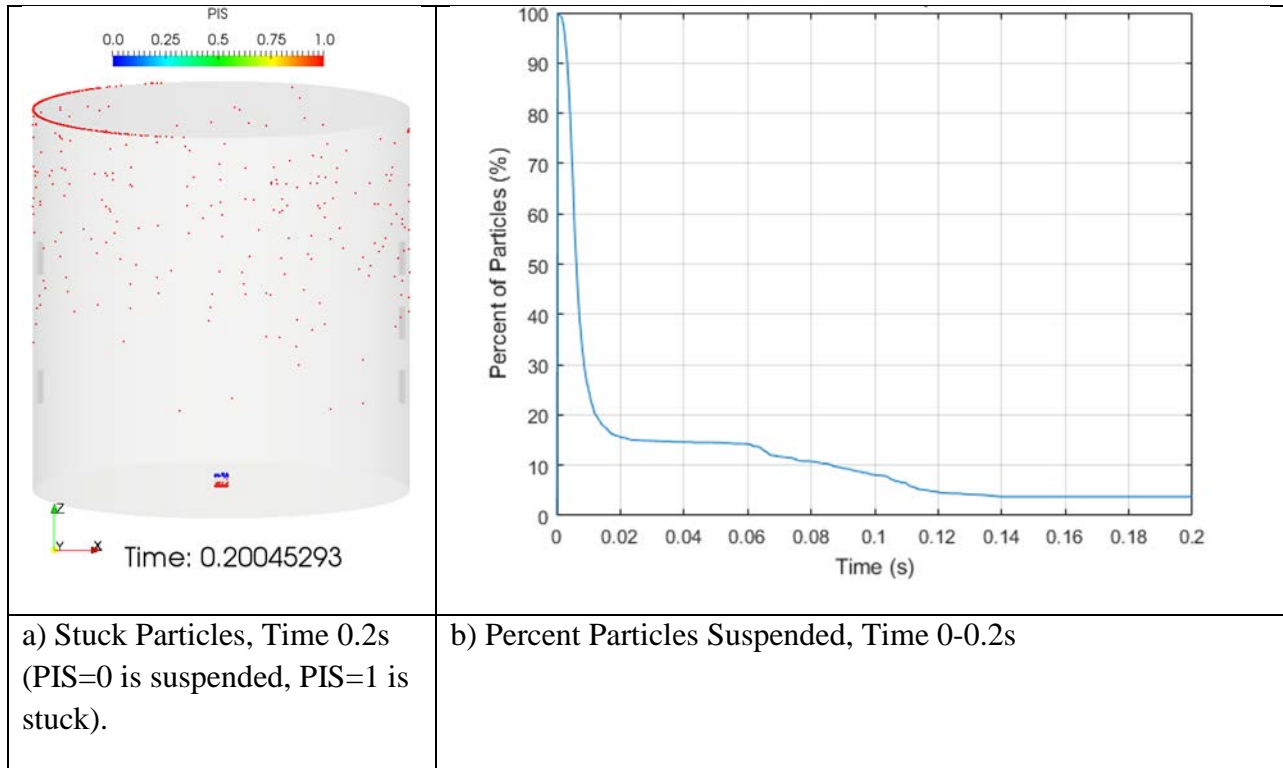


Figure 5-23 Case 1 Fuego Simulation.

5.2.2.3.2 Case 2: Fine Particles

The second Fuego simulation used 102,914 fine particles, with a mean diameter of 10 microns. These particles were translated from the fine meshed Presto simulation described previously.

As shown in Figure 5-24, the particles were injected into the Fuego simulation with velocity magnitudes of 10^3 m/s (maximum 3388 m/s), but their mass (average particle mass 2.20×10^{-12} kg) and momentum were too small to allow individual particles to move into the outer reaches of the cylinder when injected into still air.

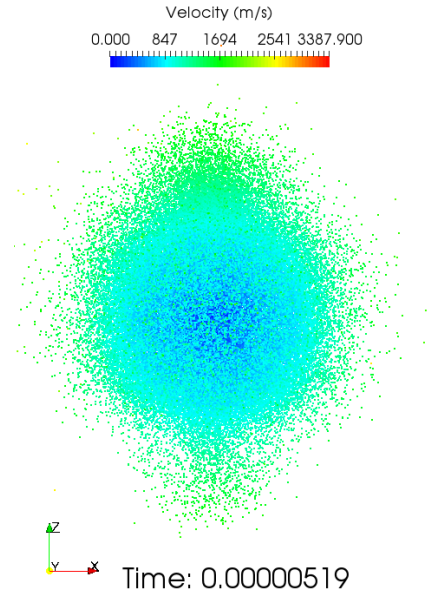


Figure 5-24 Case 2 particle velocities during initial burst into Fuego simulation, before momentum exchange and drag forces slow the particles.

The maximum fluid velocity reached was 1.78 m/s, which was much lower than the maximum reached in the previous Fuego simulation (408 m/s). At the end of a 1-second simulation, 62.6% of the particles had been deposited. 37.4% of the particles remained suspended and their total combined kinetic energy was 1.17e-11 J. None of the particles deposited on the filters.

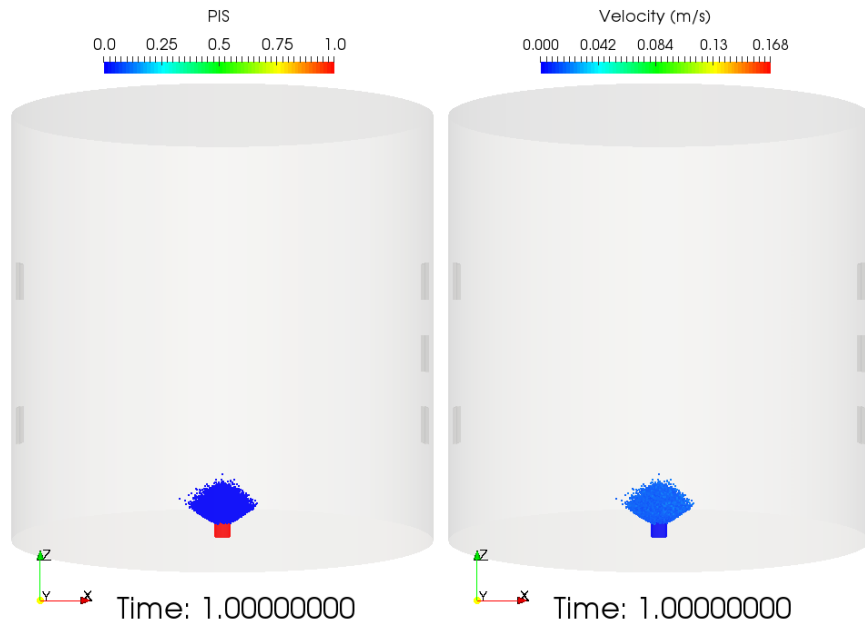


Figure 5-25 Case 2 stuck particles (PIS=0 is suspended, PIS=1 is stuck) and velocities at 1.0s.

5.2.2.3.3 Case 3: Multi-sized Particles

The third simulation used a combination of fine and coarse particles. Three sets of particles were translated from the Presto output to the create particle blocks in Fuego. A summary of their sizes and number of particles is shown in Table 5-12:

Table 5-12 Particle Block Parameters for Fuego

Particle Block	Mean Particle Diameter	Number Particles Contained in particles.txt files	Number Particles Represented	Total Number of Particles (Fuego)
1	8.13e-06 m	103,671	1000	103,671,000
2	4.03e-05 m	3064	100	306,400
3	6.78e-05 m	2272	100	227,200

Particle Block 1 contains fine particles that were lofted into the air by their initial velocities and the positive z fluid velocity induced by larger particles from Blocks 2 and 3. The maximum particle velocity at injection was 1550 m/s, which is on the same order of magnitude as the 250 psig experiment. The maximum fluid velocity was 582 m/s. The initial burst of the larger particles from Blocks 2 and 3 helped to negate the effect seen in the Case 2 simulation where the fine particles were effectively stopped in place by their injection into still air.

Simulation frames taken at different times show that the particles contained in the three blocks behave differently after injection. The large Block 3 particles impact the ceiling within 0.6 seconds of injection. Particles from Block 2 do not reach far enough up in RART before falling to the floor. The fine particles from Block 1 have a smaller initial velocity and move together as a cluster before striking the top of the cylinder with an average particle velocity of 1.12 m/s and a maximum fluid velocity of 3.43 m/s at impact. This velocity is similar to the experimental velocity at the time of impact and is on the correct order of magnitude. The fine particles then moved from the center and across the ceiling of the container toward the walls.

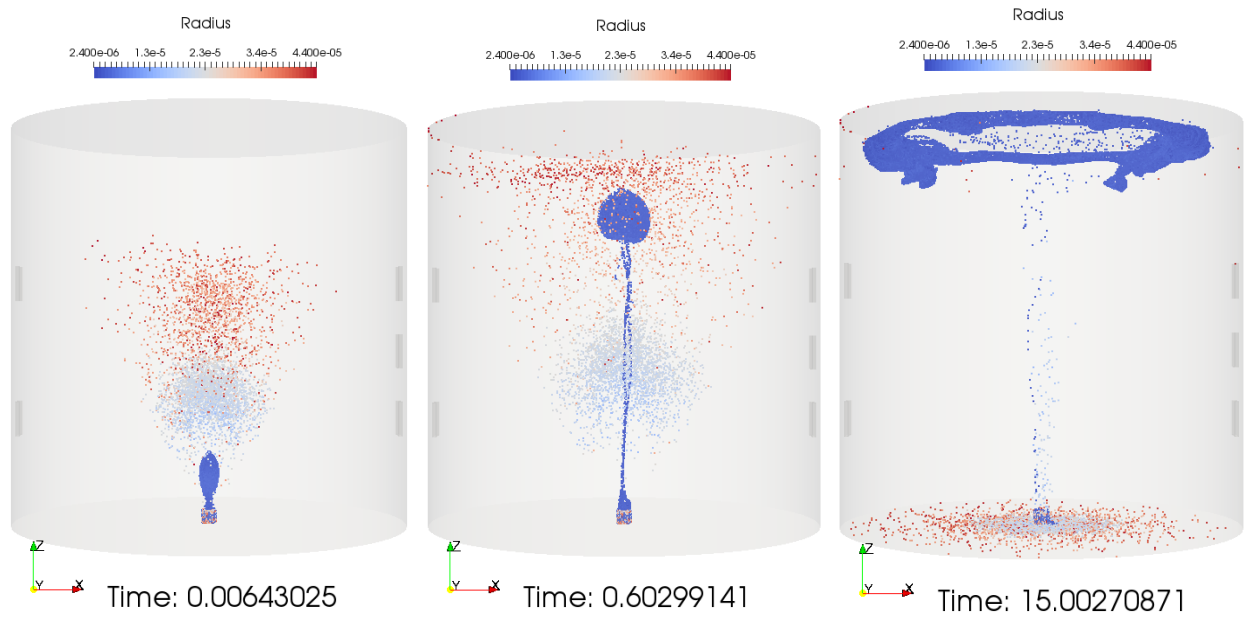


Figure 5-26 Case 3 particles showing the different sizes of particles at different times after injections.

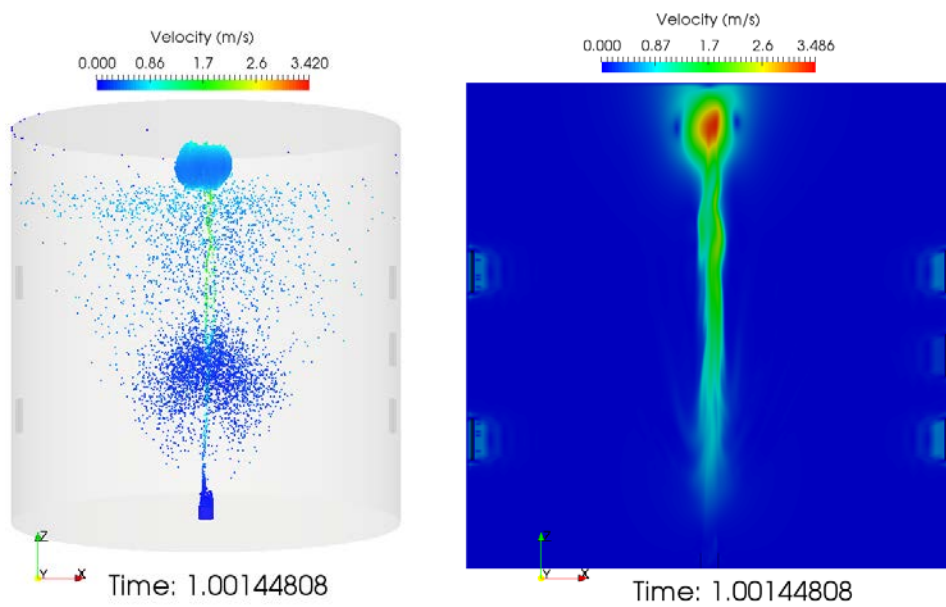
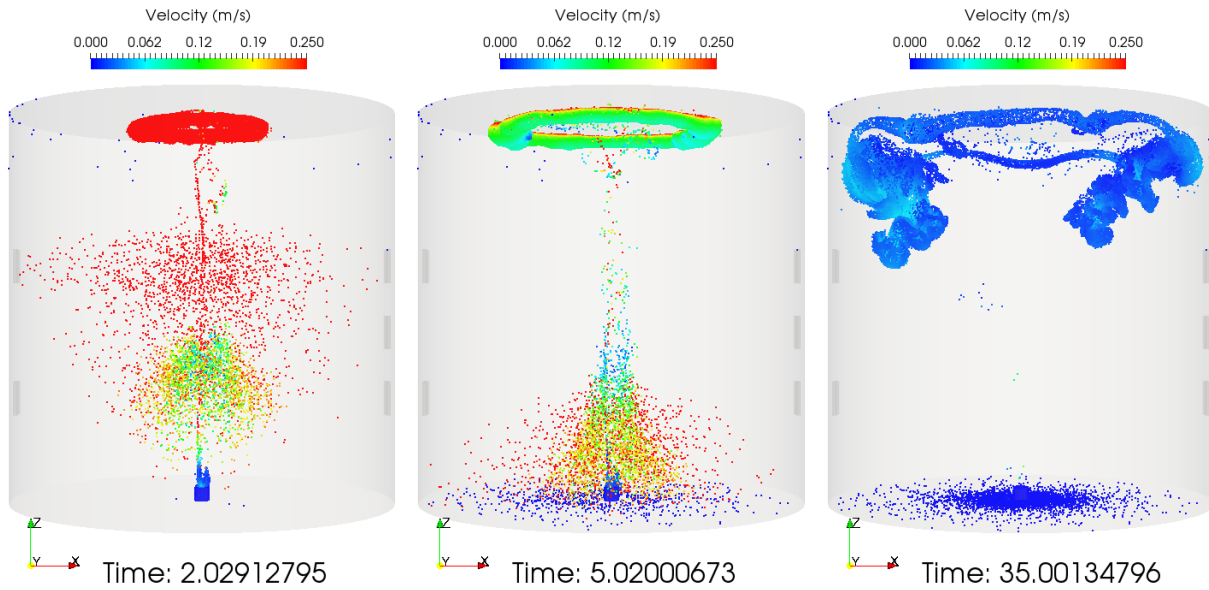
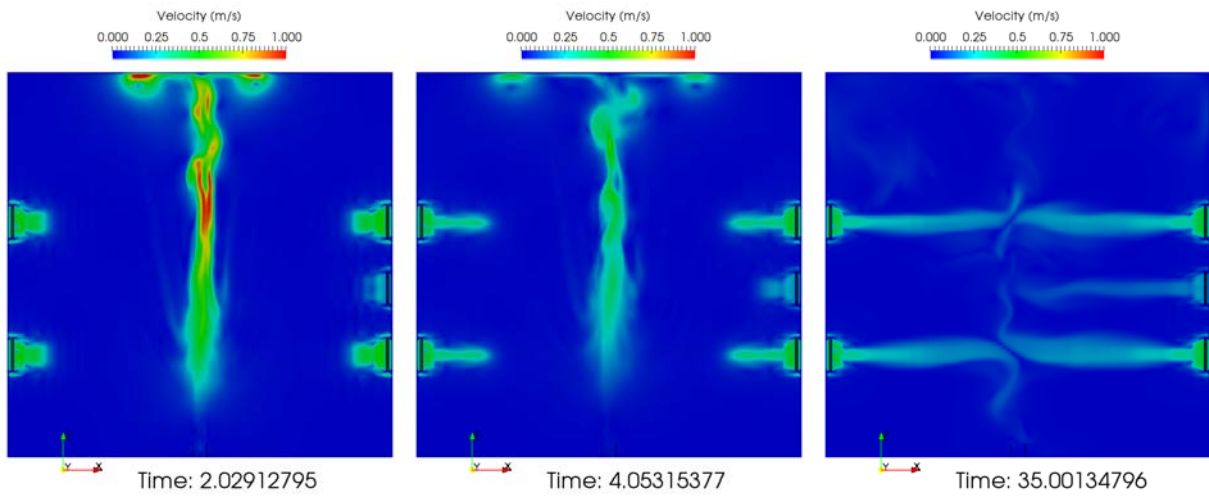


Figure 5-27 Case 3 particle and fluid velocities at impact with the ceiling of canister.



a) Case 3 Particle Velocities.



b) Case 3 Fluid Velocity.

Figure 5-28 Case 3 particle and fluids velocities after impact with the ceiling.

At the end of 200 seconds, 52.0% of the particles remain suspended. 46.9% of the total particles deposited and 1.12% of the particles deposited on the filters.

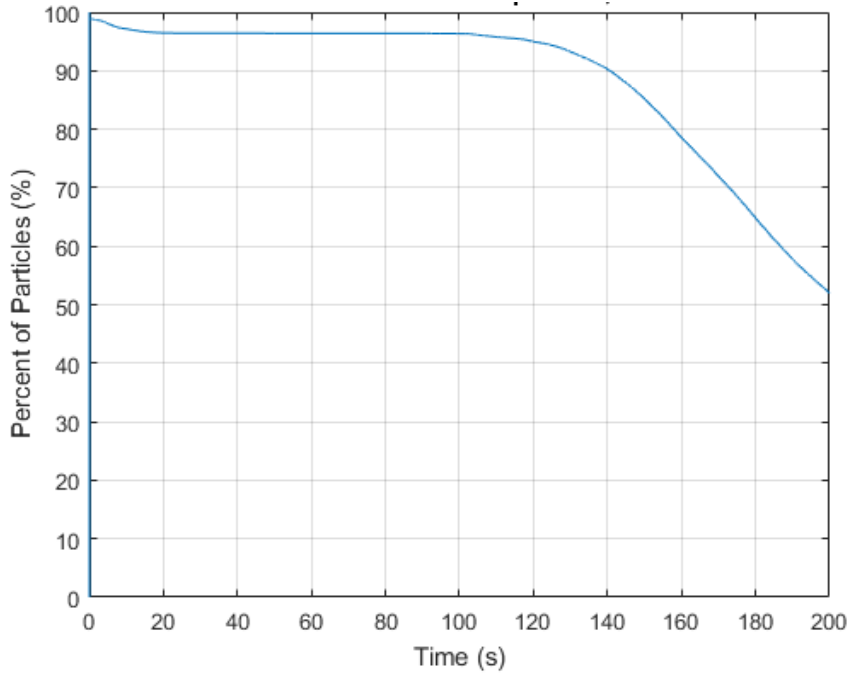


Figure 5-12 Case 3 Percent Particles Suspended, Time 0-200s.

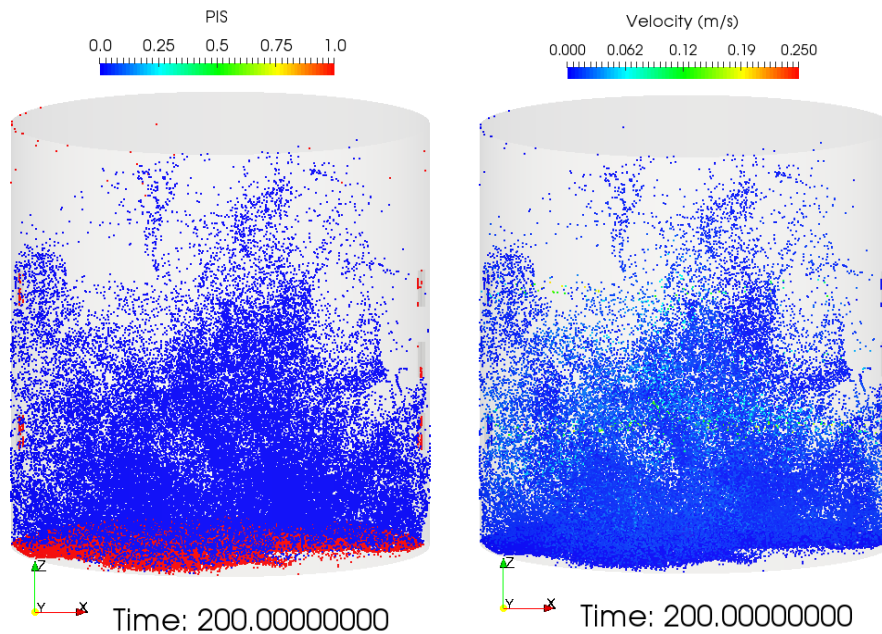


Figure 5-29 Case 3 stuck particles (PIS=0 is suspended, PIS=1 is stuck) and velocities at time 200s.

5.2.2.3.4 Case 4: Multi-sized Particles, Middle Section Open

An additional fourth simulation was performed using the same injected particles as in the Case 3 Multi-Sized Particles section. In the Fuego input, the ceiling boundary condition was changed from completely closed to having the middle ring open. Otherwise the Fuego input was identical to that of the third simulation.

The particles initially behave as they did in the previous simulation. They have the same maximum initial velocity of 1550 m/s and maximum fluid velocity 582 m/s. The fine group of particles hit the ceiling with an average velocity of 1.12 m/s. The maximum fluid velocity at this time was 3.49 m/s.

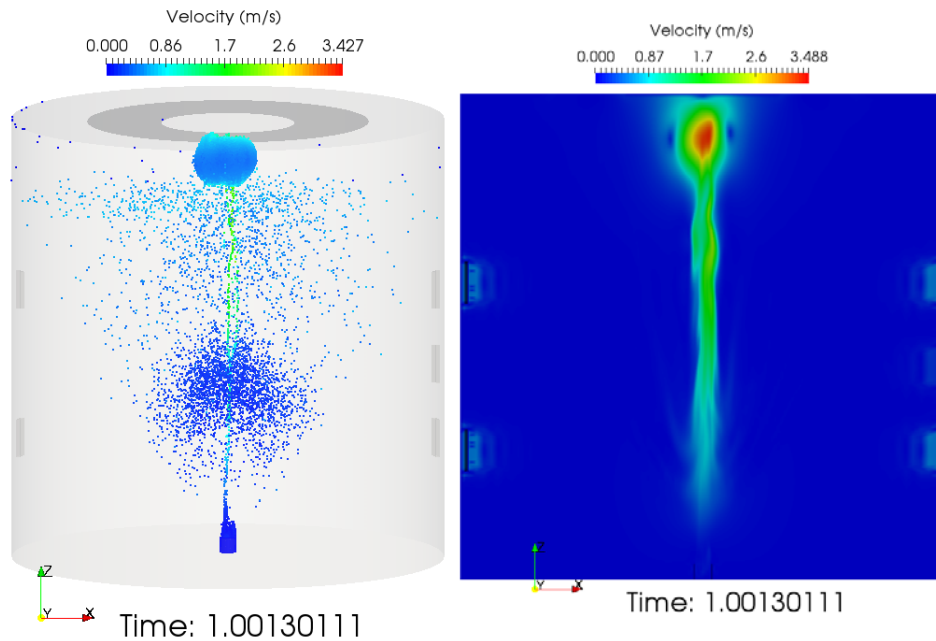
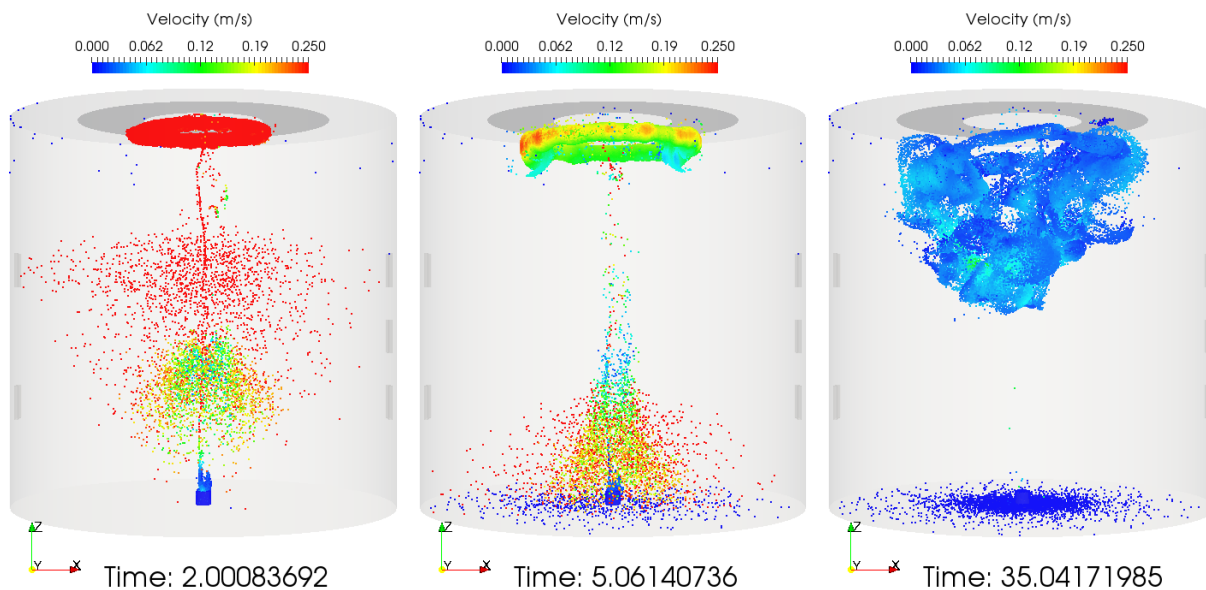
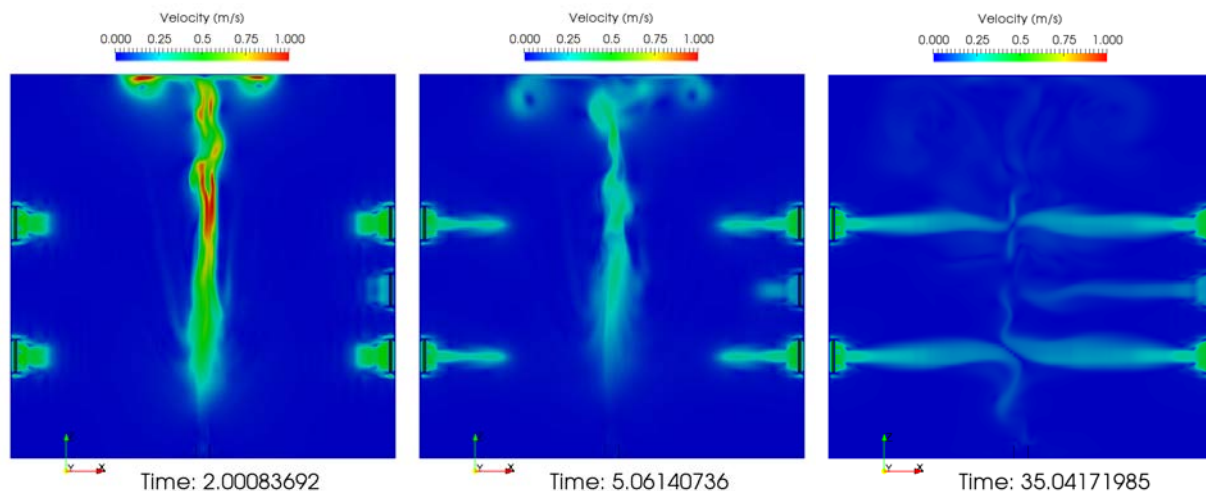


Figure 5-30 Case 4 particle and fluid velocities at impact with the ceiling of canister.

The resulting ring of particles spreads outward from the center and toward the open middle ring of the ceiling. Upon encountering the open middle ring, the particles are directed downward and do not spread horizontally to the outer ring of the ceiling. This may be an effect of the turbulence mode. Because of their relatively high velocities, few particles are deposited on the ceiling itself.



a) Case 4 Particle Velocities.



b) Case 4 Fluid Velocity.

Figure 5-31 Case 4 particle and fluids velocities after impact with the ceiling.

At time 200 seconds, 143,000 particles had been deposited on the middle ring of the ceiling, which accounted for 0.14% of the particles in the simulation and 0.40% of the total stuck particles. 65.8% of total particles remained suspended, 34.9% were deposited, and 0.22% of the total particles deposited on the filters. This is a smaller amount of deposited particles than in the closed ceiling case. It is hard to draw conclusions from this case and the number of particles

deposited on the open middle section due to behavior of the particles as a result of the high particle velocities as they impact the inner ceiling. The particle and fluid velocities are similar to those measured during the experiment during impact, but some work still needs to be done in order to lessen the effects of the Presto/Fuego coupling's abrupt particle injection into still air.

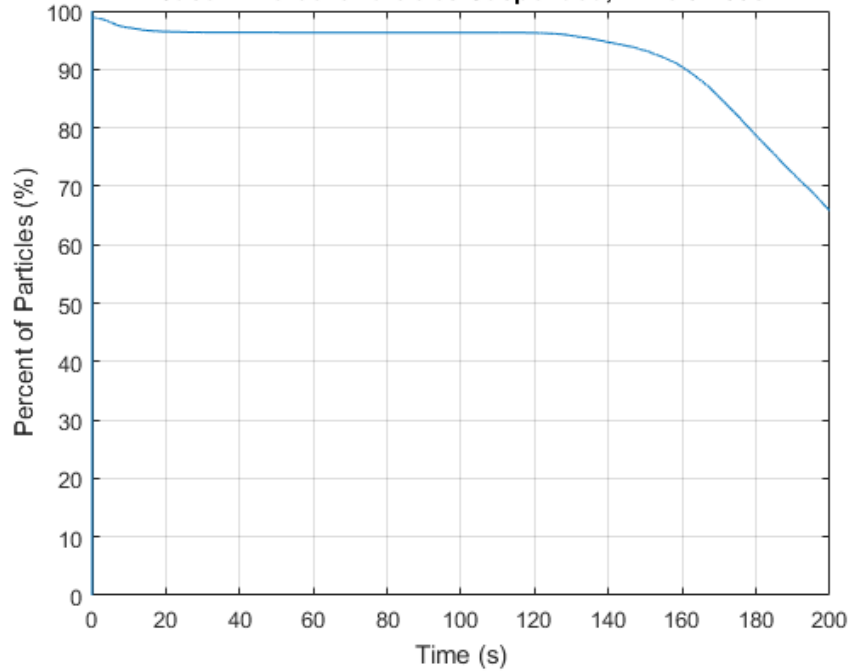


Figure 5-32 Case 4 Percent Particles Suspended, Time 0-0.2s

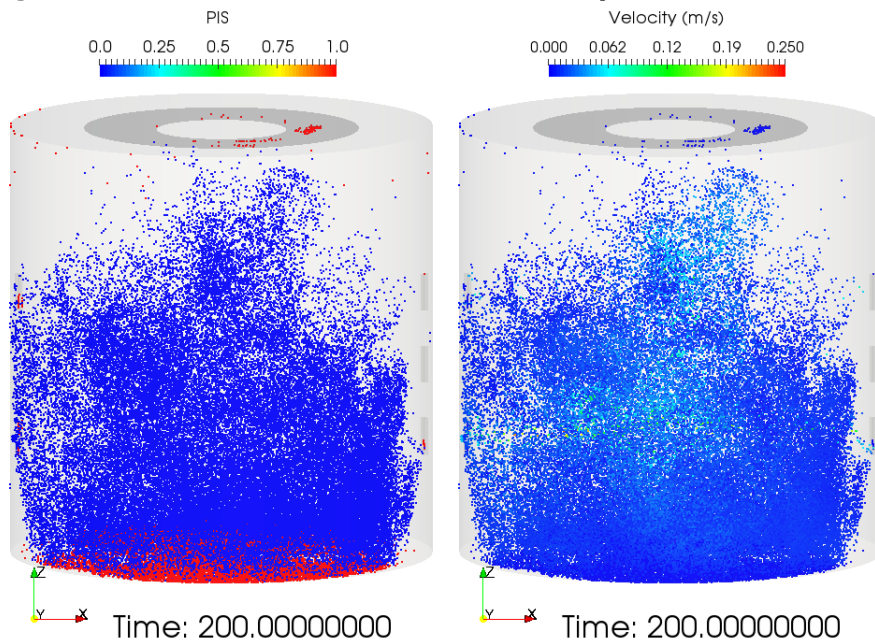


Figure 5-33 Case 4 stuck particles (PIS=0 is suspended, PIS=1 is stuck) and velocities at time 200s.

5.3 Summaries and Conclusions

This chapter describes three simulations conducted for the free-fall spills, 50 psig (0.34 MPa) and 250 psig (1.72 MPa) pressurized powder release cases in the experiments conducted in RART.

A gravitational (free-fall) spill simulation of 100 g of TiO₂ powder in a beaker has been done, even though 10⁸ out of 10¹³ of the particles in 100 g were used. We have used a fine mesh for this simulation, which is a significant improvement over that of Year 1. We model both the prescribed sample flow and introduce a turbulence model, an improvement over Year 1. When the beaker is turned, the fall of powders will interact the air around them, and introduce the fluid motion within the RART volume. The induced fluid velocity can be used by MELCOR [Louie 2016]. We were able to run the simulation to the experiment end time of 30 minutes.

However, the aerosol result of the simulation overestimates the ARF in terms of the particles collected in the samples. This difference may be due to the following factors:

- Fuego currently does not model agglomeration, which may cause the faster settling.
- The assumption of 10⁸ (10⁵ with 1000 particles per parcel) particles in the model versus the actual number of particles of 10¹³ may overestimate the number of particles pulled through the samples.
- The turbulence flow model used may influence the mixing that causes the overestimation.
- The percent of particle collected is a number percent, which may be different from the experimental data as a mass percent.

In the pressurized release experiments, PARE apparatus is used to release the powder in the RART. We conducted both 50 psig (0.34 MPa) and 250 psig (1.72 MPa) cases. Because Fuego is a low-Mach (< 0.7) fluid code, we can only model the 50 psig (0.34 MPa) case (Mach number is about 0.38). For the higher pressure case, we use SIERRA/SM (Presto) code to perform the initial blast of the powder and pass the particle data to Fuego for simulating the rest of the experiment condition.

50 psig (0.34 MPa) Case

For this pressure case, the simulation of the rupture disk in the experiment for the pressure release from the PARE to RART was assumed to be open within ~ 1 millisecond. The fluid velocity of 643 m/s was assumed for this pressure case. The results show that the particle cloud rises up toward the ceiling of RART in a short time, while the sampling (or filters) flow pulls the particles toward the sampling devices. As the simulation continues, particles that impact the ceiling or hit the PART walls will stick or deposit. Because of the difficulties observing any deposition, additional simulation runs with fluid open boundary conditions were used to allow depositions. These types of open boundary conditions would be corrected if they were modeling

the filters, since particles are trapped onto the filter while gas is allowed to flow through. Despite this issue, the deposition values are reported for both the ceiling and filters.

250 psig (1.72 MPa) Case

For this pressure case, the simulation of the powder release of 250 psig (1.72 MPa) was first done through the use of the Presto code. Initially, a coarse mesh was used to model the TiO₂ powder by using the SPH model in the PARE with the prescribed pressure as the induced pressure (or stress) load. However, the size of this stress is insufficient to induce the release of the powder. Therefore, this stress is increased by a factor of 1000. This increase in value is justified because Presto primarily models solids, and it does not model fluid, even though there is an ideal gas model (only in the ITAR version). To truly model gases, a fluid code like Fuego is required. In reality, when the PARE is pressurized, both powder and air inside the PARE are at pressure. Without modeling the gas portion, the induced stress needs to be larger in order to push the particles out of the PARE volume. When passing the particles to Fuego, the induced fluid flow by the injecting particles may not yield the actual fluid conditions as in the experiment. That is why the use of the multiplier is justified.

At first, we wanted to demonstrate if this Presto-Fuego coupling calculation was feasible. To do that, a coarse model having millimeter-sized particles was initially used. In order for Fuego to utilize the particle output from Presto, a translation method was used to generate a series of particle files to be read by Fuego. The particle files are generated using a series of scripts designed to extract the Presto outputs. Once it is done, the Fuego simulations were conducted.

In the first run, the coarse particle sizes in the order of millimeters from the Presto run were input to Fuego run. The Fuego model was based on the “no flow” case for the 50 psig (0.34 MPa) simulation described in Table 5-9. In this case, the Fuego run showed that the particles were stuck to the surfaces early. It may be because the particles are too large. In the fine particle size run (using the results of Presto in the second run), the Fuego results showed that the particles were very slow because the micron sized particles could not influence the fluid in the RART volume. Therefore, the multi-size particle run by using final run of Presto simulations was conducted. In this simulation, the results are more encouraging. Because the particles imparting the ceiling were not able to stick to the surfaces as indicated in the experiment, a separate Fuego model (using the “middle” case in Table 5-9 for the 50 psig case) was conducted. However, the results showed slightly improved deposition onto the middle ring of the RART ceiling in comparison to what was observed in the same case for the 50 psig (0.34 MPa) simulation. This may be because the selection of the turbulence model chosen or other effect associated with the boundary layer. Thus iterations may be required to model the condition of the experiment correctly. As indicated in Chapter 2, the deposition model in Fuego can be improved. This improvement may be suitable for this simulation. All Fuego simulations were only run out to 200 seconds, instead of 30 minutes as reported in the experiment.

This Page Intentionally Left Blank

6 FRAGMENTATION ANALYSIS

6.1 Introduction

Glass and ceramic-oxide radioactive material forms (e.g., PuO₂) are susceptible to brittle fracture during handling and transportation. Fracture of these materials may result in the generation of fragments small enough to become airborne, and thus easily dispersed and inhaled. Entrainment and dispersal of particles with aerodynamic equivalent diameter (AED) of 10 μm or less is generally anticipated under normal aerodynamic conditions [DOE 1994, Haschke 2008]. The assessment of the risk to the public and the environment from these materials due to events resulting in their fracture is based on the determination of the source term for environmental release. This source term is typically quantified by an airborne release fraction (ARF) and a respirable fraction (RF) of material generated by a given event [DOE 1994].

Section 4.3.3 of DOE-HDBK-3010 (the DOE Handbook [DOE 1994]) provides an empirically based formula for determining the airborne respirable fraction of material (ARF x RF) generated during a free-fall impact scenario. While this equation is generally considered conservative and satisfactory for assessing compliance with the regulatory process for handling and transportation of these materials, it is based on data derived from free-fall impact tests performed by Mecham et al. [Mecham 1981] and Jardine et al. [Jardine 1982] in which only a few materials, subjected to a limited range of loading conditions, were considered. Because the final state of fragmentation (in terms of the size and distribution of fragments) is strongly dependent not only on the properties of the material and the energetic loading conditions that lead to breakup, but also on the different intrinsic length scales associated with fragmentation, it is difficult to precisely predict fragmentation characteristics for other brittle solid wastes forms subjected to a wider range of loading conditions based on the test data alone. Numerical simulation techniques have the potential to allow such predictions.

This chapter describes a two-scale modeling approach, in development by us, that may be used to simulate the dynamic fragmentation of brittle solid radioactive material forms subjected to general loading and boundary conditions. The approach is intended to provide the necessary level of accuracy, fidelity, and versatility for making safety assessments of brittle radioactive materials subjected to wide-ranging accident conditions, while remaining computationally tractable. The method provides the resulting fragment characteristics (average size and size distribution) across the entire fragment range of interest.

A preliminary version of this two-scale modeling approach has been exercised on a representative problem drawn from the laboratory-scale impact tests that form the basis of the ARF x RF equation provided in the DOE Handbook for the free fall spill and impactation stress release case. Results from this exercise are described below. This demonstration is an initial step in the development of a more sophisticated approach that will take the form of a constitutive model to be incorporated in SIERRA/SM finite element code during the third year of this project.

6.2 Two-Scale Model Approach

The two-scale modeling approach uses the finite element method to simulate dynamic fracture under general loading and boundary conditions to determine macro-scale fragmentation. At the

lower length scale, a one-dimensional (1-D) model is used to determine the micro-scale fragmentation. Boundary conditions for the 1-D model are derived from the macro-scale model. Fragmentation characteristics from both length scale models are combined to determine the resulting fragment size distribution spanning both length scales.

6.2.1 Macro-scale

At the macro-scale, the approach uses a gradient damage elastic continuum mechanics material model within a finite element framework to simulate dynamic fracture under general loading and boundary conditions. SIERRA Solid Mechanics (SIERRA/SM), a mature finite element code under continuing development at Sandia National Laboratories, is the code utilized [SIERRA 2016]. SIERRA/SM has explicit and implicit solver capabilities and is intended for the solution of quasi-static and transient dynamic problems involving general contact, large deformations, and material damage and failure.

Within SIERRA/SM the brittle material is represented using the gradient damage explicit (GDE) material constitutive model. (Note that version 4.41-7 or newer of the code is consistent with the description of the GDE material model given below.) The GDE material model is implemented as a modified version of the gradient damage model outlined by Lorentz et al. [Lorentz 2011]. The response of the model is linear elastic, but incorporates anisotropic stiffness degradation to account for crack formation within the continuum. Instead of directly representing the sharp discontinuities associated with cracks, the presence of a crack is approximately represented by a diffusive auxiliary damage field (or phase field) that smears the effect of each crack over a finite volume in the region of the crack.

The Cauchy stress tensor ($\boldsymbol{\sigma}$) for the material is defined by the following

$$\boldsymbol{\sigma} = A(d)[\lambda \text{tr}\boldsymbol{\epsilon}^+ \mathbf{I} + 2\mu\boldsymbol{\epsilon}^+] + \lambda[\text{tr}\boldsymbol{\epsilon}^- \mathbf{I} + 2\mu\boldsymbol{\epsilon}^-] \quad (6-1)$$

where λ, μ are Lamé constants, $A(d)$ is the stiffness function ($0 \leq A(d) \leq 1$), d is the damage ($0 \leq d \leq 1$), $\boldsymbol{\epsilon}^+, \boldsymbol{\epsilon}^-$ are the positive and negative components of the Green-Lagrange strain tensor, and \mathbf{I} is the identity matrix. In this formulation, the stiffness function only acts to modify the stresses generated by the positive (tensile) components of the strain tensor ($\boldsymbol{\epsilon}^+$) allowing the full strength of the material to be recovered upon crack closure. The positive and negative portions of the Green-Lagrange strain tensor are defined as follows,

$$\boldsymbol{\epsilon} = \boldsymbol{\epsilon}^+ + \boldsymbol{\epsilon}^- = \mathbf{P}\boldsymbol{\Lambda}\mathbf{P}^T, \quad (6-2)$$

with

$$\begin{aligned} \boldsymbol{\epsilon}^+ &= \mathbf{P}\boldsymbol{\Lambda}^+\mathbf{P}^T, \\ \boldsymbol{\epsilon}^- &= \mathbf{P}\boldsymbol{\Lambda}^-\mathbf{P}^T, \end{aligned} \quad (6-3)$$

where \mathbf{P} consists of the eigenvectors of $\boldsymbol{\epsilon}$ and $\boldsymbol{\Lambda}$ is a diagonal matrix of principal strains ($\zeta_1, \zeta_2, \zeta_3$), and

$$\boldsymbol{\Lambda} = \text{diag}(\zeta_1, \zeta_2, \zeta_3), \quad (6-4)$$

$$\Lambda^+ = \text{diag}(\langle \zeta_1 \rangle, \langle \zeta_2 \rangle, \langle \zeta_3 \rangle), \text{ and}$$

$$\Lambda^- = \Lambda - \Lambda^+.$$

The Maccaulay brackets, $\langle \dots \rangle$, in Eq. (6-4) indicate that the maximum value of the principal strain or zero be used in forming the diagonal matrix. The stiffness function in Eq. (6-1) is defined as follows:

$$A(d) = \frac{(1-d)^2}{1 + (m-2)d + (1+pm)d^2}, \quad (6-5)$$

where m depends on the material's modulus of elasticity (E), critical fracture energy or energy release rate (G_c), critical fracture stress (σ_c), and the phase regularization length (L), as follows:

$$m = \frac{3EG_c}{2\sigma_c^2 L}, \quad (6-6)$$

and p is a parameter, subject to the limitations $p \geq 1$ and $p \leq m - 2$, that influences the shape of the stress decay following the initiation of damage.

The material is assumed initially undamaged ($d=0$) throughout. Damage is initiated when the maximum principal stress (σ_1) reaches or exceeds a user defined critical fracture stress (σ_c). Once damage has been initiated, increasing extensional straining of the material results in the accumulation of additional damage, up to a point when the material is completely damage ($d=1$) and retains no strength or stiffness in tension ($A(d=1) = 0$). A damage value of one indicates the formation of crack surfaces. The volume of material over which the effects of a crack are smeared is based on a user-specified length scale (L , the phase regularization length scale). The energy dissipated in the model over this volume during the damage accumulation process is designed to match the fracture energy (G_c) for the material supplied by the user. Once an element is fully damaged ($d \approx 1$), it is removed from the analysis.

The evolution of damage in the material is governed by the evolution equation

$$\eta \dot{d} = -A'(d)\hat{\psi} + c\nabla^2 d - k, \quad (6-7)$$

where $\eta \geq 0$ is the phase viscosity, $\hat{\psi}$ is the driving energy, and c and k are constants that depend on G_c and L as follows:

$$c = \frac{3}{8}LG_c, \quad (6-8)$$

$$k = \frac{3G_c}{4L}.$$

The inclusion of the Laplacian of the damage field ($\nabla^2 d$) in Eq. (6-7) introduces non-locality and results in the damage associated with the formation of a crack being smeared out over some finite volume of material in the vicinity of the crack. The driving energy ($\hat{\psi}$) in Eq. (6-7) is defined as the maximum of the maximum-over-time of the driving energy (ψ^+) for the undamaged material and the ratio k/m , as

$$\hat{\psi} = \max\left(\max_t \psi^+, \frac{k}{m}\right). \quad (6-9)$$

The elastic tensile strain energy for the undamaged material is defined based on the ratio of the maximum principal stress (σ_1^u) for the undamaged material to the critical fracture stress (σ_c) multiplied by the critical fracture energy (G_c)

$$\psi^+ = \frac{\max(\sigma_1^u, 0)}{\sigma_c} G_c, \quad (6-10)$$

where σ_1^u is the maximum eigenvalue of the stress tensor $\boldsymbol{\sigma} = \lambda \text{tr} \boldsymbol{\epsilon} \mathbf{I} + 2\mu \boldsymbol{\epsilon}$ for the undamaged material. Defining the driving energy in the manner shown ensures that the damage field never assumes a non-meaningful negative value, that damage does not begin to accumulate until the maximum principal stress has reached or exceeded the critical fracture stress, and that the process is irreversible (e.g., the material does not heal itself).

To approximately account for spatial variability of critical response characteristics within the real materials being modeled, SIERRA/SM and the GDE material constitutive model allow for the critical fracture stress and fracture energy to be varied on an element-by-element basis. This is achieved by randomly assigning values drawn from Weibull distributions to each element in the continuum model. The initial value assigned for each element and each parameter is calculated as follows:

$$\text{Val} = \bar{\mu} \left(\frac{\ln R}{\ln(1/2)} \right)^{\frac{1}{b}}, \quad (6-11)$$

where $\bar{\mu}$ is the Weibull median, b is the Weibull shape parameter, and R is a random number drawn from a uniform distribution between 0 and 1.

For elements in the macro-scale simulation that suffer complete damage ($d \approx 1$) during the course of a simulation, material property and loading information from the macro-scale model simulation is used to define initial and boundary conditions for the 1-D micro-scale model simulations. The information passed to the lower length scale model includes the material density (ρ), elastic modulus (E), critical fracture stress (σ_c), and fracture energy (G_c); the element's total mass (w); and the strain rate ($\dot{\epsilon} = \boldsymbol{\epsilon} : \boldsymbol{\epsilon}$) the element was subjected to at the time of its fracture initiation (designated $\dot{\epsilon}_{Initial}$) and at the time of its attainment of a fully damaged ($d \approx 1$) state (designated $\dot{\epsilon}_{Final}$). A third rate was also calculated as the average of the initial and final strain rates (designated $\dot{\epsilon}_{Average}$) and passed to the lower length scale model.

6.2.2 Micro-scale model

The micro-scale model consists of a 1-D approach, developed by Zhou et al. [Zhou 2005], that describes fragmentation phenomena as being the result of elastic wave propagation coupled with a cohesive failure process. Both crack nucleation and crack opening are modeled by an initially rigid linear decaying cohesive law, slightly different from the one proposed by Camacho et al. [Camacho 1996] (see Figure 6-1). Prior to providing any further detail about this 1-D approach, briefly introducing other models and discussing their performances is particularly useful in order to justify our choice of the Zhou and Molinari model.

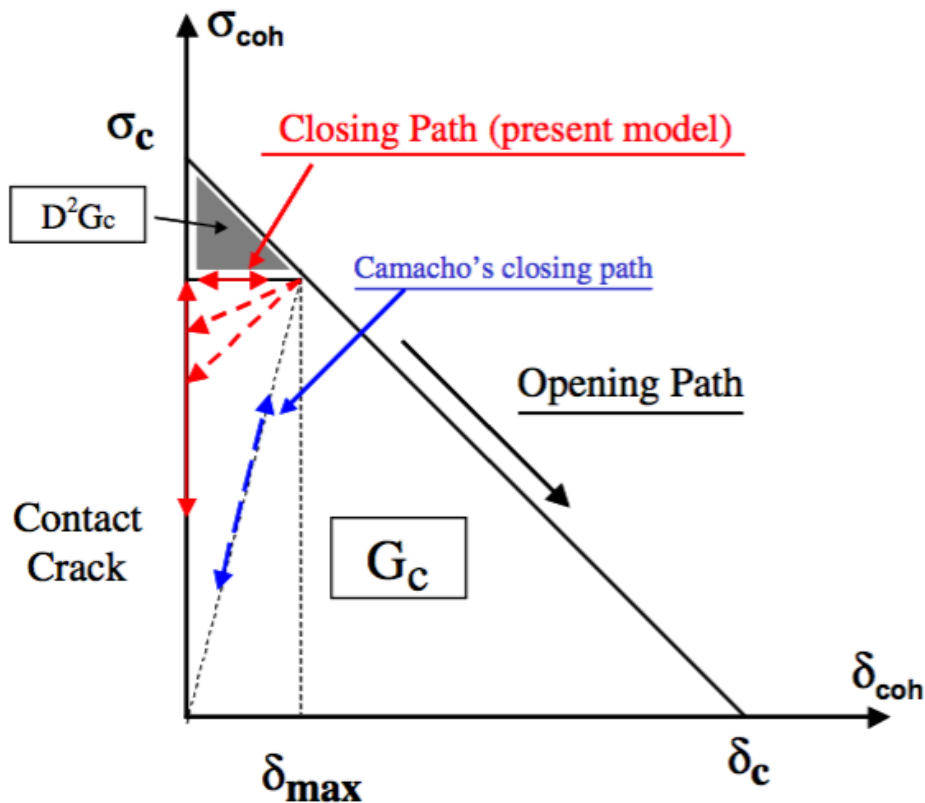


Figure 6-1 Graphical representation of the two irreversible linear decaying cohesive laws developed by Zhou and Molinari and Camacho and Ortiz [Zhou 2005].

First models [Grady 1982, Glenn 1986], referred to as energy models, use energy-based criteria to link strain rates and material properties to average fragment sizes. In the present case, such models have two limitations: first, the models only compute the average fragment size without providing the fragment size distribution, and second, the models generally overestimate the fragment size at high strain rates (see Figure 6-2). More recently, Drugan [Drugan 2001] considered dynamic fragmentation as a process (in contrast to an instantaneous event). At high strain rates, his model predicted average fragment sizes about ten times smaller than the ones obtained with the energy models (see Figure 6-2). Drugan's model is limited in that it assumes that all cracks nucleate simultaneously at equally-spaced loci and it also provides no information about the resulting fragment size distribution. Shenoy and Kim [Shenoy 2003] extended Drugan's work to account for initial internal defects. The defects were incorporated via equally-spaced cohesive node-couples whose behavior obeys an exponential cohesive law. The model proposed by Zhou and Molinari [Zhou 2005] is similar to the one developed by Shenoy and Kim except that they use an initially rigid linear decaying cohesive law (valid for a wider range of strain rates (see Figure 6-2)) and an explicit representation of the internal defect's spatial distribution. Consequently, the Zhou and Molinari model presents the advantages of predicting both the fragment size distribution and average fragment size accurately over a relatively large range of strain rates. In addition, it allows spatial distributions of intrinsic defects to be modeled directly.

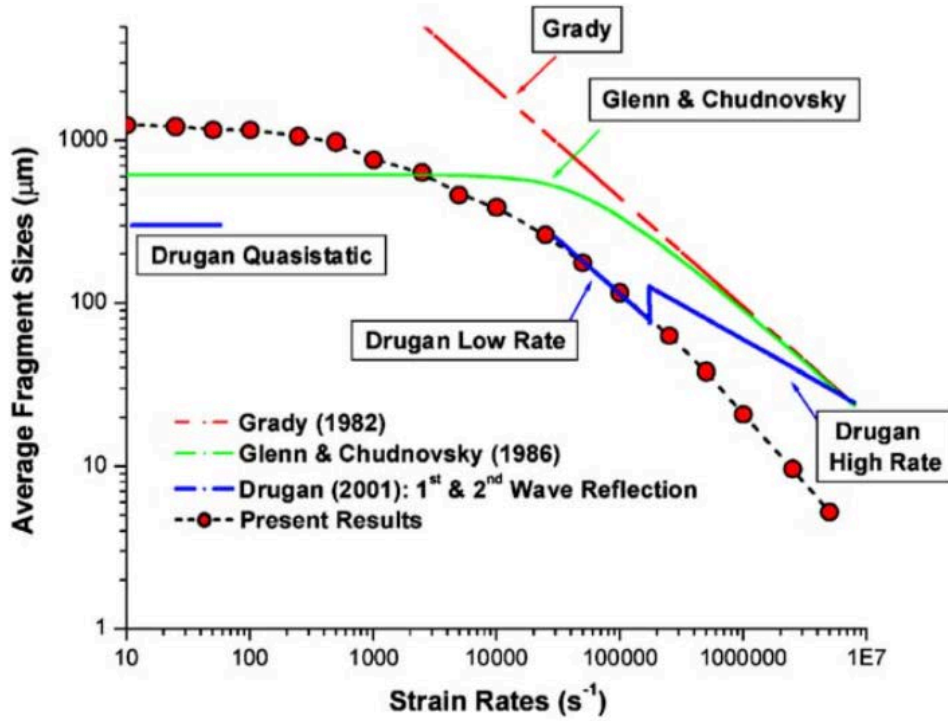


Figure 6-2 Examples of predicted average fragment sizes plotted with respect to strain rates in the case of an initially defect-free homogeneous bar [Zhou 2005].

In the following, any fully damaged element obtained from the macro-scale model is represented as a 1-D bar. The spatial coordinates associated with the left and right extremities of the bar are $x = -L_{bar}/2$ and $x = L_{bar}/2$, respectively, with L_{bar} denoting the total bar length. The element is assumed to be initially (i.e. $t = 0$ s) damage-free with uniform stress σ_0 , strain ϵ_0 and strain-rate $\dot{\epsilon}_0$. Consequently, the initial conditions in terms of velocity, stresses and strains are

$$v(X, 0) = \dot{\epsilon}_0 X, \quad (6-12)$$

$$\epsilon(X, 0) = \epsilon_0 = \frac{\sigma_0}{E}, \quad (6-13)$$

$$\epsilon(X, 0) = \epsilon_0 = \frac{\sigma_0}{E}. \quad (6-14)$$

The boundary conditions, valid at any time $t \geq 0$, are

$$v\left(\frac{L_{bar}}{2}, t\right) = v_R = \dot{\epsilon}_0 \frac{L_{bar}}{2}, \quad (6-15)$$

$$v\left(-\frac{L_{bar}}{2}, t\right) = v_L = -\dot{\epsilon}_0 \frac{L_{bar}}{2}, \quad (6-16)$$

where v_R and v_L correspond to the velocities prescribed on the right and left sides of the bar, respectively.

The following stress criterion determines whether or not a crack nucleates

$$\sigma(X, t) = \sigma_c(X), \quad (6-17)$$

where σ_c , also referred to as the maximum cohesive force, denotes the local strength of the bar.

Crack opening and local stresses are related by the irreversible cohesive law (see Figure 6-1) such that

$$\frac{\sigma_{coh}}{\sigma_c} = 1 - \frac{\delta_{coh}}{\delta_c} \text{ for } \dot{\delta}_{coh} > 0, \delta_{coh} = \delta_{max}, D < 1, \quad (6-18)$$

$$\frac{\sigma_{coh}}{\sigma_c} = 1 - \frac{\delta_{max}}{\delta_c} \text{ for } \delta_{coh} < \delta_{max}, D < 1, \quad (6-19)$$

with δ_{coh} , δ_c , and δ_{max} denoting the current crack opening distance, the critical crack opening distance, and the maximum crack opening distance, respectively. Note that δ_{coh} and δ_{max} coincide when the crack opens or grows, but are no longer the same when the crack shrinks or closes. The damage number D , introduced in the cohesive law, is defined as $D = \min(\frac{\delta_{max}}{\delta_c}, 1)$.

The damage number is a direct indicator of the damage level associated with a given cohesive node. While $D=0$ means that the node is perfectly intact, $D=1$ reveals that the node is fully broken. In the case of a fully broken node, the stress becomes null and the total energy dissipated by the crack is equal to $G_c = \frac{\sigma_c \delta_c}{2}$. More details about the finite difference scheme used by Zhou and Molinari to solve this problem can be found in the appendix of their journal article [Zhou 2005].

6.3 Demonstration Problem

As a demonstration, the two-scale modeling approach has been used to simulate one of the laboratory-scale impact tests that form the basis of the ARF equation provided in DOE Handbook 3010 [DOE 1994] for the free-fall spill and impaction stress release case. In the selected test, a 10 kg cylindrical steel weight was dropped onto a cylindrical ceramic uranium dioxide (UO₂) pellet orientated on its side between two flat hardened steel plates (each about 12.5 mm thick) in a sealed container [Mecham 1981]. The lower plate was restrained from moving while the upper plate was free to translate into the pellet once struck by the falling weight. The drop height of the steel weight was selected so as to provide 1.2 J of kinetic energy per cubic centimeter of specimen material. The UO₂ pellet was comprised of three 13.7 mm diameter by 13.6 mm thick discs of commercially available nuclear power fuel. Following the impact, the resulting UO₂ fragment particles were analyzed and a particle size distribution determined (Figure 6-3).

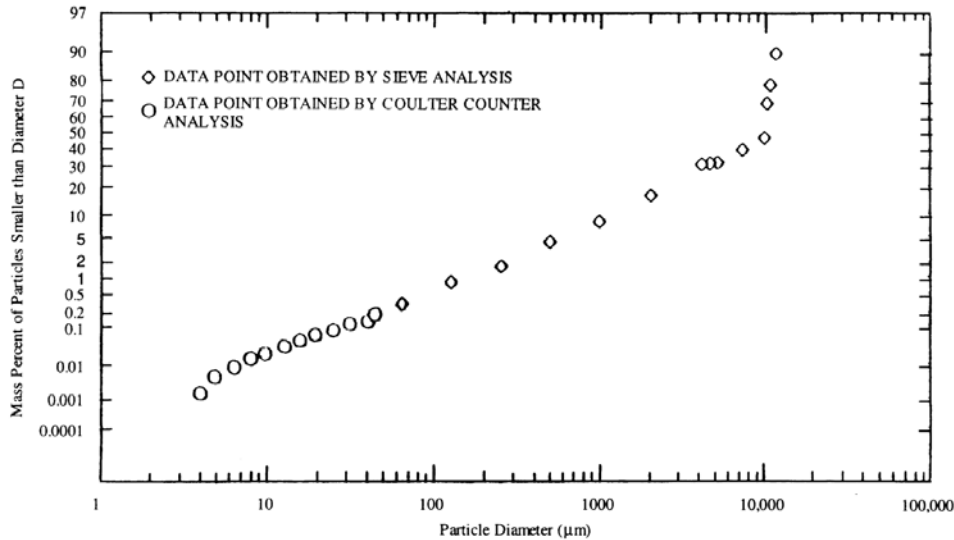


Figure 6-3 Particle sized distribution resulting from UO₂ pellet impact test (taken from [Jardine 1982]).

6.3.1 Macro-scale model

The impact event was modeled using the explicit solver within SIERRA/SM version 4.41-6-508-g049357e6 (Note that this version is a precursor to the 4.41-7 version and includes a coding correction to the GDE material model not found in the 4.41-6 and earlier versions of the code). The ceramic pellet material was represented using the GDE material model. Material properties (density $\rho = 9688 \text{ kg/m}^3$, elastic modulus $E = 137.9 \text{ GPa}$, Poisson's ratio $\nu = 0.3$, critical fracture stress $\sigma_c = 82.7 \text{ MPa}$, and fracture energy $G_c = 75.0 \text{ J/m}^2$) were estimated from material test data for related ceramic materials, or in the case of the critical fracture stress, calculated from an equation found in NUREG/CR-0497 [MATPRO 1979]. The GDE phase regularization length scale was set to 5 times the characteristic element length ($L = 5L_e = 5 \times 0.02 \text{ mm} = 0.1 \text{ mm}$), and the shape parameter $p = 2.0$. To approximately account for real material variability, the critical fracture stress and fracture energy were varied on an element-by-element basis throughout the pellet by randomly assigning values drawn from Weibull distributions (critical stress: $\bar{\mu} = \sigma_c$, $b = 100$; fracture energy: $\bar{\mu} = G_c$, $b = 100$).

To reduce the model size and computation time, a plane-strain representation of the impact test was created. The steel weight, the upper and lower steel plates, and the UO₂ pellet were all included in the model. To maintain the correct ratio of impact-energy to ceramic-pellet-mass, the length of the steel drop weight was adjusted while maintaining its width equal to the original diameter of the cylindrical drop weight used in the test. Each component was represented using eight-node reduced integration hexahedral elements, with one element (approximately 0.02 mm in size) in the thickness direction of the modeled plane. As illustrated in Figure 6-4, a total of about 450,000 elements were used to represent the UO₂ pellet, resulting in an in-plane element size of about 0.02 mm. The lower plate, upper plate, and drop weight were represented with a total of 1430, 1300, and 7568 elements, respectively, yielding approximate element sizes of 1.0, 1.0, and 2.0 mm.

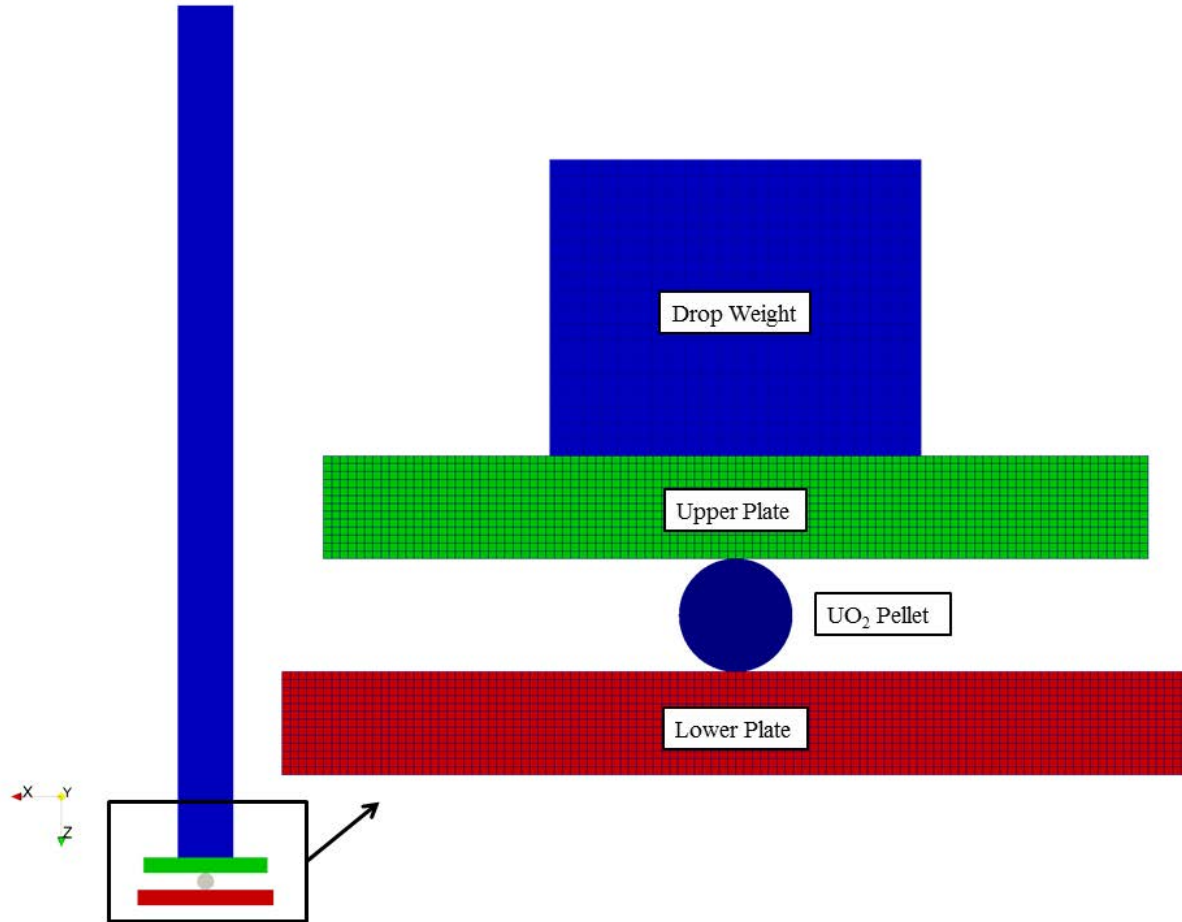


Figure 6-4 Macro-scale finite element model mesh.

In addition to the kinematic boundary conditions applied to enforce a plane-strain condition upon all components of the model, the lower plate was restricted from moving in-the-plane by constraints applied along its lower edge and the upper plate was restricted from lateral translation and rotation in-the-plane by lateral translation constraints applied along its two sides. The drop weight was given an initial velocity of 1.2 m/s, corresponding to an impact energy of 1.028×10^{-5} J, or 1.2 J per cubic centimeter of specimen.

6.3.2 Micro-scale model

The input variables of the one-dimensional micro-scale model fall into two distinct categories. The first one consists of the set of variables that do not change from one element to another. These variables are the Young's modulus (E), the material density (ρ), the total bar length (L_{bar}), the spatial resolution (ΔX) used to discretize the bar and the total number of time steps ($N_{\Delta t}$). Their values are: $E = 137.9 \text{ GPa}$, $\rho = 9688 \text{ kg/m}^3$, $L_{bar} = 17.3 \text{ mm}$, $\Delta X = 2 \text{ }\mu\text{m}$ and $N_{\Delta t} = 10^4$. The second category gathers all the parameters whose value is directly related to the element considered. These input variables are the volume and mass of the element, the critical fracture energy, the critical fracture stress and the strain rate the element was subjected to at the time of its failure. Note that it has been assumed in the present case that both the critical fracture energy and the critical fracture stress are constant and uniform throughout the whole bar. The micro-scale model does not require any additional data in order to be capable of computing, for each broken element, the number of fragments as well as the size and mass of each fragment.

6.4 Results and Analysis

The macro-scale finite element simulation was performed first. Post-processing of the output data from the macro-scale simulation extracted the requisite information for performing the 1-D micro-scale simulations. Micro-scale simulations were performed, one for each element in the macro-scale model that suffered complete damage. Results from the macro- and micro-scale models were then combined to determine the full range of particle size distribution information.

6.4.1 Macro-scale model

Figure 6-5 shows the resulting macro-scale fragmentation predicted by the finite element model, as well as the material damage plotted on the undeformed mesh. Figure 6-6 shows the associated particle size distribution expressed as the mass-percentage-of-particles-smaller-than-diameter versus particle geometric diameter. Because fully damaged elements are removed from the simulation during the fracture event, some of the UO_2 mass is lost. A total of 31,385 elements were removed from the simulation. These elements represent about 7.6% of the initial specimen mass. As a result of this, the particle size distribution resulting directly from the finite element simulation (labeled as FEM in Figure 6-6) never drops below about 7.6%. This illustrates the fact that the macro-scale model is not able to accurately resolve fragments with a size less than about $500\ \mu\text{m}$. To determine the full range of the sizes of the particle that are produced, a lower-length scale model capable of accurately resolving the micro-scale fragments is also required.

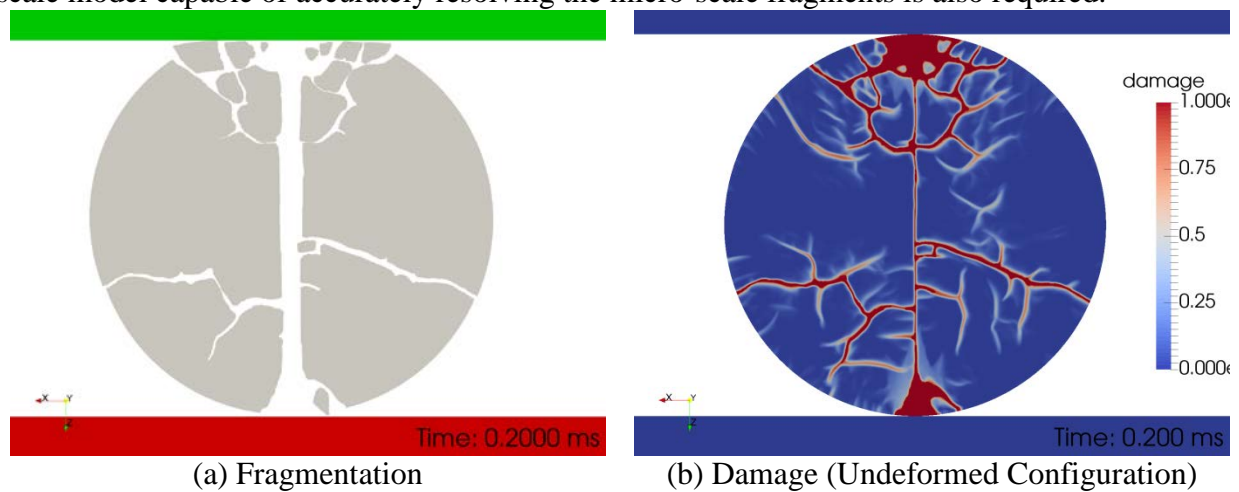


Figure 6-5 Fragmentation predicted by macro-scale finite element model.

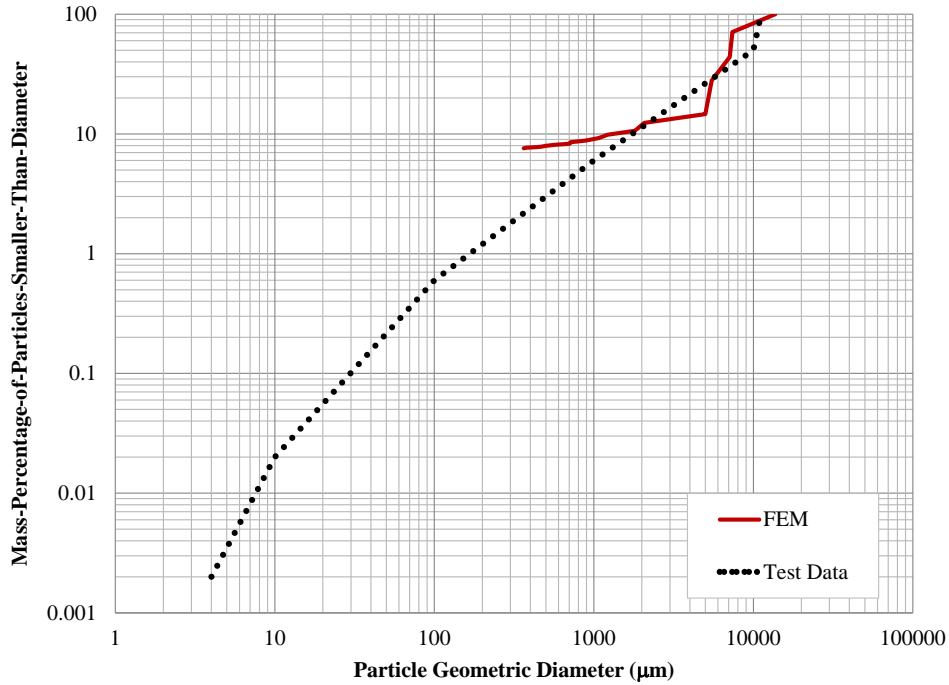


Figure 6-6 Particle size distribution resulting from the macro-scale finite element model compared to the test data [Jardine 1982].

Figure 6-7 shows a frequency diagram of fracture strain rates for the 31,385 failed elements for each of the strain rates used in the 1-D micro-scale model simulations. The resulting strain rates appear to be reasonably well represented by a log-normal (base 10) distribution, with an average strain rate of about $10^{3.73} = 5370 \text{ s}^{-1}$, $10^{4.67} = 46,774 \text{ s}^{-1}$, and $10^{4.91} = 81,283 \text{ s}^{-1}$ for the initial, average, and final rates, respectively.

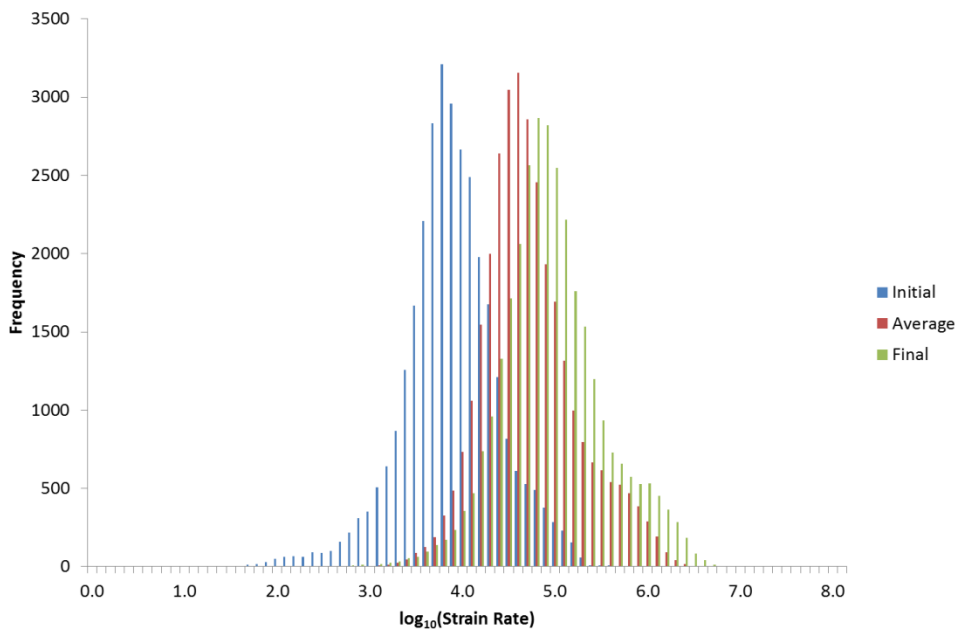


Figure 6-7 Failed element strain rate frequency plot.

6.4.2 Micro-scale model

A micro-scale model simulation was run for each of the 31,386 fully damaged elements resulting from the macro-scale simulation, and for each of the three (initial, average, and final) strain rates provided. The results of the simulations are provided in Figure 6-8 with the fragment size distributions and cumulative mass ratios for each of the three strain rates plotted. The cumulative mass ratio is defined here as the cumulative mass divided by the mass associated with the 31,386 fully damaged elements (which in this case represents only about 7.6% of the total mass of the UO₂ pellet). Results from the simulations reveal that the choice of prescribed strain rate in the micro-scale model has a significant effect on both the average fragment size and fragment size distribution. The average fragment sizes associated with the initial (Figure 6-8a), average (Figure 6-8b), and final (Figure 6-8c) strain rate cases are 418 μm , 32 μm , and 62 μm , respectively. Figure 6-9 shows the same information plotted in a manner consistent with Figure 6-3 and Figure 6-5. The effect of the choice of strain rate utilized in the micro-scale model simulations is clearly significant, particularly for the smaller particle sizes in the 10 μm range.

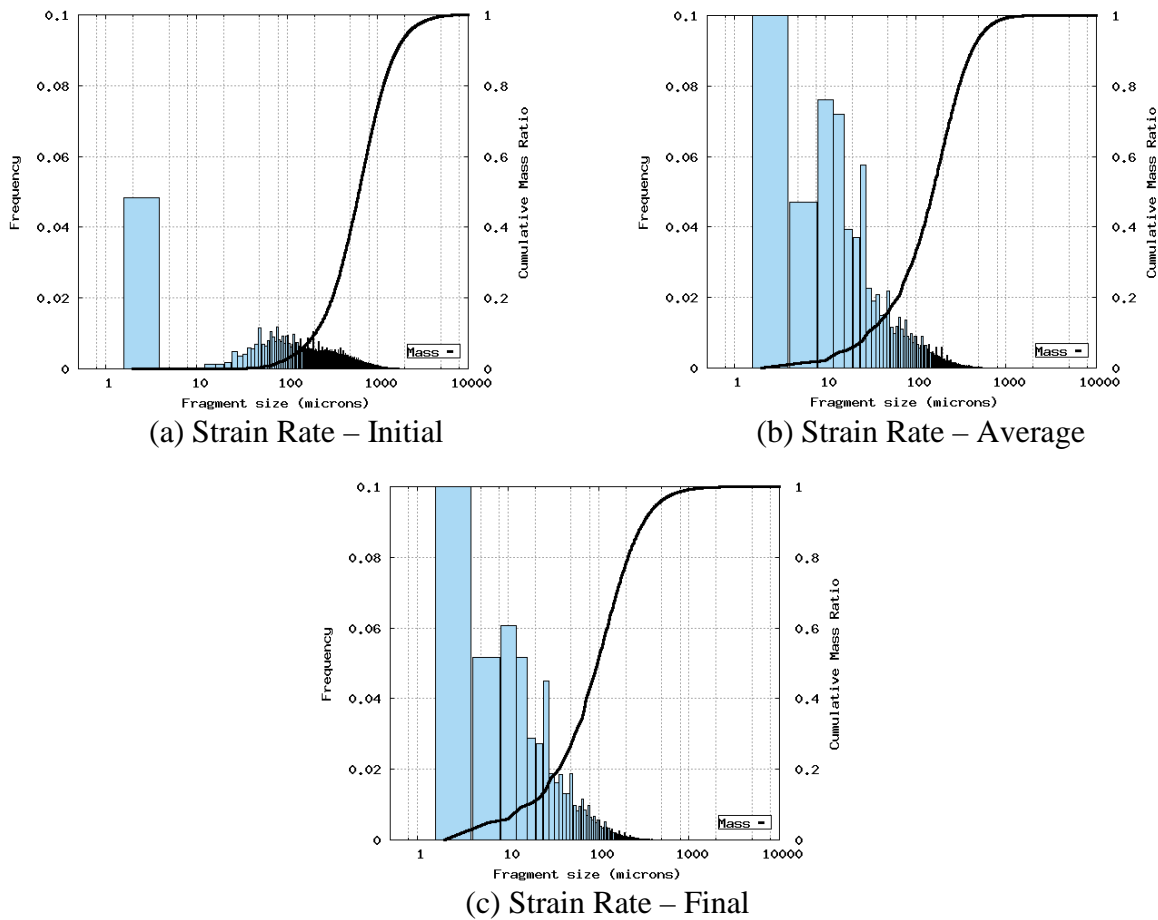


Figure 6-8 Fragment size distributions and cumulative mass ratios resulting from micro-scale model simulations.

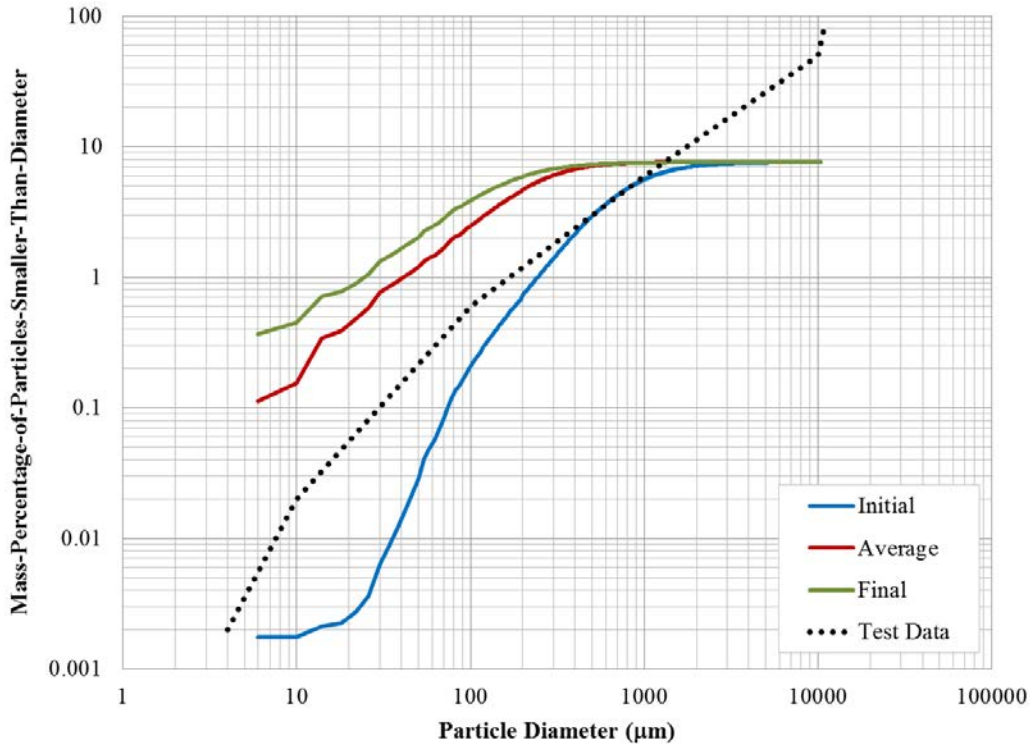


Figure 6-9 Particle size distribution resulting from the micro-scale model simulations compared to the test data [Jardine 1982].

6.4.3 Combined two-scale model

Combining the particle size data provided by the 1-D micro-scale model with the macro-scale particle size data provided by the finite element model produces the two-scale model prediction. This combination of the results from the two models is done on a mass scaled basis. The mass distribution resulting from the macro-scale model is taken as the mass distribution for 92.4 % of the initial pellet mass (equivalent to the mass of the elements retained in the macro-scale simulation) and the mass distribution resulting from the micro-scale model simulations is taken as the mass distribution for the remaining 7.6% of the initial pellet mass. The resulting combined mass distributions are given in Figure 6-10.

The two-scale model results match reasonably well with the impact test data. The choice of strain rate used to initialize the micro-scale model simulations significantly affects the resulting particle size distribution; particularly in the particle size range of interest for safety evaluations. Results from the three rates selected do bound the test data, which is encouraging, and potentially indicates that improved results may be obtained if strain rate time-histories from the macro-scale model are used instead to define the boundary conditions for the micro-scale model simulations. The new material model to be developed in the third phase of this project will have this capability.

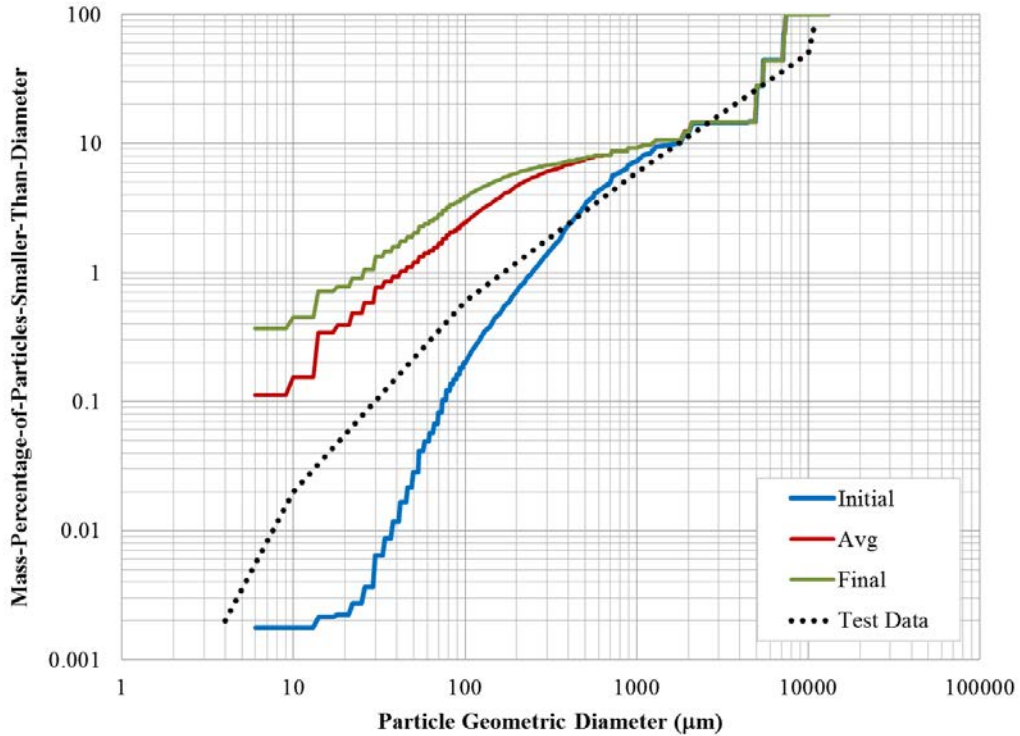


Figure 6-10 Particle size distribution resulting from the combination of the macro- and micro-scale model simulations compared to the test data [Jardine 1982].

6.5 Conclusions

The two-scale modeling approach presented has been shown to be capable of providing reasonably accurate particle size distribution predictions across the entire particle size range of interest for brittle radioactive material forms susceptible to fracture through its application to a laboratory-scale UO_2 impact test. The approach is particularly promising because it provides the necessary level of accuracy, fidelity, and versatility for making safety assessments of brittle radioactive materials subjected to wide-ranging accident conditions while remaining computationally tractable.

7 SUMMARY AND CONCLUSION

This report discusses the Year 2 accomplishments of an NSRD project substantiating the DOE-HDBK-3010 using SNL SIERRA code suite, such as the SM code Adagio/Presto and the FD code Fuego. In Year 2, we were tasked to improve Fuego code by implementing a particle resuspension model and a multi-component evaporation model as described in Chapter 2. To test the resuspension model implemented in Fuego, we had identified a resuspension experiment data from the Handbook that simulated the resuspension due to human activity [Fish 1967] as described in Chapter 3. Two specific fire experiments in Chapter 3 of the Handbook were simulated to demonstrate Fuego capability: a beaker fire experiment (described in Section 3.3.1 of the Handbook) and a gasoline pool fire (described in Section 3.3.6 of the Handbook).

7.1 Fuego Model Improvement

Chapter 2 describes the enhancement to Fuego to allow particle resuspension from deposited surfaces and to allow better characterization of multi-component effects on evaporations.

In the resuspension model effort, we attempt to characterize the model by using a number of parameters that can be input to Fuego, allowing various flow and particle conditions. We have demonstrated development test problems, which illustrates the usefulness of the model. This model may be only suitable for a certain range of the particle sizes and flow velocities without additional work.

In terms of the multi-component evaporation model, we have provided the basic evaporation model, and the simplified approach to model multi-components of an evaporating droplet. We also provided development example inputs for testing this model. The simplified approach describes the beaker fire experiment which was described in detail in Chapter 4 of this report. The resuspension model was used in Chapter 3 for analyzing two experiments from the Handbook.

In conclusion, we have provided the code improvement to Fuego to allow modeling of the particle resuspension and multi-component evaporation of liquid droplets. Fuego improvement will be continued as the code applications are widening. In particular, the deposition (or sticking) of particles with low Stokes numbers (small diameters) in the turbulent boundary layer can be improved. The deposition process is dependent on the boundary layer, fluid velocity, particle's size and flow direction. In addition, the particle agglomeration is an important process. We had begun to implement a particle attractive force model. The work is still ongoing.

7.2 Resuspension Model Testing

In Chapter 3, we attempted to test the resuspension model described in Chapter 2 by using the resuspension data in the Handbook. We were able to model the human activity in a room that results in resuspension of particles.

The Handbook uses data generated about 50 years ago to estimate a resuspension factor. This is only a single number to provide a time and spatially integrated value for the fraction of aerosol

particles that would be resuspended above a contaminated surface for a range of activities. The experiments were not well characterized by today's standards since measurement equipment and diagnostics were limited. Nonetheless, the resuspension factor is used and provides a basis for assessing computational modeling of the resuspension process.

By using our existing flow modeling software and state-of-the-art computer hardware, we demonstrated that it is possible to simulate a resuspension experiment. The simulations have tremendous fidelity in terms of where and when aerosol particles would be resuspended for accidents of interest. In this work we compared the computed resuspension factor to the measured value for particles of known size and physical properties that were deposited on a floor. The computations were within an order of magnitude of the measured resuspension factor, which is good considering that the conditions of the experiments were not provided in detail.

The ability to model a human walking in a simulation is a challenge task, particularly when the experimental description is not clear and specific. Despite these issues, we demonstrated that we can use Fuego code to simulate human activity in a CFD code.

7.3 Reanalyzing Fire Experiments

In Chapter 4, we re-analyzed the beaker and gasoline pool fire simulations as described in Year 1 of this project. Both the resuspension and the multi-component evaporation models for the Fuego improvements were used in the simulations reported in this chapter.

Beaker Fire Experiment:

Our results indicate that contaminant release from a burning fuel with entrained contaminant droplets is not principally due to initial flame dynamics, though that was observed in the original study in Year 1 with non-evaporating inertial particles. The variation of the particle insertion data played the largest role with turbulence variation near the pool surface showing less importance. Initial pool height had large impact on the ARF, and, as in the earlier study, it is clear that more experimental results would be helpful in exploring this variation. Since the goal of the DOE handbook is to provide conservative estimates for these scenarios, and greater contaminant release rates were observed both at lower (0mm) and higher (40mm) pool heights than the nominal of 20mm, variation in pool height should be explored further.

Gasoline Pool Fire Experiment:

For this experiment, we conclude the following:

- Multiple entrainment mechanisms were presented as potential methods for hazardous contaminant release from contaminated fuel fires.
- The predicted ARF calculated by a CFD code was compared to the ARF measured in a relevant historical experiment and previous computational work. The addition of multiple species evaporation and deposition for particles provided new insight to the entrainment dynamics. The volatile fuel was seen to evaporate rapidly in the fire above the pool surface, increasing the likelihood that the remaining non-volatile solid contaminant would transport down the wind tunnel and reach the outflow.
- Practical assumptions for the turbulence boundary conditions result in significant uncertainty in the ARF.

- Boiling mechanism duration was again found to be the most significant factor in predicting the ARF. Improved modeling of particle entrainment from pool boiling will help the quantitative accuracy of this type of modeling.
- The particle input temperature did not significantly alter the volatile evaporation, resulting in similar contaminant release.
- Future work would include longer duration simulations of the resuspension of deposits left from a multiple component boiling entrainment scenario in order to detect contaminant release at the collection point, potentially enabling a prediction of the resuspension entrainment ARF.

7.4 Powder Release Experiments

In Chapter 5, three simulations were conducted for the free-fall spills. 50 psig (0.34 MPa) and 250 psig (1.72 MPa) pressurized powder release cases in the experiments conducted in RART were also performed.

A gravitational (free fall) spill simulation of 100 g of TiO₂ powder in a beaker has been done, 10⁸ out of 10¹³ of the particles in 100 g were tracked. We have used a fine mesh for this simulation, which is a significant improvement over that of Year 1. We model the prescribed sample flow and introduce a turbulence model approximation, both improvements over the Year 1 effort. When the beaker is turned, the falling powder will interact the surrounding air, and induce the fluid flow within the RART volume. The induced fluid velocity can be used by MELCOR [Louie 2016]. We were able to run the simulation to the experiment end time of 30 minutes.

However, the aerosol result of the simulation overestimates the ARF in terms of the particles collected in the samples. This difference may be due to the following factors:

- Fuego currently does not model agglomeration, which may cause the settling to be faster.
- The assumption of 10⁸ (10⁵ with 1000 particles per parcel) particles in the model versus the actual number of particles of 10¹³ may overestimate the number of particles pulled through the samples.
- The turbulence flow model used may influence the mixing that causes the overestimation.
- The percent particle collected is a number percent, which may be different than the experiment data as a mass percent.

In the pressurized release experiments, we conducted both 50 psig (0.34 MPa) and 250 psig (1.72 MPa) cases. Because Fuego is a low-Mach number (< 0.7) fluid code, we can only model the 50 psig (0.34 MPa) case (Mach number is about 0.38). For the higher pressure case, we use SIERRA/SM (Presto) code to perform the initial blast of the powder and pass the particle data to Fuego at a later time for simulating the rest of the experiment condition.

50 psig (0.34 MPa) Case

For this pressure case, the simulation of the rupture disk in the experiment for the pressure release from the PARE to RART was assumed to be done within ~ millisecond. The fluid velocity of 643 m/s was assumed for this pressure case. The results show that the particle cloud rises up toward the ceiling of RART in a short time, while the sampling (or filters) flow pulls the particles toward the sampling devices. As the simulation continues, particles that impact to the ceiling or hit the PART walls will stick or deposit. Because of the difficulties to observe any deposition, additional simulation runs with fluid open boundary conditions were used to allow depositions. Despite this issue, the deposition values are reported for both the ceiling and filters.

250 psig (1.72 MPa) Case

For this pressure case, the simulation of the powder release of 250 psig (1.72 MPa) was first done through the use of Presto code. Initially, a coarse mesh was used to model the TiO₂ powder by using SPH model in the PARE with the prescribed pressure as the induced pressure (or stress) load. However, the size of this stress is insufficient to induce the release of the powder. Therefore, a multiplication of 1000 is applied to this stress. This increase in value is justified, because Presto is modeled solids, and it does not model fluid, even though there is an ideal gas model (only in the ITAR version), which is not truly modeling the gas as in a fluid code like Fuego. In reality, when the PARE is pressurized, both powder and air inside the PARE are at pressure. Without modeling the gas portion, the induced stress needed to be larger in order to push the particles out of the PARE volume. When passing the particles to Fuego, the induced fluid flow by the injecting particles may not yield the actual fluid conditions as in the experiment. That is why the use of the multiplier is justified.

At first, the coarse particle sizes in the order of millimeters from the Presto run were input to Fuego run. The Fuego model was based on the “no flow” case for the 50 psig (0.34 MPa) simulation described in Table 5-9. In this case, the Fuego run showed that the particles were stuck to the surfaces early because the particles are too large. In the fine particle size run (using the results of Presto in the second run), the Fuego results showed that the particles were very slow because the micron-sized particles could not influence the fluid in the RART volume. Therefore, the multi-size particle run (using final run of Presto simulation) was conducted. In this simulation, the results are more encouraging. Because the particles imparting the ceiling were not able to stick the surfaces as indicated in the experiment, a separate Fuego model (using the “middle” case in Table 5-9 for the 50 psig case) was conducted. However, the results showed slightly improved deposition onto the middle ring of the RART ceiling in comparison to what was observed in the same case for the 50 psig (0.34 MPa) simulation. This may be because of the selection of the turbulence model chosen or other effect associated with the boundary layer. Thus, iterations may be required to model the condition of the experiment correctly.

In conclusion, the coupled method of using Presto and Fuego is proven to be useful to address high Mach number flow, which Fuego alone cannot be able to handle. However, iterations and the use of a multi-size particle approach are needed in order to produce meaningful results.

7.5 Fragmentation Analysis

Unlike to the two previous chapters to re-analyze the Year 1 simulations, the fragmentation analysis in Chapter 6 is intended to explore if SIERRA/SM code can be used to simulate the fragmentation experiment data described in Section 4.3.3 of the Handbook.

The two-scale modeling approach uses the finite element method to simulate dynamic fracture under general loading and boundary conditions to determine macro-scale fragmentation. At the lower length scale, a 1-D model is used to determine the micro-scale fragmentation. Boundary conditions for the 1-D model are derived from the macro-scale model. Fragmentation characteristics from both length scale models are combined to determine the resulting fragment size distribution spanning both length scales.

The two-scale modeling approach presented has been shown to be capable of providing reasonably accurate particle size distribution predictions across the entire particle size range of interest for brittle radioactive material forms susceptible to fracture through its application to a laboratory scale UO₂ impact test. The approach is particularly promising because it provides the necessary level of accuracy, fidelity, and versatility for making safety assessments of brittle radioactive materials subjected to wide ranging accident conditions while remaining computationally tractable.

This Page Intentionally Left Blank

8 RECOMMENDATIONS FOR FUTURE WORK

In this chapter, we provide recommendations for future work for this project. Our research is intended to provide a numerical capability using SIERRA tools to substantiate ARF and RF data in the Handbook. During the research, we have identified a number of recommendations to improve SIERRA tools to better support ARF/RF data. Similarly, when we conducted the simulations using the SIERRA tools, we often used assumptions in the calculations. These assumptions or modeling methods may not be fully validated to model or compare well with experiment data. Thus the further analyses are recommended for the simulations we provided in this research.

Fuego Code Improvement

In this year, we implemented two new particle models into SIERRA/FD (Fuego): Resuspension and multi-component evaporation models. Both models have been tested as described in Chapter 2 through Chapter 4 of this report. We offer a number of Fuego improvement needs to better model the ARF data in the Handbook (see Table 8-1).

Table 8-1 Fuego Particle Model Improvement Needs

Model	Description
Agglomeration	Although the adhesive model is being implemented in the code, the completion of the model will help to better model the powder release simulations as described in Chapter 5.
Deposition	Deposition is an important model for aerosol physics. In this research we have encountered a number of issues relating to the deposition (sticking in Fuego’s term) when the particles are deflected from the surfaces. As described in Chapter 2, the deposition model in Fuego will be improved in the coming year, particularly with respect to boundary layer entrainment of small particles. If the deposition allows the particles to agglomerate as in a real situation, then the particle resuspension model can be more realistic, since the current resuspension only models the resuspension according to the same particle deposition size distribution (that ignores agglomeration).
Boundary Layer	The particle impact behavior in the boundary layer needs further validation.

Fuego Resuspension Model Testing

In this year, a particle resuspension model has been implemented in Fuego. We attempted to test this model by selecting resuspension experiment data from the Handbook and a reactor experiment of STORM SR-11 (see Chapter 3 of this report). However, we decided to stop the simulation of the STORM SR-11 test because the high fluid velocity creates a large computational cost to resolve the flow for the long duration of the experiment. On the other hand, we successfully demonstrated model predictions for the human activity resuspension experiment (see Chapter 3 for the Fish experiment) from the Handbook. Because the experiment was not well described the test report, (conditions such as the pace of the human walking on a contaminated surface and the collection method) it is difficult to assess model accuracy.

Therefore, a number of assumptions were used to model the human walking and duration. The Fuego calculation with the resuspension model did not compare well with the experiment data. Because the calculation was done using an older version of Fuego which did not include turbulent variations in the wall shear stress, it is recommended that the calculation needs to be redone with the final version of the resuspension model. In addition, a separate calculation without the use of the resuspension model should be conducted to ensure that the assumed human walking motion model in the Fuego simulation may actually induce realistic resuspension.

Fire Experiments

This year, we have demonstrated that the improved Fuego models—such as the multi-component evaporation model—could contribute better predictions of the experimental data in both beaker and gasoline pool fires. We were not able to demonstrate the resuspension model fully for the gasoline pool fire test due to lack of a relevant model parameter set. The deposition model in Fuego may require the addition of particle agglomeration models to capture some of the relevant deposition processes. To better observe the resuspension phenomena, the simulations needed to be run longer to be more consistent with the experiment.

Powder Release Experiments

In Chapter 5, we modeled the gravitational (free-fall) experiment and two pressurized release cases (50 psig and 250 psig) of TiO₂ powders in RART. For both free fall and the 50 psig pressurized release experiments, we were able to demonstrate the simulations out to 30 minutes. For the free-fall case, we estimated the ARF and compared it with the experimental data. If the agglomeration physics were included in the Fuego particle physics model, then the comparison might be better. We recommend repeating the free-fall case simulation once the particle agglomeration model is added to Fuego. In addition, the free-fall experiments as described in [Sutter 1981] contained different fall height and powder material. The additional cases should be run to substantiate the data for these experiments as well. For the pressurized release cases of [Sutter 1983], the inclusion of boundary layer entrainment and other particle forces (e.g. Van der Waal or electrostatic) may change the simulated particle interactions with the RART ceiling. To model the 250 psig pressure case, we used a number of Presto models to obtain energetic particles (kinetic energies) to be passed to Fuego simulations, so that they can be compared to the experimental data. We determined that multi-size particle models were needed in order to produce reasonable agreement with the experiments. Additional simulations are required to fine tune the multi-size particle models from Presto to Fuego in order to produce meaningful results. Therefore, it is recommended that these additional simulations be performed and that the simulations should be conducted out to 30 minutes. If the Fuego improvement, as described in Table 8-1 were added, these additional simulations can be more realistically modeled.

Fragmentation Analysis

As described in Chapter 6, a capability to model the fragmentation experiment data of the Handbook was demonstrated. A two-scaled modeling approach was employed to address the disparate length scales involved (particles ranging in size from millimeters to microns). The two-scale model results match the impact test data reasonably well. The choice of strain rate used to initialize the micro-scale model simulations has a significant effect on the resulting particle size distribution; particularly in the particle size range of interest for safety evaluations. Results from the three rates selected do bound the test data, which is encouraging, and potentially indicates

that improved results may be obtained if strain rate time-histories from the macro-scale model are used instead to define the boundary conditions for the micro-scale model simulations. Therefore, it is recommended to further develop this capability as discussed in Year 3 tasks below.

Year 3 (FY2017) Tasks

As of Year 2 we addressed the experimental data of the fire and powder releases in Chapter 3 and Chapter 4 of the Handbook. In addition, we also addressed the capability of SIERRA/SM code to model the fragmentation experiment of a fracture of a UO_2 pellet using two-scale model approach as described above. In this capability, a microscopic 1-D model was developed to provide a way to predict finer fragments in the range of 10 microns or less. The results from this approach seem to agree well with the experiment data. To reduce the explicit coupling between the macro-scaled and micro-scaled simulations, we will implement the microscopic scaled model into SIERRA/SM (Presto) as a material model in the coming year. In addition, we plan to address Chapter 5 and Chapter 6 of the Handbook in FY2017. For Chapter 5 of the Handbook, we propose to add a breach and combustion scenario involving the content of a 55-gallon waste drum. We propose the addition because no such data existed previously and because a drum accident occurred recently at the Waste Isolation Pilot Plant which prompted the review of any potential breach of waste drums. In addition, we propose to address Chapter 6 “Inadvertent Criticality” to examine more recent data in the open literature and assess the data within the Handbook. This is important because much of the documented source terms for the nuclear criticality were from NRC regulatory guides that have been cancelled and represented the data that is not thoroughly applicable to DOE facilities and fissile material configuration at DOE sites.

This Page Intentionally Left Blank

9 REFERENCES

- [Bagul 2013] Bagul, R.K., D. S. Pilkhwal, P.K. Vijayan, and J.B. Joshi, "Entrainment phenomenon in gas-liquid two-phase flow: A review," *Sadhana*, 38(6), pp. 1173-1217, (2013).
- [Borkowski 1986] Borkowski, R., Bunz, H., and Schoeck, W., "Resuspension of Fission Products during Severe Accidents in Light-Water Reactors," KfK3987, EUR 10391, May (1986).
- [Brown 2006] Brown, A.L., Vembe, B.E., "Evaluation of a model for the evaporation of fuel from a liquid pool in a CFD fire code," Proceedings of the ASME International Mechanical Engineering Congress & Exposition, November 5-10, 2006, Chicago, IL, USA, IMECE2006-15147
- [Brown 2009] Brown, Alex, "Impact and Fire Modeling Considerations Employing SPH Coupling to a Dilute Spray Fire Code," Proc. 2009 ASME Summer Heat Transfer Conference, San Francisco, California, USA July 19-23, 2009..
- [Brown2012] Brown, Alex et al. "Impact, Fire, and Fluid Spread Code Coupling for Complex Transportation Accident Environment Simulation," *Jour. Thermal Sci. Eng. Applications*, 4, 021004, (June 2012).
- [Brown 2015] Brown, Alex and Louie, David "Contaminant Entrainment in a Liquid Fuel Fire," TFESC-12948, 1st Thermal and Fluid Engineering Summer Conference, New York, NY, August 9-12, 2015.
- [Brown 2015a] Brown, A. L., Zepper, E. T., Louie, D. L. Y., Restrepo, L. "Contaminant Entrainment from a Gasoline Pool Fire," SAND2015-7185C, September 2015, Sandia National Laboratories.
- [Camacho 1996] Camacho, G. T., Ortiz, M., "Computational modeling of impact damage in brittle materials," *International Journal of Solids and Structures* 33, pp 2899-2938 (1996).
- [Derakhti 2014] Derakhti, M., and Kirby, J.T., "Bubble entrainment and liquid-bubble interaction under unsteady breaking waves," *J. Fluid Mech.* 761, 464-506, 2014.
- [DOE 1994] Department of Energy, Airborne Release Fractions/Rates and Respirable Fractions for Non-Reactor Nuclear Facilities, Volume 1 and 2, DOE-HDBK-3010-94, U.S. Department of Energy, Washington, DC, December 1994, Reaffirmed 2013.
- [Domino 2003] Domino, S. P., Moen, C. D., Burns, S. P., and Evans, G. H., "SIERRA/Fuego: A Multi-Mechanics Fire Environment Simulation Tool," AIAA Paper 2003-0149, 41st AIAA Aerospace Sciences Meeting, Reno, NV, January 2003.
- [Drysdale 1998] Drysdale, An Introduction to Fire Dynamics, Second Edition, John Wiley & Sons, Inc., 1998.
- [Drugan 2001] Drugan, W. J., "Dynamic fragmentation of brittle materials: analytical mechanics-based models", *Journal of Mechanics and Physics of Solids* 49, pp 1181-1208 (2001).
- [Faeth 1983] Faeth, G.M., "Evaporation and combustion of sprays," *Prog. Energy Combust. Sci.*, 9, 1-76, (1983).

- [Fish 1967] Fish, B. R., R. L. Walker, G. W. Royster, and J. L. Thompson, "Redispersions of Settled Particulates," Health Physics Division, Oak Ridge National Laboratory, 1967, in "Surface Contamination: Proceedings of a Symposium held at Gatlinburg Tennessee, June 1964," B. R. Fish (Ed.), Pergamon Press, pp. 75 - 81, 1967.
- [Fluent 2012] Fluent®, Lecture 10 Best Practice Guidelines, 14.5 Release, ANSYS® Corporation, Canonsburg, PA, 2012
- [Gelbard 2013] Gelbard, F., Brown, A., Louie, D., Feng, C. and Bixler, N., "A Basic Principles Approach for Determining Radionuclide Releases from Accidental Explosions in Reprocessing Facilities," Proceeding to the 2013 ANS Winter Meeting and Nuclear Technology Expo, Washington DC., November 10-14, 2013.
- [Glenn 1986] Glenn, L. A., Chudnovsky, A., "Strain-energy effects on dynamic fragmentation", Journal of Applied Physics 59, pp 1379-1380 (1986).
- [Grady 1982] Grady, D. E., "Local inertia effects in dynamic fragmentation", Journal of Applied Physics 53, pp 322-325 (1982).
- [Henry 2014] Henry, C. and J. P. Minier, "Review: Progress in particle resuspension from rough surfaces by turbulent flows," Progress in Energy and Combustion Science, 45, 1-53, 2014.
- [Hagrman 1979] Hagrman, D. L., and Reymann, G. A., "MATPRO-Version 11 A Handbook of Materials Properties for use in the Analysis of Light Water Reactor Fuel Rod Behavior," NUREG/CR-0497, EG&G Idaho, Inc., Idaho National Engineering Laboratory, Idaho Falls, ID (1979).
- [Haschke 2008] Haschke, John M., and Stakebake, Jerry L., "Handling, Storage, and Disposition of Plutonium and Uranium." The Chemistry of the Actinide and Transactinide Elements. Third Edition. Ed. Lester R. Morss. Ed. Norman M. Edelstein. Ed. Jean Fuger. Dordrecht, The Netherlands: Springer, pp. 3199-3272 (2006).
- [Humphries 2015] Humphries, L.L., Cole, K.K., Louie, D.L., Figueroa, V.G. and Young, M.F., **MELCOR Computer Code Manuals- Vol.1: MELCOR Primer and Users Guide, Version 2.1 6840 2015**, SAND2015-6691 R, Sandia National Laboratories, Albuquerque, NM, August 2015.
- [IAEA 1965] "Technical Report Series #59: Thermal Conductivity of Uranium Dioxide: Report of the Panel on the Thermal Conductivity of Uranium Dioxide," STI/DOC/10/59, International Atomic Energy Agency, Vienna, Austria, (26-30 April 1965).
- [Jardine 1982] Jardine, L.J., Mecham, W.J., Reedy, G.T. and Steindler, M.J., Final Report of Experimental Laboratory-Scale Brittle Fracture Studies of Glasses and Ceramics, ANL-82-39, Argonne National Laboratory, Argonne, IL October 1982.
- [Kataoka 1983] Kataoka, I., and Ishii, M., "Mechanistic Modeling and Correlations for Pool-Entrainment Phenomenon," NUREG/CR-3304, ANL-83-37, April (1983).
- [Kogan 2008] Kogan, V., Schumacher, P.M., "Plutonium release fractions from accidental fires," *Nuclear Technology*, 61, pp. 190-202, (2008).

- [Lefebvre 88] Lefebvre, A.H., Atomization and Sprays, Hemisphere Publishing Company, 1988.
- [Lick 2009] Lick, W.J., Sediment and contaminant transport in surface waters, Taylor & Francis, 2009.
- [Lorentz 2011] Lorentz, E., Cuvilliez, S., and Kazymyrenko, K., “Convergence of a gradient damage model toward a cohesive zone model,” *Comptes Rendus Mecanique*, 339, 1, 20-26 (2011).
- [Louie 2015] Louie, D.L.Y. and Brown, A. NSRD-6: Computational Capability to Substantiate DOE-HDBK-3010 Data, SAND2015-10496, Sandia National Laboratories, Albuquerque, NM, November 2015.
- [Louie 2016] Louie, D.L.Y., et.al, NSRD-10: MELCOR 2.1 Guidance Report for Leak Path Factor Applications, SAND2016-YYYY, Sandia National Laboratories, Albuquerque, NM, to be published.
- [Magnussen 1981] Magnussen, B.F., “On the Structure of Turbulence and a Generalized Eddy Dissipation Concept for Chemical Reactions in Turbulent Flow,” 9th AIAA Sc. Meeting, St. Louis, (1981).
- [Mecham 1981] Mecham, W. J., Jardine, L. J., Pelto, R. H., Reedy, G. T. and Steindler, M. J., “Interim Report of Brittle-Fracture Impact Studies: Development of Methodology”, ANL-81-27, Argonne National Laboratory, Argonne, IL (1981).
- [Minana 2012] Minana, M., Turgeon, J., Lujan, C., Pilch, M., and Hackney, P., **Sandia National Laboratories Advanced Simulation and Computing (ASC) Software Quality Plan – ASC Software Quality Engineering Practices, Version 3.1**, SAND2008-5517, Sandia National Laboratories, Albuquerque, NM, March 2012.
- [Mishima 1968] Mishima, J., Schwendiman, L.C., and Radasch, C.A., “Plutonium Release Studies IV. Fractional Release from Heating Plutonium Nitrate Solutions in a Flowing Air Stream,” BNWL-931, UC-41 Health & Safety, November 1968.
- [Mishima 1973] Mishima, J., and Schwendiman, L.C., **The Fractional Airborne Release of Dissolved Radioactive Materials During the Combustion of 30 Percent Normal Tributyl Phosphate in a Kerosine-Type Diluent**, BNWL-B274, June 1973
- [Mishima 1973a] Mishima, J., Schwendiman, L.C., **Some Experimental Measurements of Airborne Uranium (Representing Plutonium) in Transportation Accidents**, BNWL-1732, August, 1973.
- [Nazar’ko 1981] Nazar’ko, V. M. et al., “Thermophysical properties of tri-n-butyl phosphate mercaptan absorbent,” *Gazov. Prom-st., Ser.: Podgot. Pererab. Gaza Gazov. Kondens.*, 3, 13-16, (1981).
- [NEA 1999] **International Standard Problem 40 - Aerosol Deposition and Resuspension, Final Comparison Report**, NEA/CSNI/R(99)4, Joint Research Centre European Commission, February 1999.
- [Popov 2000] Popov, S.G., “Thermophysical Properties of MOX and UO₂ Fuels Including the Effects of Irradiation,” ORNL/TM-2000/351, Oak Ridge National Laboratory (2000).

- [Radhakrishnan 1993] K. Radhakrishnan and A. C. Hindmarsh, "Description and Use of LSODE, the Livermore Solver for Ordinary Differential Equations," LLNL report UCRL-ID-113855, December 1993.
- [Ranz 1952] Ranz, W.E. and Marshall, W.R., "Evaporation from Drops," Chem. Eng. Prog, 48, 141-146, (1952).
- [Ricks 2011] Ricks, Allen, "Verification and Validation of SIERRA/Fuego in an Unconfined Upward Burning Solid Propellant Fire," SAND2011-6983C, Fire and Aerosol Sciences Sandia National Laboratories, Albuquerque, NM, October 17th, 2011.
- [Roberts 2003] Roberts, J.D., Jepsen, R.A., and James, S.C., "Measurements of Sediment Erosion and Transport with the Adjustable Shear Stress Erosion and Transport Flume," Journal of Hydraulic Engineering, Vol. 129, No. 11, 2003.
- [Rodriguez 2013] Rodriguez, S., Turbulence Modeling Tips, SAND2014-4707C, Sandia National Laboratories, Albuquerque, NM, 2014.
- [Rodriguez 2014] Rodriguez, S., Direct Numerical Simulation, Sandia National Laboratories, Albuquerque, NM, 2014.
- [Sehmel 1984] Sehmel, G.A., "Deposition and Resuspension," Chapter 12 in "Atmospheric Science and Power Production," Randerson, D., editor, DOE/Tic-27601, 1984.
- [Shenoy 2003] Shenoy, V. B., Kim, K.-S., "Disorder effects in dynamic fragmentation of brittle materials," Journal of Mechanics and Physics of Solids 51, pp 2023-2035 (2003).
- [SIERRA 2016] <http://compsim.sandia.gov/compsim/Docs/Sierra/4.40/GeneralRelease>
- [SIERRA 2016a] SNL, **SIERRA/SolidMechanics 4.40 User's Guide**, SAND2016-2707 O, Sandia National Laboratories, Albuquerque, NM, March 23, 2016.
- [SIERRA 2016b] SIERRA Solid Mechanics Team, **Sierra/SolidMechanics 4.40, User's Guide: Addendum for Shock Capabilities**, SAND2016-2705 O, Sandia National Laboratories, Albuquerque, NM, March 23, 2016.
- [SIERRA 2016c] Sierra Structural Dynamics Development Team, **Sierra/SD – Theory Manual**, SAND2016-3047 O, Sandia National Laboratories, Albuquerque, NM, April 4, 2016.
- [SIERRA 2016d] Sierra Thermal/Fluid Development Team, **SIERRA Low Mach Module: Fuego User Manual – Version 4.40**, SAND2016-4157, Sandia National Laboratories, Albuquerque, NM, May 2, 2016.
- [Sirignano 1983] Sirignano, W.A., "Fuel Droplet Vaporization and Spray Combustion Theory," Prog Energy Combust Sci., 9(4), 291-322, (1983).
- [Sutter 1981] Sutter, S.L., et al, **Aerosols Generated by Free Fall Spills of Powders and Solutions in Static Air**, PNL-3786, NUREG/CR-2139,
- [Sutter 1983] Sutter, S.L., **Aerosols Generated by Releases of Pressurized Powders and Solutions in static Air**, PNL-4566, NUREG/CR-3092, Pacific Northwest Laboratory, Richland, WA, May 1983.
- [Tieszen 2005] Tieszen, S.R., Domino, S.P., and Black, A.R., "Validation of a simple turbulence model suitable for closure of temporally-filtered Navier-Stokes equations using a helium plume," SAND2005-3210, June 2005, Sandia National Laboratories.

- [Wilcox 2006] Wilcox, D., Turbulence Modeling for CFD, 3rd Edition, DCW Industries, Lake Arrowhead, California, 2006.
- [Young 2015] Young, M.F., Liftoff Model for MELCOR, SAND2015-6119 Sandia National Laboratories, Albuquerque, NM, July 2015.
- [Zhou 2005] Zhou, F., Molinari, J.-F., “A cohesive model based fragmentation analysis: effects of strain rate and initial defects distribution,” International Journal of Solids and Structures 42, pp 5181-5207 (2005).
- [Zigh 2013] Zigh, G. and J. Solis, Computational Fluid Dynamics Best Practice Guidelines for Dry Cask Applications, United States Nuclear Regulatory Commission, NUREG-2152, 2013.
- [Zyskind 2006] Ziskind, G., “Particle resuspension from surfaces: Revisited and re-evaluated,” Reviews in Chemical Engineering, 22, 1-2, pages 1-123, 2006.

This Page Intentionally Left Blank

APPENDIX A

Summary Table for Handbook Data

This appendix provides a summary table for the Handbook, including a number of columns: Column 1 identifies the chapter or section number; Column 2 identifies the category, such as liquid, solid, etc.; Columns 3 and 4 tabulate the bounding values; Column 5 describes any initial size distribution provided; and Column 6 provides comments. Note that Column 1 intends to provide the information of interests from those chapters/sections from the Handbook. It is not necessarily a complete list, since Chapter 2 of the Handbook deals with gaseous forms, which are often assumed to be released during an accident. Thus, it may not have an interest in this current research in terms of ARF and RF. Note: this summary table is an “in-progress” table, which means that it would be updated as more substantiating studies are done to the data in the Handbook.

Chapter /section	Category	ARF	RF	Initial Size Distribution	Comments
3.0	LIQUID				This chapter divides into types of liquids, which includes aqueous solutions, organic, and combustible solvents.
3.2	<i>Aqueous solution</i>			Droplet distribution during bubbling is provided	This section describes models related to evaporation and boiling. Formulations on entrainment of liquid droplets from the surface of a bubbling or boiling pool are provided. Phenomena associated with these entrainments are described. (see Chapter 5 of this report for more details about describing the use of these models in the simulations.)
3.2.1	<u>Thermal Stress</u>				
	(a) Heating of aqueous solution in flowing air without surface rupture bubbles	3.00E-05	1		
	(b) Boiling (bubbles continuously breaking the surface of the bulk liquid with < 30% of volume of the liquid as bubbles)	2.00E-03	1		
3.2.2	<u>Explosion Stress</u>				
	Venting of pressurized liquids				
	(a) Venting below liquid level	1.00E-04	1	< 10 μm	
	(b) Venting above liquid level				
	[1] low pressure (< 0.35 MPa)	5.00E-05	0.8		
	[2] high pressure (>0.35 MPa)				
	(aqueous solution)	2.00E-03	1		~1 g/cc solution density
	(conc. Heavy metal solution)	1.00E-03	0.4		≥1.2 g/cc solution density
	[3] superheated liquid				
	(≤ 50°C superheat)	1.00E-02	0.6		
	(50 to 100°C superheat)	1.00E-01	0.7		
	(> 100°C superheat)	0.33*(MF) ^{0.91}	0.3		MF = mole fraction of pressurized gas/water vapor flashed
3.2.3	<u>Free-Fall Spill</u>				

Chapter /section	Category	ARF	RF	Initial Size Distribution	Comments
	3-m distance				
	(a) aqueous solution				
	[1] aqueous solution	2.00E-04	0.5		~ 1g/cc solution density
	[2] conc. Heavy metal solution	2.00E-05	1		≥ 1.2 g/cc solution density
	(b) slurries < 40% solids	5.00E-05	0.8		
	(c) viscous solution, viscosity > 8 centipoise	7.00E-06	0.8		
	> 3-m				Both ARF and RF should be larger than the 3-m fall, and the empirical correlations for ARF and drop size presented in Ballinger et.al (Jan 1988)
3.2.4	<u>Aerodynamic Entrainment and Resuspension</u>				Use of these values for < 100 hours would not introduce serious error due to the severe depletion of the source.
	(a) indoor surfaces (SS, concrete) up to normal facility ventilation flow; outdoors, pool for low wind speeds	4.00E-07	1		
	(b) indoor, covered with debris or under static condition	4.00E-08	1		
	(c) outdoors, large pools wind speed ≤ 30 mph	4.00E-06	1		
	(d) outdoors, absorbed on soil, no lengthy pooling wind speed ≤ 50 mph	9.00E-05	1		
3.3	<i>Organic Combustible Liquids</i>				No experimental data on the behavior of organic, combustible liquids in response to explosive release, venting of pressurized liquid, free-fall spills or aerodynamic entrainment were found. We are examining some of the experiments referenced in this section for this year in the area of fire in Section 3.3.1 and Section 3.3.6 of the Handbook (see Chapter 4 of this report)
	<u>Thermal Stress</u>				
	(a) volatiles (i.e., I2)	1	1		
	(b) Quiescent burning, small surface pool, or on larger pool	1.00E-02	1		
	(c) vigorous burning large pools	3.00E-02	1		This includes solvent layer burning over limited aqueous layer with sufficient turbulence to disrupt bulk of aqueous layer
	(d) Same as (C) to complete dryness	1.00E-01	1		
	(e) air-dried salts under gasoline fire	5.00E-03	1		Includes aqueous solution, on a porous or cracks, depression
	(f) same as (e) above, except on metal surface	2.00E-01	1		May not include porous, cracks or depression
4.0	SOLIDS				This chapter of the Handbook describes the data related to metals (primarily the release

Chapter /section	Category	ARF	RF	Initial Size Distribution	Comments
					from energetic hydride reactions, nonmetallic (such as ceramics) or composite solids, and powders.
	<i>Metal</i>				
4.2.1	<u>Thermal Stress</u>				
	(a) Plutonium				
	[1] oxidation (corrosion) at room temperatures				These values intended for < 100 hours
	(unalloyed Pu)	$2 \times 10^{-6} \mu\text{g Pu/cm}^2\text{-hr (dry air)}$	0.7		
		$7 \times 10^{-3} \mu\text{g Pu/cm}^2\text{-hr (100\% RH)}$	0.7		
	(delta-phase metal)	$7 \times 10^{-8} \mu\text{g Pu/cm}^2\text{-hr (dry air)}$	0.7		
		$6 \times 10^{-4} \mu\text{g Pu/cm}^2\text{-hr (100\% RH)}$	0.7		
	[2] oxidation at elevated temperatures	3.00E-05	0.04		
	[3] self-sustained oxidation	5.00E-04	0.5		Includes molten metal with oxide coat, self-induced convection
	[4]disturbed molten metal surfaces	1.00E-02	1		Such as flowing metal, actions resulting in continual surface renewal, high turbulence at surface. Impacted by high air velocity or free-fall, 95% confidence on these values. It is not applicable to oxidation of trace hydride, metal, powder contamination.
	[5] oxidation of small metal drops	1	0.5		hundreds of μm size, passing through air or explosive reaction of entire metal mass
	(b) Uranium				
	[1] complete oxidation of metal mass	1.00E-03	1		For thermal condition > 500 °C and for upward flow velocity of 0- 2 m/s. It is for airborne particles < 10 μm . A 95% confidence level is for flow velocities < 100 cm/s.
	[2] free-fall of molten metal drops	1.00E-02	1		This is based on an arbitrary increase of 95% confidence to the experiment data.
	[3] explosive dispersal of molten uranium	1	1		If the uranium is molten and subdivided in very small drops and ejected at sonic velocities (very fine particles and aggregates $\leq 10 \mu\text{m}$)
4.2.2	<u>Explosive Stress</u>				No recommended value is given. It refers to the surface contamination section of the handbook. For shock effects, it refers to the size of the TNT equivalent for respirable release. 20% of the metal should be used as respirable fraction. Consult national laboratories for analyses.
4.2.3	<u>Free-Fall and Impaction Stress</u>				No significant release as indicated. Refer to the surface contamination section of the handbook.
4.2.4	<u>Aerodynamic Entrainment and Resuspension</u>				Identical correlations as described in the Thermal Stress type (a)[1] above.
4.3	<i>NONMETALLIC OR COMPOSITE</i>				

Chapter /section	Category	ARF	RF	Initial Size Distribution	Comments
	<i>SOLIDS</i>				
4.3.1	<u>Thermal Stress</u>				
	(a) vitrified waste				No significant release by industrial-type fire.
	(b) aggregate (e.g., concrete and cement)				
	[1] tritium release from concrete				
	(if present and 200 °C)	5.00E-01	1		
	(if present and 600 °C)	1	1		
	[2] suspendible powder	6.00E-03	0.01		
	[3] spent commercial nuclear fuel				These materials were discussed in general for accident conditions related to severe accidents in commercial reactors. Thus release related to thermal stress is related to the release described in Section 4.4.1 of the Handbook.
4.3.2	<u>Explosive Stress</u>				No recommended value is given. It refers to the surface contamination section of the handbook. For shock effects, it refers to the size of the TNT equivalent for respirable release. 20% of the metal should be used as respirable fraction. Consult national laboratories for analyses.
4.3.3	<u>Free-Fall and Impaction Stress</u>	see comment	see comment	A distribution related to the UO ₂ pellet impacts is provided	A correlation for a combined value of ARF*RF is given as A*P*g*h, where A is an empirical correlation of 2E-11 cm ³ per g-cm ² /s ² , P specimen density, g/cm ³ , g is gravity at sea level, and h is fall height in cm. (See Chapter 6 for the simulation and model approach to substantiate the impact data.)
4.3.4	<u>Aerodynamic Entrainment and Resuspension</u>				No significant release. See contamination section of this handbook.
4.4	<i>Powders</i>				For high energy stresses, the bounding values of 10 μm AED and RF =0.1 should be assumed.
4.4.1	<u>Thermal Stress</u>				Based on the thermal condition of < 1000 °C
	(a) non-reactive compounds	6.00E-03	1.00E-02		Entrainment of pre-formed particles by the flow upwards of heated surface.
	(b) reactive compounds except PuF ₄	1.00E-02	1.00E-03		Particles formed by reaction given by the experiments
	(c) PuF ₄	1.00E-03	1.00E-03		Particles formed by reaction given by the experiments
4.4.2	<u>Explosive Stress</u>				
	(a) shock effect				No data
	(b) blast effect				Detonations and deflagrations
	[1] above the surfaces	see comment	see comment		No detailed information is provided for detonation. For large deflagration, use ARF of 1 and RF for the original powder size that is < 10 μm. It is for a container failure pressure of ~ < 0.17 MPa.

Chapter /section	Category	ARF	RF	Initial Size Distribution	Comments
	[2] accelerated airflow parallel to surface	5.00E-03	0.3		This represents a condition of the powders shield from the effects of a detonation or strong deflagration by standard containers.
	(c) venting of pressurized powders for deflagration > 25% confined volume				This also includes the condition of a deflagration and pressurized release. We are examining the pressurized release of powder experiment in this research (see Section 5.2 of [Louie 2015] and Section 5.2 of this report).
	[1] ≤ 0.17 MPa	5.00E-03	0.4		
	[2] 0.18 to 3.5 MPa	1.00E-01	0.7		
4.4.3	<u>Free-Fall/Impaction Stress</u>				We are examining a projectile hitting a can filled with powder (see Section 5.1 of [Louie 2015]). There is no experimental data for this simulation.
	(a) fall height < 3 m	2.00E-03	0.3		
	(b) fall height > 3 m	See comment. The calculated value must exceed those in (a)	See comment. The calculated value must exceed those in (a). The RF is limited in the total RF in the original powder.	see comment	Using PSPILL code to model powder spills - varying Mo (mass of powder spilled, kg). Air density and viscosity assumes to be 1.18 kg/m ³ and 1.85e-5 Pa-sec, respectively. The correlation is given as: $ARF = 2 * 0.1064 * (M_o^{0.125}) / (H^{2.37} / \rho^{1.02})$, where H = spill height, and ρ = bulk density of powder. $AMMD = 12.1 - 329 * \rho + 7530 * F$, where F is the airborne fraction (ARF). Note this equation only has a 46% correlation coefficient due to the variability in the data (see Section 5.1 of this report for the simulation).
	(c) suspended solid dispersed into flowing air	$ARF = 0.0134 v_{wind} + 0.00543$, where v_{wind} is the wind speed (m/s)	The RF is limited in the total RF in the original powder.		For enhanced air velocities normal to direction of powder flow.
	(d) suspension of bulk powder in confinement	1.00E-03	0.1		Due to vibration of substrate from shock-impact to powder confinement (e.g., glovebox or can) due falling debris or external energy (i.e., seismic vibration)
	(e) suspension of bulk powder in debris impact and air turbulence from falling object	1.00E-02	0.2		No confinement is involved.
4.4.4	<u>Aerodynamic entrainment and resuspension</u>				Use of values given for short time frame (< 100 hours) (See Chapter 2 for modeling resuspension due to hum activity described in [Fish 1967].)
	(a) homogeneous bed of powder exposed to ambient condition	ARR = 4E-5/hr	1		Normal process facility ventilation flow, nominal atmospheric wind speed < 2 m/s, gusts up to 20 m/s, following the event.
	(b) homogenous bed of powder buried under structural debris exposed to ambient condition	ARR = 4E-6/hr	1		Including static conditions within structure following the event.
	(c) entrainment of powders from road surface by passage of vehicular traffic	1.00E-02	1		ARF is per passage
5.0	<i>SURFACE CONTAMINATION</i>				

Chapter /section	Category	ARF	RF	Initial Size Distribution	Comments
5.2	<i>Contaminated, combustible solids</i>				
5.2.1	<u>Thermal Stress</u>				
	(a) packaged mixed waste	8.00E-05	1		For contaminated combustible materials heated/burned in packages with largely non-contaminated surfaces
	(b) uncontained cellulosic or largely cellulosic mixed waste	1.00E-02	1		For burning of unpackaged, loosely strewn cellulosic materials
	(c) uncontained plastics				
	[1] except polystyrene	5.00E-02	1		
	[2] polystyrene	1.00E-02	1		
	(d) dispersed ash dropped into air stream or forced draft air				These values are not typically applied to burning masses of combustible material in large fires. These apply to extremely severe conditions where loosely contaminated combustible material is driven airborne as part of an updraft fireball.
	[1] loose powder	4.00E-01	1		
	[2] air-dried solution or adherent contamination	8.00E-02	1		
5.2.2	<u>Explosive Stress</u>				
	(a) shock effect				No data. Assume to be venting of pressurized gases over material.
	(b) blast effect				No data. Assume to be venting of pressurized gases over material.
	(c) venting of pressurized gases over contaminated combustible waste	1.00E-03	1		
5.2.3	<u>Free-Fall and Impaction Stress</u>				
	(a) materials with high surface area to mass ratios	0	0		No significant suspension is expected for freefall spill from working heights (~1 to 1.5 m)
	(b) combustible material is unpackaged/lightly packaged and strongly impacts the floor	1.00E-03	1		Or is impacted by falling debris. The values are based on reasoned judgment.
	(c) combustible material is packaged in a relatively robust container that is opened or fails due to impact with the floor or impaction by falling objects	1.00E-03	0.1		
5.2.4	<u>Aerodynamic Entrainment and Resuspensions</u>				Note that no applicable data found. Reasoned judgment is used. (For < 100 hours)
	(a) indoor or outdoor exposed to ambient conditions	ARR = 4E-5/hr	1		Normal process facility ventilation flow, nominal atmospheric wind speed < 2 m/s, gusts up to 20 m/s, following the event.
	(b) buried under debris exposed to ambient condition	ARR = 4E-6/hr	1		
5.3	<i>Contaminated, noncombustible materials</i>				
5.3.1	<u>Thermal Stress</u>	6.00E-03	0.01		Reasoned judgment applies

Chapter /section	Category	ARF	RF	Initial Size Distribution	Comments
5.3.2	<u>Explosive Stress</u>				
	(a) shock effects				No recommended value is given. It refers to the surface contamination section of the handbook. For shock effects, it refers to the size of the TNT equivalent for respirable release.
	(b) blast effects				bounded by venting of pressurized gases in (c) below
	(c) venting of pressurized gases				These apply only to a loose surface contamination on the solid, not the solid as a whole. It includes corroded solids.
	[1] accelerated gas flows in area without significant pressurization	5.00E-03	0.3		
	[2] venting of pressurized volumes				
	(> 0.17 MPa)	5.00E-03	0.4		
	(< 0.17 MPa)	1.00E-01	0.7		
5.3.3	<u>Free-Fall and Impaction Stress</u>				
	(a) free-fall				Most materials will not experience free-fall spill. It is bounded by impact, shock vibration (b) below
	(b) impact, shock-vibration				
	[1] under brittle fracture	see comment	see comment		A correlation for a combined value of ARF*RF is given as $A * P * g * h$, where A is an empirical correlation of $2E-11 \text{ cm}^3$ per $\text{g-cm}^2/\text{s}^2$, P specimen density, g/cm^3 , g is gravity at sea level, and h is fall height in cm.
	[2] materials that do not undergo brittle fracture	1.00E-03	1		
5.3.4	<u>Aerodynamic Entrainment and Resuspensions</u>				It is bounded by powders estimates
	(a) indoor or outdoor exposed to ambient conditions	ARR = 4E-5/hr	1		Normal process facility ventilation flow, nominal atmospheric wind speed < 2 m/s, gusts up to 20 m/s, following the event.
	(b) buried under debris exposed to ambient condition	ARR = 4E-6/hr	1		
5.4	<u>HEPA Filters</u>				
5.4.1	<u>Thermal Stress</u>	1.00E-04	1		Extrapolation of maximum experimental of release of particles accumulated by the passage heated air through HEPA filters
5.4.2	<u>Explosive Stress</u>				
	(a) shock effects	2.00E-05	1		Based on experimentally measured release of accumulated particles from HEPA filters, localized failure from a momentary high pressure pulse.
	(b) blast effects	1.00E-02	1		High velocity air flow through up to filter break pressure
	(c) venting of pressurized gases	1.00E-02	1		
5.4.3	<u>Free-Fall and Impaction Stress</u>				No applicable experimental data for airborne release during free-fall of HEPA filters were uncovered
	(a) HEPA filter upon impact with hard unyielding surface				Bounded by conservative extrapolation of maximum releases measured for contained and uncontained HEPA filters.
	[1] enclosed (e.g., packages, filter	5.00E-04	1		

Chapter /section	Category	ARF	RF	Initial Size Distribution	Comments
	or plena housing)				
	[2] unenclosed	1.00E-02	1		
5.4.4	<u>Aerodynamic Entrainment and Resuspensions</u>				No significant release by nominal air velocities
6.0	INADVERTENT NUCLEAR CRITICALITY				
	<i>Solution</i>	see comment	none		The criticality is generically considered terminated by the evaporation of 100 liters of water or some lesser amount. The airborne source term is given by $(MAR_{c1} * DR_{c1} * ARF_{c1}) + (MAR_{s1} + DR_{s1} + ARF_{s1})$, where MAR_{c1} = inventory of gas and volatile, DR_{c1} =damage ratio for gases and volatiles generated in criticality, 1.0, ARF_{c1} =1 for noble gas, MAR_{s1} =inventory of non-volatile fission products generated, DR_{s1} =damage ratio radionuclides in solution, 1.0, and ARF_{s1} =5E-4 for non-volatiles, 1E-3 for ruthenium in fuel reprocessing solutions.
	<i>Fully Moderated/Reflected Solids</i>	see comment	none		This includes reflected bulk metal and metal pieces or solid fines such as powders that are moderated or reflected. It assumes no severe molten eruption, reactions and vaporization. Airborne source term = $MAR_{c2} * DR_{c2} * ARF_{c2}$, where MAR_{c2} =inventory of fissionable material and radionuclides from criticality, DR_{c2} =damage ratio, metal pieces=0.1, fines or powder=1.0, and ARF_{c2} =non-volatile can be neglected, 5E-1 for noble gases, and 5E-2 for iodine.
	<i>Bare, Dry solids</i>	see comment	none		No moderation, rather reflection. Airborne source term = $MAR_{c3} * DR_{c3} * ARF_{c3}$, where MAR_{c3} =inventory of radionuclides from fission, DR_{c3} =damage ratio, metal pieces=0.1, fines or powder=0.1, and ARF_{c3} =5E-1 for noble gas, 5E-2 for iodine.
	<i>Large Storage Arrays</i>				No data available

Distribution

External Distribution

- 2 U.S. Department of Energy
Office of Nuclear Safety - Nuclear Safety R&D Program
Attn: Alan Levin, NSR&D Program Manager
1000 Independence Avenue, SW
Germantown, MD 20585

- 2 U.S. Department of Energy
Office of Nuclear Safety Basis and Facility Design (AU-31)
Attn: Patrick Frias, NSR&D Project Manager
19901 Germantown Road (AU-31)
Germantown, MD 20874

- 1 U.S. Department of Energy
Office of Nuclear Safety Basis and Facility Design (AU-31)
Attn: Garrett Smith, Director, Office of Nuclear Safety Basis and Facility Design
19901 Germantown Road (AU-31)
Germantown, MD 20874

- 1 U.S. Department of Energy
Office of Nuclear Safety Basis and Facility Design (AU-31)
Attn: Samuel Rosenbloom
19901 Germantown Road (AU-31)
Germantown, MD 20874

- 1 U.S. Department of Energy
Office of Nuclear Energy
Attn: James C. Bresee
Mail Stop NE-52
19901 Germantown Road
Germantown, MD 20874

- 2 U.S. Nuclear Regulatory Commission
Office of Nuclear Material Safety and Safeguards
Attn: Yawar Faraz (1) and Wendy Reed (1), Division of Spent Fuel Management/LTSF
Mail Stop 4 B34
Washington DC, 20555-0001

- 1 U.S. Nuclear Regulatory Commission
Office of Nuclear Regulatory Research, Environmental Transport Branch
Attn: Mark Fuhrmann
Mail Stop 10 A12
Washington, DC 20555-0001

1 Louis F. Restrepo
Vice President, Business Development
Atkins Nuclear Solution US
2500 Louisiana Blvd NE, Suite 310
Albuquerque, NM 87110

1 Jose R.O. Munoz
Assistant Manager for Operations
DOE-NNSA, Los Alamos Field Office
3747 West Jemez Road
Los Alamos, NM 87544

1 Terry Foppe
Senior Nuclear Safety Specialist
Link Technologies, Inc.
20250 Century Blvd Suite 225
Germantown, Maryland 20874-1177

Internal Distribution

1	MS0721	Susan Y. Pickering	6200
1	MS0736	Richard O Griffith	6230
1	MS0744	John Bignell	6233
1	MS0744	Victor G. Figueroa	6233
1	MS0744	Patrick D. Mattie	6233
1	MS0744	San Le	6233
1	MS0747	Remi P.M. Dingreville	6233
1	MS0748	Nathan E. Bixler	6232
1	MS0748	Randall O. Gauntt	6232
1	MS0748	David L.Y. Louie	6232
1	MS0748	Lindsay N. Gilkey	6233
1	MS0828	Paul Crozier	1541
1	MS0828	Flint Pierce	1541
1	MS0828	Tyler Voskuilen	1541
1	MS0871	John S. Bowers	2720
1	MS1135	Alexander Brown	1532
1	MS1135	Carlos Lopez	1532
1	MS1135	Ethan T. Zepper	1532
1	MS1136	Gary E. Rochau	6221
1	MS1136	Salvador B. Rodriguez	6221
1	MS0899	Technical Library	9536 (electronic copy)

This Page Intentionally Left Blank

